LEVEL

DNA 4820F-1

ELECTRON INDUCED DISCHARGE MODELING, TESTING, AND ANALYSIS FOR SCATHA

Volume I. Phenomenology Study and Model Testing

IRT Corporation
P.O. Box 80817
San Diego, California 92138

R. C. Keyser   J. M. Wilkenfeld
R. E. Leadon   A. Weiman

31 Dec 78

Final Report 1 Sep 77—31 Dec 78,

CONTRACT No. DNA 001-77-C-0180

IRT-8161-

APPROVED FOR PUBLIC RELEASE;
DISTRIBUTION UNLIMITED.

E5p'.

Prepared for
Director
DEFENSE NUCLEAR AGENCY
Washington, D. C. 20305

81 2 26 088

REPORT DOCUMENTATION PAGE		READ INSTRUCTIONS BEFORE COMPLETING FORM
1. REPORT NUMBER DNA 4820F-1 ✓	2. GOVT ACCESSION NO. AD-A095 962	3. RECIPIENT'S CATALOG NUMBER
4. TITLE (and Subtitle) ELECTRON INDUCED DISCHARGE MODELING, TESTING, AND ANALYSIS FOR SCATHA Volume I—Phenomenology Study and Model Testing		5. TYPE OF REPORT & PERIOD COVERED Final Report for Period 1 Sep 77—31 Dec 78
		6. PERFORMING ORG. REPORT NUMBER IRT 8161-015-1 ✓
7. AUTHOR(s) R. C. Keyser R. E. Leadon J. M. Wilkenfeld A. Weiman		8. CONTRACT OR GRANT NUMBER(s) DNA 001-77-C-0180 ✓
9. PERFORMING ORGANIZATION NAME AND ADDRESS IRT Corporation ✓ P.O. Box 80817 San Diego, California 92138		10. PROGRAM ELEMENT, PROJECT, TASK AREA & WORK UNIT NUMBERS Subtask Q93QAXEE502-01
11. CONTROLLING OFFICE NAME AND ADDRESS Director Defense Nuclear Agency Washington, D.C. 20305		12. REPORT DATE 31 December 1978
		13. NUMBER OF PAGES 142
14. MONITORING AGENCY NAME & ADDRESS(if different from Controlling Office)		15. SECURITY CLASS (of this report) UNCLASSIFIED
		15a. DECLASSIFICATION DOWNGRADING SCHEDULE

16. DISTRIBUTION STATEMENT (of this Report)

Approved for public release; distribution unlimited.

17. DISTRIBUTION STATEMENT (of the abstract entered in Block 20, if different from Report)

18. SUPPLEMENTARY NOTES

This work sponsored by the Defense Nuclear Agency under RDT&E RMSS Code
X323078469 Q93QAXEE50201 H2590D.

19. KEY WORDS (Continue on reverse side if necessary and identify by block number)

Spacecraft Charging	Dielectric	Electron Induced Discharge
Electrical Testing	Electrons	Geosynchronous Satellites
Discharge Modeling	SCATHA	Coupling Analysis

20. ABSTRACT (Continue on reverse side if necessary and identify by block number)

A combined analytical and experimental program has been carried out to understand, simulate, and model the effects produced by the coupling of space electron induced electrostatic discharges (EID) into satellite structures. The program had five main tasks: to develop a worst case model for EID defined as a current source and to incorporate it into an SGEMP code for coupling analyses; to construct and electrically test a scale model (SCATSAT) of the P78-2 (SCATHA) spacecraft; to make a comparison between test results and model —

20. ABSTRACT (Continued)

prediction; and to specify a strawman set of electrical test procedures for simulating the response of spacecraft to ESD for incorporation into a Spacecraft Charging Military Standard; to compare the internal response of the SCATSAT to two techniques simulating different aspects of the discharge, the arc itself and the blowoff electrons. Work carried out under the first four tasks are described in this volume, which is Volume I of the final report. The fifth task is described in Volume II.

PREFACE

1

CONVERSION FACTORS FOR U.S. CUSTOMARY TO
METRIC (SI) UNITS OF MEASUREMENT

TO CONVERT FROM	TO	MULTIPLY BY
angstrom	meters (m)	1.000 000 X E -10
atmosphere (normal)	kilo pascal (kPa)	1.013 25 X E +2
bar	kilo pascal (kPa)	1.000 000 X E +2
barn	meter^2 (m^2)	1.000 000 X E -28
British thermal unit (thermochemical)	joule (J)	1.054 350 X E +3
calorie (thermochemical)	joule (J)	4.184 000
cal (thermochemical)/cm^2	mega joule/m^2 (MJ/m^2)	4.184 000 X E -2
curie	giga becquerel (GBq)*	3.700 000 X E +1
degree (angle)	radian (rad)	1.745 329 X E -2
degree Fahrenheit	degree kelvin (K)	$\tau_K = (t°~f + 459.67)/1.8$
electron volt	joule (J)	1.602 19 X E -19
erg	joule (J)	1..00 000 X E -7
erg/second	watt (W)	1.0L0 000 X E -7
foot	meter (m)	3.048 000 X E -1
foot-pound-force	joule (J)	1.355 818
gallon (U.S. liquid)	meter^3 (m^3)	3.785 412 X E -3
inch	meter (m)	2.540 000 X E -2
jerk	joule (J)	1.000 000 X E +9
joule/kilogram (J/kg) (radiation dose absorbed)	Gray (Gy)**	1.000 000
kilotons	terajoules	4.183
kip (1000 lbf)	newton (N)	4.448 222 X E +3
kip/inch^2 (ksi)	kilo pascal (kPa)	6.894 757 X E +3
ktap	newton-second/m^2 (N-s/m^2)	1.000 000 X E +2
micron	meter (m)	1.000 000 X E -6
mil	meter (m)	2.540 000 X E -5
mile (international)	meter (m)	1.609 344 X E +3
ounce	kilogram (kg)	2.834 952 X E -2
pound-force (lbf avoirdupois)	newton (N)	4.448 222
pound-force inch	newton-meter (N·m)	1.129 848 X E -1
pound-force/inch	newton/meter (N/m)	1.751 268 X E +2
pound-force/foot^2	kilo pascal (kPa)	4.788 026 X E -2
pound-force/inch^2 (psi)	kilo pascal (kPa)	6.894 757
pound-mass (1bm avoirdupois)	kilogram (kg)	4.535 924 X E -1
pound-mass-foot^2 (moment of inertia)	kilogram-meter^2 (kg·m^2)	4.214 011 X E -2
pound-mass/foot^3	kilogram/meter^3 (kg/m^3)	1.601 846 X E +1
rad (radiation dose absorbed)	Gray (Gy)**	1.000 000 X E -2
roentgen	coulomb/kilogram (C/kg)	2.579 760 X E -4
shake	second (s)	1.000 000 X E -8
slug	kilogram (kg)	1.459 390 X E +1
torr (mm Hg, 0° C)	kilo pascal (kPa)	1.333 22 X E -1

* The becquerel (Bq) is the SI unit of radioactivity; 1 Bq = 1 event/s.

** The Gray (Gy) is the SI unit of absorbed radiation.

2

TABLE OF CONTENTS

TABLE OF CONTENTS (continued)

LIST OF ILLUSTRATIONS

5

LIST OF ILLUSTRATIONS (continued)

LIST OF TABLES

LIST OF TABLES (continued)

1. EXECUTIVE SUMMARY

1.1 INTRODUCTION

This report documents the past year's activities of a program whose goal is to increase knowledge of the effects produced by the coupling of low energy ($\lesssim 30$ keV) space electron induced discharges (EID) into satellite structures. This work has been carried out under the sponsorship of the USAF Space and Missile Systems Organization (YC) and the Defense Nuclear Agency (RAEV) as part of the Spacecraft Charging at High Altitude (SCATHA) program. The initial phase of the program had five major components:

1. To develop a worst case model for EID defined as a current source and to incorporate it into an existing SGEMP code (SABER) to carry out coupling calculations to predict satellite response.

2. To construct and test an electromagnetically accurate 2/3 scale model of the P78-2 spacecraft (SCATSAT) under an electrical simulation of the response produced by EID.

3. To perform comparisons between test results and model predictions of the modified SABER code.

4. To specify a set of validated test procedures for accurately simulating the response of spacecraft to EID which can be incorporated into any Spacecraft Charging Military Standard which may be produced as part of the SCATHA program.

5. To compare the internal response of the SCATSAT to the techniques simulating different aspects of the electron induced discharge, the arc itself and blowoff of electrons.

The first four activities are discussed in this volume, the last in Volume II of this report.

9

1.2 DISCHARGE MODEL

A worst case discharge model has been generated based on a review of existing data, theoretical analyses, and model testing. Several discharge mechanisms were evaluated including: punchthrough of charge embedded in a dielectric to a conducting substrate; flashover of charge along the insulator surface to an edge; and a blowoff of embedded electrons from the surface of the dielectric. The blowoff mechanism was adjudged to produce the largest response defined in terms of structural replacement currents which flow consequent to a discharge. Analyses of the response of a right circular cylinder to each of the above discharge mechanisms indicate that the body currents produced by blowoff are more than an order of magnitude larger than those consequent to a punchthrough when the driving currents are properly scaled. The phenomenological discharge model had the following elements:

1. The surface density of outward emitted charges per unit area is proportional to the breakdown strength of the dielectric. This yields $Q/A \sim 10^{-7}$ C/cm^2.

2. The amount of charge emitted scales roughly linearly with area for small areas (<1 m^2).

3. The pulse characteristics are taken to be a rise time of 10 ns and a fall time of 10 to 100 ns.

In addition, a physical model of the discharge mechanism has been developed in which the punchthrough or flashover of a small amount of trapped charge triggers the blowoff discharge of the balance. This model remains to be validated by experiment.

The worst case model developed for this program is based on the limited information available as of June 1978. One of the major unanswered questions for studying EID coupling is to develop the data base for establishing better models in terms of current source descriptions related to system geometry (scaling), mode of initiation, propagation, and termination. Only with this information can one produce electrical test techniques for response simulation which can truly be said to have been validated. Hence, it is important to carry out the proposed electron spraying experiments on the CAN and SCATSAT.

1.3 CAN EXPERIMENT

To confirm the assumptions on which the model was based, a simple test case was examined - the so-called can experiment. The body replacement currents on a

cylinderical conducting can were measured for an arc discharge excitation that simulates a punchthrough breakdown of a charged dielectric sheet. These measurements were compared to calculated responses for three cases: (1) an arc discharge for essentially the same geometry as the experiment, (2) a uniform electron emission off the end of the can representing a blow off discharge, and (3) a capacitive direct injection drive of the end of the can representing an electrical simulation of the blowoff process. When the results are scaled to the same amount of released charge and the same pulse shape, the surface currents created by the outward emission of charge and the capacitive direct injection drive are more than an order of magnitude larger than the measured and calculated responses for the arc discharge, except very close to the breakdown point. Assuming that a significant fraction of the charge involved in a breakdown process is emitted outward, it is concluded that the major body-current responses of a spacecraft due to a dielectric discharge can be simulated by a capacitive direct injection drive electrical test. Thus for a worst case simulation the current practice of using arc discharges to simulate body responses due to electron induced discharges is, in general, not as good a technique as a capacitive direct injection drive, and the latter were chosen for our testing.

1.4 SCATSAT TESTS

For response testing, a 2/3 scale model of the P78-2, dubbed the SCATSAT was constructed whose design was chosen to simulate the basic structure of the real satellite, including the EMI enclosures, realistic cable harness layout, and shielding including incorporation of the same types of wires, a fairly detailed mockup of the solar arrays, and some of the experiment penetrations. No detailed simulation of the experiments or internal electronics was attempted although electronic boxes were included into which wires from the cable bundle were run, many of which were terminated with dummy loads.

The cable harness of the P78-2 was simulated by a cable bundle which included the major branches of the real harness but none of its minor branches unless they were adjudged important. The shielding treatment for the spacecraft harness was followed in constructing the mockup. No attempt was made to incorporate realistic dielectric surface treatments (as of yet) as analysis indicates that the presence of thin dielectrics on surfaces has a negligible effect on the response. For the proposed electron spraying tests, surface dielectrics will be incorporated into the model.

The principal goals of the electrical test program employing the SCATSAT were as follows:

1. To provide verification of the ability of the computer model/SABER code to predict EID coupling.

2. To develop electrical test techniques for simulating the most important aspects of the response of a spacecraft to EID.

3. Use SCATSAT to study coupling to and EID tightness of the P78-2.

A capacitative/direct injection technique was employed which simulated the outward emission of electrons judged to produce the major EID response. Two pulse shapes were employed, one was a short pulse with $t_r \sim 3$ ns and a FWHM of 10 ns; the longer pulse had a similar rise time and a FWHM of ~ 30 ns. Both the rate of change of surface current ($\dot{B}$) and cable currents were recorded. As a prelude to electron spraying tests in a vacuum tank, satellite responses were monitored for the case of no booms and with booms.

A fairly complete set of data was obtained for one drive scheme, symmetric excitation on the top, and smaller sets for three other drivers, all asymmetric excitations. The following general conclusions about the SCATSAT response can be drawn from the data analysis.

1. The external surface current responses of SCATSAT, and probably the P78-2 satellite, are not like those of a continuous conductive right circular cylinder as might have been expected and as such a satellite structure is frequently modeled.

2. The booms significantly affect the external surface current responses.

3. The top antenna cable is a major penetration into the internal cables for drive points near the antenna. Measurements at one point decreased by a factor of ~ 40 when this penetration was sealed. However, there is no area near the antenna where discharges are likely to occur, so it may not be problemmatic.

4. Frequencies appearing in the various responses can generally be accounted for in resonances associated with structural features of the spacecraft.

5. For 1,000 mA of emitted current, observed cable currents with the top antenna penetrations sealed are approximately:

12

a. On a boom wire shield: 3 mA

b. On the 3B cable bundle: 8 mA

c. On the loop cable: 3 mA

d. On the solar array cable: 5 mA

e. On the long dipole antenna: 50 mA.

The 3B and loop cable currents would be increased if the top antenna penetration were opened.

Another conclusion has been drawn concerning the drive schemes used. We wanted to use both short pulse, ~10 ns up and down triangular, and a long pulse, ~10 ns up and >100 ns down. The actual short pulse used had a rise time (10 to 90%) of ~3 ns with an 8-10 ns FWHM. This was obtained with the Anvil Pulser with no need for shaping. To obtain a longer pulse, it was necessary to increase the capacitance between the return plate and the object. Experiment and analysis showed that it was necessary to bring the return plate down very near the object and increase its size to the diameter of the object in order to bring the pulse width up to even 30 ns FWHM and 70 ns base width. This was still not as wide as desired but was accepted as a compromise. The experimental results suggest that this configuration resulted in resonances which were associated with the driver configuration rather than the object and that it is a less efficient excitation of the test object. More work is needed in this area if it is required to simulate long discharge pulses.

1.5 ANALYSIS

A parallel analytical and computer code modification task was undertaken whose aims were:

1. To incorporate the postulated discharge mechanisms and the capacitative direct injection pulse model into the SGEMP code SABER for EID coupling analyses.

2. To determine whether the presence of thin dielectrics on satellite surfaces significantly alters EID response.

3. To establish criteria for estimating the relative effectiveness of different discharge methods for producing EID generated transients (response scaling).

4. To predict SCATSAT body responses to CDI excitation for analysis verification.

13

The incorporation of blowoff into the code presented no essential difficulties as the outward emission of electrons is a standard feature of SGEMP codes. Although not presently included, the capability for the emission of ions can be handled relatively simply using electron emission and transport as the model. Similarly, the CDI excitation can be handled within the framework of the code as it exists by modeling it as a conducting plate and a current source with a predetermined shape and amplitude that travels along the wire connecting the drive plate and pulser to the SCATSAT. More difficult is the simulation of punchthrough. It was found that the optimum technique is to model the driver as a current source with the desired pulse shape which flows from the outer surface of the dielectric sheet to the conducting substrate. This modification also involved altering the properties of the dielectric sheet during the time that discharge was occuring to permit a flow of charge parallel to the surface of the dielectric. This is a nonstandard process for SABER and other SGEMP codes and had to be done with some care to minimize computational noise.

Spacecraft charging cannot occur unless dielectrics are present. However, there has been controversy as to whether the presence of the thin dielectrics typically found on the suface of satellites significantly effects the EID response. The incorporation of thin dielectrics into SGEMP codes in a straght forward manner is not trivial as the Courant criterion dictates that correspondingly small time steps be used; i.e. for a dielectric of thickness ~0.01 cm, one must employ time steps ~0.2 psec. This leads to rather large expenditures in computing time and money as the response produced by discharges can last from tens to hundreds of nanoseconds. Therefore a combined computer modeling and analytical approach was adopted to determine the relative importance of such dielectrics in effecting response. A sample problem was modeled with the SABER code with dielectric thickness as an adjustable parameter. In addition an evaluation was made of the magnitude of the relevant terms in the electromagnetic response equations. It was concluded that for the radiation environment under which spacecraft charging occurs and for the dielectric thickness as typically encountered on the surfaces of the satellites, the effect of thin dielectrics on the EID replacement currents generated is negligible.

Based on a comparison of analytical and experimental results, the following conclusions are drawn.

The computer model, which treated the exterior surface of the SCATSAT as a continuous conductor, produced predications which agree with the experimental data within a factor of 2.5 or better in all but three cases. In two of the cases, there is

sufficient confidence in the reliability of the experimental data to suggest that the prediction is in error because of a failure to include detail in the model; i.e., representing SCATSAT as a continuous conductor. In the third case, there is no corroberation of the experimental data, and no reason for the descrepency has been identified; and so the experiment may be in error.

Frequency content is difficult to compare but it appears that the model would predict the correct frequencies if the problem were carried out far enough. Unfortunately this becomes very expensive. A run of 100 ns would consume one hour of computer time.

The analysis points out the limitations faced in employing typical SGEMP codes in modeling EID response. First, even a three dimensional code has difficulty in handling significant external features such as booms or antennas, or modeling the interior of a spacecraft. Second, such analysis yields only the external currents. Additional analysis is required to predict internal coupling through penetrations into cables and electronics. Third, it is quite expensive to carry out sufficiently far in time response predictions with an SGEMP code. Characteristic spacecraft response modes associated with booms or cables show frequencies as low as 1 MHz. Therefore it is desirable that development be undertaken of analytic, normal mode, or lumped element computational techniques which could be used to follow the coupling response out to longer time periods (~1 μsec) to identify low frequency modes even if with reduced accuracy. A related task is to work out means of coupling both external currents and internal discharge sources produced by high energy electrons into the spacecraft electronics and cable harness to look for EID induced circuit upset or burnout - perhaps through the use of the system EMC analysis codes such as IEMCAP.

Finally, the SCATHA technology program has put its entire emphasis on the low energy substorm environment. There is an additional component of the natural radiation environment comprising high energy electrons (E < 5 MeV) which can penetrate the surface of the spacecraft and possibly create discharges in cables and dielectrics which are part of internal structural and electronic components. We feel that this aspect of the problem must be addressed in any program which attempts to ensure that spacecraft will function reliably in the space radiation environment.

2. INTRODUCTION

This section will discuss the nature of the problem being investigated in the SCATHA program, the scope of the present effort, and how it relates to the overall spacecraft charging problem. Basically, the approach followed in this program has involved defining a worst case discharge mechanism, incorporating this discharge into an SGEMP code for coupling analysis, developing an electrical analog for discharge response simulation, and carrying out model testing and analyses. Section 3 discusses the manner in which a worst case model of a space electron induced discharge was established, how an electrical simulation of the response to the discharge was chosen and validated, which was primarily through analysis and an initial test program on a simpler test object, a right circular closed cylinder. Section 4 describes the design and construction of the test object, which simulates the SCATHA P78-2 spacecraft. Section 5 discusses the test program carried out on the more complex satellite-like test object (SCATSAT) and presents the results of the test effort. Section 6 presents the analyses performed on the satellite test object and compares these to the experimental data. Section 7 is a general discussion of the results and outputs of this program and identifies some unanswered questions. Appendix A provides a detailed discussion of discharge scaling. Appendix B presents a circuit analysis of the Anvil Pulser-SCATSAT system. Appendix C describes a set of calculations and model tests made to determine whether interaction between the SCATSAT and the surrounding test area would be significant.

2.1 BACKGROUND OF THE SPACECRAFT CHARGING PROBLEMS

Adverse system effects created by spacecraft charging are potentially catastrophic (i.e., may cause spacecraft failure). In recognition of this fact many groups, both governmental and industrial, concerned with satellite survivability have launched programs to study this phenomenon. The most ambitious of these is the joint NASA/USAF Spacecraft Charging at High Altitude (SCATHA) venture in which a test satellite (P78-2) will be launched in early 1979 (Refs 1,2).

16

Over the past several years a series of anomalies have been observed in the behavior of satellites located in geosynchronous orbits at altitudes of approximately 5.6 earth radii (33000 km) (Ref 3). The anomalies have included equipment malfunctions such as uncommanded changes in operation, the recording by detectors of spurious events which in fact did not occur, and a persistent rise in operating temperatures. In a few cases, at least a partial failure of components such as power systems has occurred. It was gradually realized that the appearances of many, but not all of these anomalies could be correlated with the presence of a satellite in a magnetic substorm. In such storms the relatively cold high density plasma with electron temperatures of a few eV or less is replaced by a much hotter, lower density plasma with a temperature on the order of ten keV or more (Ref 4). The electron component of such a plasma is energetic enough to penetrate the surface of irradiated dielectrics where it is trapped. Because of the high resistivity of such dielectrics the trapped charge does not leak off. In this manner the irradiated and shadowed portions of a spacecraft can be differentially charged. This effect is enhanced if one side of the spacecraft is illuminated by sunlight. The illuminated portion of the spacecraft will tend to remain near the potential of the ambient plasma. Such differential charging of electrically isolated dielectrics can lead to the creation of potential differences between spacecraft components which can be as large as 20 kV.

At a sufficiently high potential difference dielectric breakdown occurs. Several possible discharge mechanisms have been identified. In one, the discharge current travels through the volume of the dielectric. A second type of discharge runs along the dielectric surface to a conductor. In conventional insulator literature, the former is typically called punchthrough while the latter is termed flashover. A third type of dielectric breakdown seems to occur in electron irradiated insulators. The consequent discharge results in the expulsion of particles out through the front surface. This has been called blowoff. In terms of producing a system response, that resulting from a blowoff discharge is most severe (Ref 5). It has been argued that the predecessor to a blowoff discharge is the buildup of a positive charge layer created near the insulator surface as a consequence of electron and ion induced secondary emission (Ref 6), although no conclusive evidence exists on this point. The other possibility is that the most common discharge process involves a combination of mechanisms such as a punchthrough or flashover which initiates an electron and/or ion blowoff (see Section 3.3).

These discharges can generate both currents and electromagnetic radiation that can couple into circuits. The resulting transients may then produce circuit malfunction or upset if they are not properly circumvented. Most importantly, the discharge current also generates replacement currents on the body of the satellite. These replacement currents generate fields which can couple into circuits. The currents themselves can degrade thermal blankets and second-surface mirrors which may be the possible cause for the observed rise in satellite temperatures, or contaminate other critical surfaces such as those found in optical sensors. In order to effect a level of hardening that is adequate but not excessive, one must be able to predict the behavior of spacecraft in worst-case environments. Thus, one must develop realistic charging, discharging, and coupling models on which to base such predictions.

Additional problems can be caused by the high energy electron of the space electron environment. This component is normally due to high energy electron (0.05<E<4 MeV) trapped in the outer van Allen belt. Even though the maximum incident fluence of the natural high energy electrons are an order of magnitude or more lower than for those for low energy plasma substorm electrons, such electrons can penetrate into the interior of spacecraft where they embed themselves in electronic components, leading to a possible total dose problem, or in cable dielectrics with the possibility of causing a discharge creating transients which couple into circuitry.

In addition, as a consequence of an exoatmospheric nuclear detonation, large numbers of electrons and ions are injected into the electron belts (Ref 7) which may lead to the same problems caused by the natural radiation environments.

Also present are both natural positive ions and, after a nuclear burst, artificial low energy ions.

The charged particle environment of importance to spacecraft charging is summarized in Table 1. Little is known about the effect of ions on altering the charging and discharging response of spacecraft and no attempt was made to take them into account in the electrical simulations developed during this program. Nor has any attempt been made to address the problems created by the penetrating components of the space radiation environment, not having received any mandate to do so. We feel that this is a major shortcoming of and limits the validity of the work reported on herein.

Testing for the effects of EID on system performance has been attempted on a few satellites. The procedures generally used in the past have been aimed at simulating the arc produced by the EID by various means, e.g., discharging a charged capacitor to

various points on a spacecraft or charging an insulation blanket until it arcs through or over (Ref 8,9). Such a procedure has been followed for the P78-2 EMC tests. System operation and/or transient signals on wires are monitored during the arc to determine system effects. As will be discussed later, such simulations leave out a very important feature of the discharge, namely, the emission of charge from the surface of a dielectric. This can be major driver of system response currents and its omission can lead to optimistic conclusions from such a test program. One goal of the present effort has been to define more accurate test techniques.

Table 1. Charged Particle Space Environment of Importance to Spacecraft Charging

Particles	Energy	Maximum Incident Flux (A/cm^2)
Ambient plasma	1 eV	5×10^{-10}
Natural low-energy plasma substorm electrons	2 - 30 keV	10^{-8}
Natural high-energy electrons	0.05 - 4 MeV	5×10^{-12}
Natural positive ions	2 - 50 keV	2×10^{-10}
Artifical low-energy plasma electrons	2 - 30 keV	2×10^{-6}
Artifical low-energy positive ions	2 - 50 keV	4×10^{-8}
Artificial high-energy electrons	0.1 - 5 MeV	5×10^{-10}

2.2 SCOPE OF CURRENT PROGRAM

The present program has been developed at the request of and in conjunction with SAMSO/YCT and YCP to carry out testing and analysis on a physical model of the SCATHA spacecraft (P78-2) and to define a preliminary set of electron induced discharge (EID) test procedures for that and other spacecraft.

The program had three main tasks. These are:

1. EID Coupling Analysis. The coupling of electron induced discharges to the SCATHA structure and major cable harnesses was modeled and analyzed. This involved defining a worst case specification of the discharge parameters. Then an existing SGEMP code was modified to incorporate a simulation of the discharge and response predictions were made.

2.   EID Coupling Experiments.   An experimental characterization of the response of the SCATHA physical model has been provided, including estimates of the coupling of structural currents to the main cable harness in order to verify the analytical EID coupling predictions, and to develop and validate specific electrical test techniques for the development of the draft EID Test Document. This has involved developing and validating ways of simulating the important features of EID as they are presently known, either singly or in combination.

3.   To suggest procedures for testing the P78-2 and other spacecraft for the effects of discharges induced as a consequence of space electron irradiation.

A flow diagram of the steps in the process of accomplishing these tasks as originally prepared is shown in Figure 1.

2.3 RELATIONSHIP TO THE OVERALL SPACECRAFT CHARGING PROGRAM

The joint NASA/USAF Spacecraft Charging at High Altitude (SCATHA) program was established to address the problem of surface charging of spacecraft in geosynchronous orbits exposed to magnetic substorms. It can be broken down into five areas (Ref 10).

1.   Environment: Development of an improved model of the geosynchronous plasma environment through analyses of existing data, use of data to be obtained from experiments in the P78-2 spacecraft, and modeling.

2.   Modeling.   Primarily the development of surface charging models for spacecraft exposed to the geosynchronous radiation environments. The most elaborate of these is represented by the NASCAP code (Ref 11) which is a fully three dimensional, self consistent charging code. This aspect of the program should logically include the equally important aspect of discharge modeling although very little has been done to date on this topic.

3.   Materials Characterization and Development.   Specification of those material properties of spacecraft dielectric which make them susceptible to charge up and discharge. An understanding of the phenomenology of charging and discharging should lead to structures in which the consequences of discharge are either eliminated or minimized while other desirable and
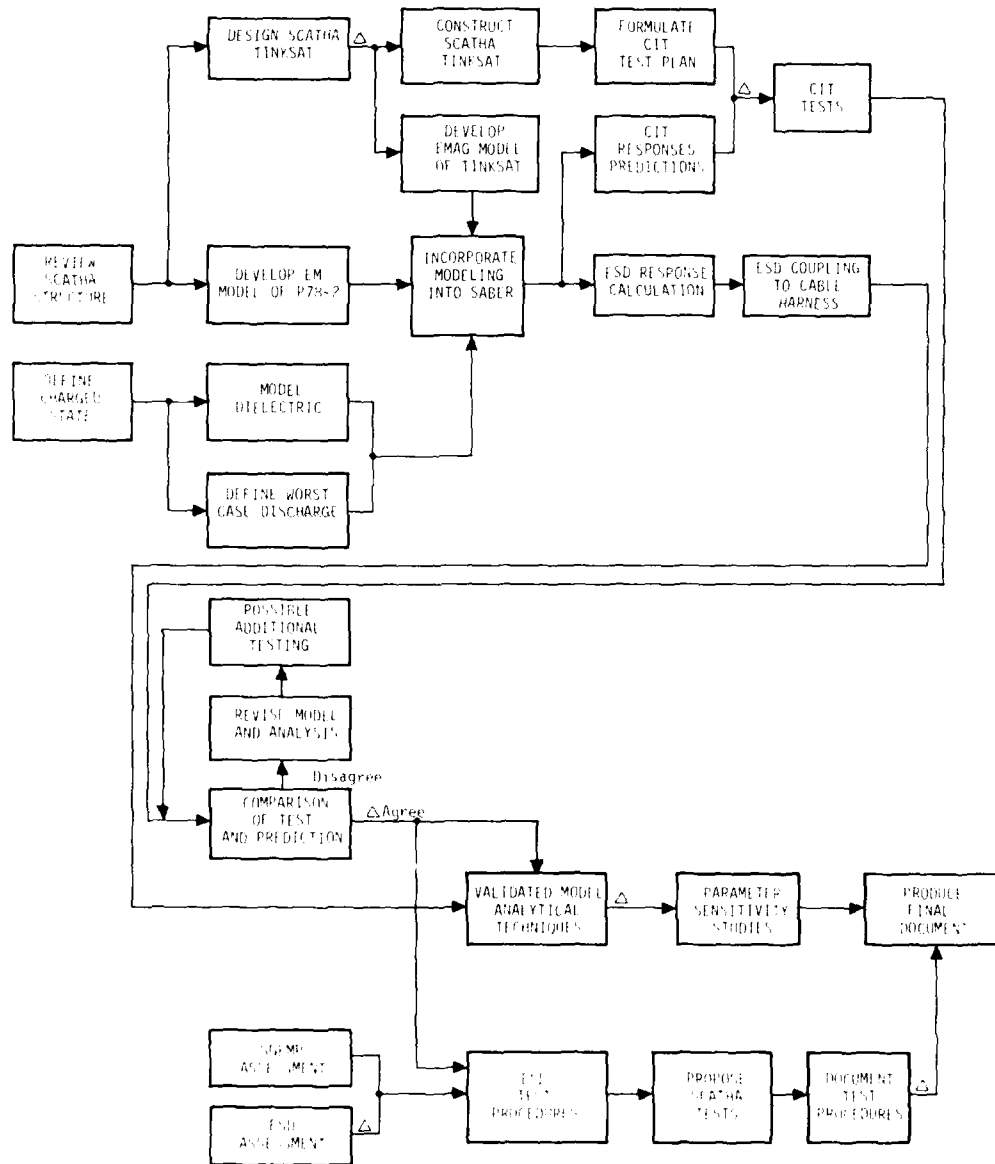
Figure 1. Program flow diagram

21

necessary features are maintained. They may be effected either by development of new materials, or modification of the manner in which existing structures are used.

4. Coupling. An identification of the manner in which discharges are coupled into spacecraft electronics. This aspect of the program depends heavily on having well defined discharge models and also on the existance of spacecraft coupling models and codes developed in other contexts such as SGEMP or EMC.

5. System Consequences. Given an understanding of the manner in which spacecraft charging can cause degradation of satellite performance, it should be possible to develop design techniques and test procedures to minimize these effects.

The IRT program has concerned itself with areas 2, 4, and 5 of the overall program in that some effort has been made to develop a worst case discharge model, coupling into a representative structure has been studied, system consequences examined, and a set of EID test procedures specified. In that regard the SCATSAT has been both an object for technology development and a spacecraft charging qualification model for the P78-2.

The question of survivability and reliability of spacecraft subject to EID is presently being examined by other groups in somewhat different contexts. There is evidence that the SGEMP response of a spacecraft can be significantly enhanced (at least at simulator fluences) if precharged (Ref 12). Thus, the phenomenology is of interest to the nuclear survivability community. In consequence, programs to study this aspect of the problem have been launched by both the Defense Nuclear Agency (under its SKYNET program) and the Air Force Weapons Laboratory (ECEMP Phenomonenology Program).

3. WORST CASE DISCHARGE SIMULATION

3.1 INTRODUCTION

In order to understand the effects of dielectric discharges, plan useful experiments, simulate the satellite responses with computer codes, and properly analyze the results, it is necessary to have at least a conceptual model of the dielectric breakdown process. At the beginning of this program, a brief review of the pertinent literature on dielectric breakdowns and discharges was undertaken. The limited scope of this review precluded any hope of developing a detailed physical model of the discharge with all its dependences on material and environmental parameters. Rather, the goal was a phenomenological model of what happens during a discharge, not necessarily why it happens, with worst-case numerical estimates of certain important macroscopic characteristics, such as the amount of charge released in one discharge and the resulting pulse shape. The results of this review and the phenomenological model which evolved are discussed in Section 3.2.

In the course of this program and through interaction with other researchers in the field, we have developed some ideas about the detailed physical processes that occur during a discharge. These ideas are summarized as a proposed physical model in Section 3.3.

The manner in which this model was incorporated into an SGEMP code and model predictions for comparison with the experimental data are reviewed in Section 6.

It is our evaluation that the blowoff mechanism in which most of the deposited charge is emitted outward away from the satellite produces a worst case response. A simulation technique based on the capacitive direct injection (CDI) technique developed for SGEMP testing was chosen for electrical testing. To partially validate this hypothesis electrical tests simulating blowoff and punchthrough discharges were carried out on a right circular cylindrical can. The results of these experiments are presented along with the supporting analysis in Section 3.4.

3.2 PHENOMENOLOGICAL MODEL OF A DIELECTRIC DISCHARGE

Two kinds of spacecraft discharges are discussed in the literature: metal-to-metal discharge via the breakdown of an intervening dielectric and dielectric-to-metal

23

discharge, again with breakdown of the dielectric. In a spacecraft in which all conducting structural members are mutually grounded, metal-to-metal breakdown would not occur. Since SCATHA is fully grounded internally (except perhaps for a few of the experiment packages), only dielectric-to-metal discharges are considered in this discussion, in particular the breakdown of charged thin dielectric sheets with con- ducting backings (substrates). Even for these breakdowns, there are two discharge modes: punchthrough of the charge imbedded in the exposed surface of the dielectric through the dielectric sheet to the substrate, and flashover, that is, the discharge of the imbedded charge to a conductor that is in contact with the exposed (irradiated) surface of the dielectric. Although these mechanisms are somewhat different, their effects are similar. Consequently, for the present phenomenological model, no distinction will be made between these two processes. For simplicity, we will usually call the breakdown "punchthrough" but essentially the same discussion applies to flashover discharge along the surface of the dielectric.

Our first assumption for a model for the discharge of a dielectric sheet over a conducting substrate was that the electrons which were trapped near the outer surface of the dielectric would suddenly break through the dielectric to the grounded substrate where they would recombine with their positive image charges. The electrical driving function from this discharge would consist of the collapse of the electrostatic potential from the dipole sheet and the radiation field associated with the arc discharge. Based on this model, it can be shown that the electric currents induced in the nearby conducting structure by collapse of the dipole electrostatic potential would be proportional to the actual discharge current in the collapsing dipole sheet multiplied by a factor approximately equal to Δ/L, where Δ is the thickness of the dielectric sheet and L is a characteristic dimension of the spacecraft structure. This is a consequence of Green's reciprocation theorem (Ref 13). Since, for typical spacecraft dielectric sheets, Δ/L is on the order of 10^{-3} to 10^{-4} this model predicts rather small currents in the structure and nearby electrical cables unless a cable just happens to lie on the dielectric very close to the punchthrough point. The sign of the structural replacement currents due to this kind of breakdown corresponds to electrons being driven away from the conducting substrate of the dielectric sheet.

An indication of the relative importance of the radiative fields compared to the collapse of the dipole potential can be obtained by comparing the magnitudes of the radiative and quasi-electrostatic E and H fields from a pulsed dipole (Ref 14). From Equations 3 and 9 of Reference 14 the radiative terms (those proportional to the time

24

second derivative of the dipole strength) are small relative to the quasi-electrostatic terms when the distance r from the pulsed dipole is less then (ct_p), where c is the speed of light and t_p is the characteristic time of the pulse. For $t_p \simeq 10^{-8}$ sec, $ct_p = 3$ m. Therefore, for positions on the spacecraft closer than 3 m from the dipole, the quasi-electrostatic terms apparently will dominate over the radiative terms, and the importance of the radiative terms is even less for longer pulse widths. Thus, it would appear that the structural return currents due to the collapsing dipole electrostatic potential and the associated radiative fields are quite small.

A cursory review of the literature on the breakdown of electron-charged dielectrics soon revealed that the above model is not complete for most cases. Although some discharges apparently agree with this model (Ref 15), the magnitudes of the structural return currents for most discharge events are much larger than predicted by the Δ/L ratio times a plausible discharge current. Moreover, the signs of the return currents correspond to electrons flowing toward the substrate of the dielectric sheet (Refs. 15-17). The reason for both of these results is that the breakdown of an electron-charged dielectric sheet apparently corresponds to negative charge (probably electrons) being emitted outward from the free surface of the dielectric, that is, away from the substrate. Experiments indicate that this charge travels at least several inches from the dielectric surface (Refs 17,18) and it probably goes much further. Measurements at IRT on the breakdown of electron charged spacecraft insulators have detected electrons at distances of over 30 cm evaluated from 12 cm circular samples. Admittedly the trajectories of the emitted particle will depend on the orientation of field lines which in turn depends on the boundary condition. The effective dipole strength, which determines the magnitude of the return current, is proportional to this emission distance. Since this distance is orders of magnitude greater than the dielectric thickness Δ, the effective dipole strength is also much larger than the dipole strength in the first model.

Models have been proposed to explain this enhanced emission during a discharge. Most of the models involve the electric field between the trapped electrons in the dielectric and an assumed positive charge density on the dielectric surface because the secondary electron emission in that region exceeds the rate of electron capture (Refs 18,19). In section 3.3, we propose a somewhat different mechanism to explain the outward emissity of charges. Regardless of which model, if either is correct, it is fairly clear that the most important discharges of the dielectric sheets, from the standpoint of spacecraft electromagnetic effects, involve the emission of negative charge outward

25

from the dielectric surface. The validity of this conclusion is substantiated in Section 3.4 by comparing the results of the arc discharge experiments with calculated results for outward emission of charge and capacitive drives. The details of the discharge models would be of interest to us mainly as an aid in predicting the magnitude and shape of the discharge pulse as functions of the physical parameters of the dielectric (for example, breakdown strength, radiation-enhanced electric conductivity, secondary-electron-emission efficiency, etc.) and the electron plasma.

There is a limited amount of information in the literature on the magnitudes of the return currents following a dielectric discharge and their time histories. However, there are many sample and experimental parameters that could affect the measured values: for example, the thickness, breakdown strength, dielectric constant, and radiation-induced electrical conductivity of the dielectric sheet; the energy spectrum of the incident electrons (penetration depth, ionization density, secondary-electron-emission efficiency); temperature; area and shape of the irradiated sample; and the electric coupling (capacitive, resistive, and inductive) of the specimen to the surrounding conducting structure. Unfortunately, the parameters for different experiments are often considerably different and there is not enough available data to determine the dependences on each. Therefore, in the following, we ignore all dependences on material properties and electron energy spectra and consider only the rough dependences on sample area and the experimental setup.

3.2.1 Total Emitted Charge

The total amount of charge Q emitted from a dielectric sheet can be written as

$$Q = J_p t_p A \tag{1}$$

where J_p is the peak emission current density during the discharge, t_p is the effective pulsewidth at half maximum, and A is the area that discharges.

If one ignores the influence of edge and perimeter effects in initiating breakdown, it seems plausible that, for small areas, Q should vary linearly with A, that is Q/A = constant, assuming that the whole area discharges in one pulse. Furthermore, for large areas, Q might be sublinear in A because the edges of the discharge region might not discharge completely. At extremely large areas, Q for one discharge might

26

approach an asymptote. A simple and plausible mathematical relation that expresses the above dependence is

$$Q = \left(\frac{dQ}{dA}\right) A_o \left[1 - \exp\left(-A/A_o\right)\right] \quad . \tag{2}$$

No physical significance is implied for this expression and it is only advanced as a possible description of the trend with area. It might turn out that edge and perimeter effects are very important and the trend with area could be superlinear, at least for small areas. The evidence on this point is not clear. Balmain et. al. (Ref 20) have found evidence that the peak current emitted scales roughly with the square root of area for Teflon. However, the data is less clear on the scaling of total charge emitted. Hopefully, future experimental analysis of data can better establish the dependence of Q on area. However, in the absence of better information at the present time, this relation will be used for now. In Equation 2, $\frac{dQ}{dA}$ is the slope of Q versus A for small areas and A_o is the effective area that discharges in one pulse when the true area A is very large. Within the accuracy of Equation 2, we can approximate it as

$$Q = \left(\frac{dQ}{dA}\right) A \qquad \text{for } \frac{A}{A_o} < 1.0$$

$$= \left(\frac{dQ}{dA}\right) A_o \qquad \text{for } \frac{A}{A_o} > 1.0 \tag{3}$$

The correct value of A is unknown at the present time. It has been suggested (Ref 21) that a value of 10 ft^2 ($\approx 1 \text{ m}^2$) be used for A_o, which may be reasonable as a starting point at this time although it is certainly open to debate. This limiting area is one of the discharge parameters that definitely needs more study.

A reasonable upper limit for dQ/dA can be obtained by saying that the incident electrons are trapped in the dielectric until the electric field that they produce ($E = \sigma/K\epsilon_o$) equals the breakdown strength of the dielectric (E_{BD}). Then all of the trapped electrons are emitted outward from the dielectric. In the above equation for E, K is the relative dielectric constant, ϵ_o is the permittivity of free space, and σ is the surface density of trapped charge. Thus

$$\frac{dQ}{dA} = \sigma_{BD} = E_{BD} K \epsilon_o \quad . \tag{4}$$

27

There is a question whether the effective breakdown strength E_{BD} for the breakdown of electron-charged dielectrics is the same as the breakdown strength measured simply by the application of high fields. In recent informal discussions, Prof. P. Budenstein of Auburn University felt that they should be essentially the same, but there is no definite evidence for this opinion. This is another area where good experimental data is needed.

As a rough order of magnitude for most polymers of interest, assume $E_{BD} = 5 \times 10^5$ V/cm and $K \epsilon_o \simeq 2 \times 10^{-13}$ f/cm, so $\frac{dQ}{dA} \simeq 10^{-7}$ coul/cm^2. This number is in reasonable agreement with what little information has been found in the literature, as is shown below.

Reference 16 quotes peak return currents of 20 to 100 A from a 300 cm^2 area with a pulse duration of 500 ns. Assuming a triangular response, the return charge per unit area (Q_r/A) is

$$Q_r/A = 0.5 \frac{(5 \times 10^{-7} \text{ sec})}{(300 \text{ cm}^2)} I_p \simeq 1.7 \times 10^{-8} \text{ to } 8.3 \times 10^{-8} \text{ coul/cm}^2 \quad . \tag{5}$$

In the experimental setup used in Reference 16, the return charge Q_r should be less than the emitted charge Q by the ratio of the capacitance of the test sample to ground and to the emitted charge. If the emitted charge travels at least a few inches from the emitting plate (Refs 17,18), it would end up on the walls of the test chamber and this ratio would be between 1/2 and 1/5. Dividing Q_r/A by this ratio gives a value for the emitted charge Q/A that brackets the value obtained from Equation 4.

Reference 15 reports a peak scope reading of a few volts across a 1 MΩ load (therefore, assume $I_p \simeq 2 \times 10^{-6}$ A). For this loading, Figure 3 of Reference 15 indicates pulse durations on the order of 0.5 μsec. The area of the sample is not clearly stated, but it is less than 4 cm^2. Using A = 3 cm^2,

$$\frac{Q_r}{A} \simeq \frac{(2 \times 10^{-6} \text{ A}) (0.5 \text{ sec})}{(3 \text{ cm}^2)} \simeq 3.3 \times 10^{-7} \text{ coul/cm}^2 \quad .$$

For the small test chamber used in Reference 15, the ratio of capacitance to ground and to the emitted charge should be close to unity. Therefore, the emitted charge

$$(Q/A \sim 3 \times 10^{-7} \text{ coul/cm}^2)$$

is again comparable to the value from Equation 4.

Reference 17 gives the current that is induced in a 12 inch long wire, 0.03 inches in diameter, and located 3 inches from the plane of the sample, which had an area of 500 cm^2. The peak current induced in the wire was about 60 mA and the approximately-triangular pulse had a base width of about 30 μsec. Basing the calculation on the projected area of the pickup wire gives

$$Q_r = \frac{0.5(0.06A)(3 \times 10^{-5} \text{ sec})}{(12)(.03)(2.54)^2} = 4 \times 10^{-7} \text{ coul/cm}^2 \quad .$$

If we assume that the charge per unit area that is intercepted by the pickup wire is the same as the charge per unit area emitted from the dielectric, then

$$\frac{Q}{A} \simeq \frac{Q_r}{A} \simeq 4 \times 10^{-7} \text{ coul/cm}^2$$

which is again in rough agreement with the previous estimates.

Finally, Reference 22 reports breakdowns when the incident charge is about 4×10^{-6} coul/cm^2. The authors also imply that all of these electrons are trapped. This value is considerably larger than the 10^{-7} coul/cm^2 previously calculated from Equation (4). However, that could just mean that the breakdown strength of their material is large since it is known that E_{BD} in polymers can have large variations. Unfortunately, they don't say how much of this charge is released during a discharge.

Thus, in spite of the inconsistencies in the above calculations of comparing values for different dielectric materials and thicknesses, electron energies and dose rates, background illumination intensity, etc., all of the quoted experimental results for the emitted charge density are in reasonable agreement with Equation (4), using average values for the material properties. At a minimum, Equation (4) provides a guide for planning future experiments and forms a standard against which future experimental data, which hopefully will be forthcoming, can be compared.

3.2.2 Emission Time History

The correct values to be used for the peak emission current density (J_p) and the pulsewidth (t_p) in Equation (1) are even more poorly known than the total emission charge density (Q/A). It has been suggested (Ref 21) that both the total emission current ($\frac{dQ}{dt} = J_p A$) and the pulsewidth t_p be assumed linear in the area A, or perhaps t_p

proportional to $A^{1/2}$. With this assumption, J_p is independent of A. The rationale for assuming t_p proportional to $A^{1/2}$ is that the charge is often emitted from one localized breakdown spot. Therefore, charge has to flow from all of A to the breakdown point (an average distance $\approx A^{1/2}$). If the velocity of the charges inside the dielectric is roughly constant, then t_p is proportional to $A^{1/2}$. The assumption of t_p linear in A was just for an additional margin of safety, assuming that a long pulse is more critical. However, these dependences on area have never been confirmed and the general opinion of attendees at a recent dielectric conference was that a uniformly charged sheet would tend to completely discharge in one pulse with a pulse width that was not significantly determined by the sample area.

Even if each of the above assumptions were plausible in itself, when taken together they are not consistent with the fact that Q/A is apparently about independent of A for $A/A_o < 1.0$ from Equation (3) and (4). Since, from Equation (1),

$$Q/A = J_p t_p \quad , \tag{5}$$

the product $J_p t_p$ should also be independent of A, and perhaps even a decreasing function of A for large A/A_o. In other words, if t_p increases with increasing A, the emission current density J_p (averaged over the emitting area) should decrease by the same function of A, so that the total emitted charge per unit area is independent of A.

With the above relationship, we have eliminated one variable (either J_p or t_p). However, we still need an estimate of the absolute value of the remaining variable (t_p or J_p). In the literature, various characteristic times of the return-current pulses have been quoted, ranging from 4 to 8 ns (Ref 15) to tens of microseconds (Ref 17). One has to be careful that one is talking about the same times from different experiments and that the quoted values are not overly affected by the experimental setup and/or the measurement system. For example, the 4 to 8 ns given in Reference 15 for a small-area sample ($<4 \, cm^2$) is the rise time of the pulse (independent of the circuit time constant) and also the fall time when the time constant was fast enough ($R = 50\Omega$). It was not clear if the response was essentially triangular or whether there was a plateau between the rise and fall times. When the scope impedance was increased to 1 MΩ, the response was governed by the circuit time constant and it appeared to be about 0.5 μsec, although this value is not consistent with just scaling the fast times by the ratio of the impedances.

By comparison, Reference 17 quotes a rise time of 20 ns for a 500 cm^2 sample and a pulse duration of 1 μs or more. The latter was undoubtedly governed by the circuit response. Similarly, Reference 16, and also Reference 23 by the same authors as Reference 16, indicate pulse durations for 300 cm^2 samples on the order of a few hundred nanoseconds with rise times on the order of 100 ns. Finally, Reference 22 indicates rise times and pulse durations in the order of a few tens of nsec for a sample with an area of about 10 cm^2.

As usual, the above data do not show a completely consistent pattern. It is true that the two smallest samples had rise times of about 10 ns. However, the next larger sample (300 cm^2) had rise and fall times of about 100 ns, whereas the largest sample (500 cm^2) was back to a rise time of 20 ns. Since slow rise times could possibly be explained by inductances in the leads between the sample and the measuring system, we tend to favor the shorter rise time (20 ns) even for the larger area. Thus, within the accuracy of the available information and the differences between the various experiments, there is no apparent significant dependence of the shape and duration of the emission pulse on the sample area. This conclusion is consistent with other kinds of dielectric breakdown measurements. Of course, if the capacitance of the sample area and the measuring impedance make the circuit time constant greater than the characteristic times of the emission pulse, the observed response times would be slower than the emission pulse. The difficulty, of course, is that one is trying to estimate what the time history of the discharge pulse is by that of the response it produces in the above experiments.

Since, for a given total emitted charge, the shortest pulse length will usually produce the largest rates of change of magnetic field, and therefore coupling into cables, it was decided that a pulse with about a 10 ns rise and fall should be used for the simulations. However, if pulse discrimination techniques are used to protect circuits, the longer pulse width may be the critical one. Therefore, it was decided that a longer pulse with say, 10 ns rise and 100 ns fall should also be employed. It was not possible in practice to achieve a pulse this long with the capacitative drive technique (q.v. Section 5.2). The relative effect of the longer times on the return currents is fairly predictable with SGEMP codes.

There is a potentially misleading aspect about the above results. If a charge of 10^{-7} coul/cm^2 is emitted from the dielectric in a few nanoseconds, one might expect an electric field (E) of about 10^6 V/cm between the emitted charge and the dielectric. This field would oppose the outward motion of the electrons. If the emitted electrons

31

had energies (A) around 50 keV, this field would cause space-charge-limiting at a distance $d = A/E = 0.05$ cm. But if the electron motion were really limited to this distance from the dielectric, the return currents would be orders of magnitude less than the observed ones and the experimenters would not have detected significant currents several inches from the emitting plate. The answer to this puzzle apparently is that, as the electrons are emitted from the dielectric, other electrons are drawn into the substrate as the return current. Therefore, the electric field between the emitted charge σ and the dielectric is much less than the value for a planar sheet of charge, $E = \sigma / K\epsilon_o$. In other words, most of the flux lines from the emitted electrons terminate on the walls of the test chamber, instead of on the positive charge left behind in the dielectric. Consequently, the emitted electrons move in a low-field region and are not strongly attracted back to the emitting surface.

Space charge limiting should not be as important in limiting blowoff of charge in a satellite in the space environment. There the satellite becomes negatively charged rather than remaining electrically neutral in the idealized laboratory experiments where the conducting substrate is grounded. The discharge process in the former case just frees the satellite of this excess charge, leaving the satellite neutral (or at least less negatively charged). This is unlike the SGEMP case where the object becomes partially charged after photo emission.

As a side issue, if the laboratory experimenters wish to measure the full emitted charge and not just the fraction that escapes the space-charge fields, they should try to minimize space-charge limiting by making the capacitance between the emitted electrons and the surrounding container as large as possible and the impedance of the return line as small as possible.

In summary, the following characteristics were chosen for the phenomenological model of spacecraft dielectric discharges,

1. Use a surface density of outward emitted charge given by

$$\frac{Q}{A} = E_{BD} K \epsilon_o$$

    up to a maximum area A_o.

2. Until further information becomes available, use
    $A_o \simeq 10 \text{ ft}^2 \simeq 10^4 \text{cm}^2 = 1 \text{ m}^2$.

3. Use a basic emission pulse with a 10 ns rise and fall time but also consider a somewhat larger pulse with times from 10 to 100 ns.

32

4. Select the emission current density to be consistent with Q/A and the assumed pulsewidth.

3.3 PROPOSED PHYSICAL MODEL OF DIELECTRIC DISCHARGE

The model for the discharge process discussed in Section 3.2 is purely pheno-menological - that is, it attempts to describe what happens during a discharge in terms of emitted charge and pulse shape, but no attempt is made to explain why the outward emission occurs. Although IRT was not tasked to develop a physics model of the discharge process under the present program, we have naturally been thinking about the subject and the following model is suggested to hopefully stimulate a few ideas. This model is not completely original with IRT but is the outgrowth of thinking about the experimental results and analyses of other researchers, for example, References 24 and 25.

One of the major unanswered questions characterizing dielectric discharges is: what is the mechanism by which electrons (and perhaps ions) are emitted from the outer surface of electron-irradiated dielectrics during a discharge? Some related questions are: (1) Is this emission basically a one-dimensional effect as implied by the Meulenberg model (Ref 19), or is it caused by heating and/or magnetic field effects as the electrons funnel toward one initial breakdown spot? (2) Is the outward emission correlated with, and perhaps initiated by, punchthrough breakdown to the substrate of the dielectric or flashover from the dielectric to an adjacent conductor?

The central idea of our proposed model is that the outward emission of electrons during a dielectric discharge is initiated by a punchthrough breakdown through the dielectric to the substrate or by flashover from the dielectric to an adjacent conductor and thence back to the substrate. In the following discussion, a punchthrough breakdown is assumed but the same discussion applies to flashover. As the trapped electrons funnel toward the initial breakdown spot, they are heated by I^2R energy and are acted on by the Lorentz force ($\vec{v} \times \vec{B}$) which tries to force electrons outward. The basic features of the model are illustrated in Figure 2. Figure 2(a) shows a grounded substrate and a thin dielectric with a sheet of embedded electrons close to the outer surface of the dielectric. If a punchthrough breakdown to the substrate occurs (Figure 2(b)), the trapped electrons in the dielectric and their positive image charges in the substrate flow toward the breakdown point. (For some reason connected with the distribution of charge and radiation-induced conductivity, the trapped charge seems

33

much more mobile in the plane of the trapped charge than through the bulk of the dielectric.) The electrical currents of electrons and their image charges produce a magnetic field that tries to force the electrons outward from the dielectric. If the I^2R heating in the vicinity of the punchthrough weakens the surface of the dielectric sufficiently, the electrons would be able to break out to free space. Once they escape from the dielectric, the exterior electric field created by the trapped electron will usually be in the proper direction to further accelerate the electrons away from the dielectric. In addition, such a mechanism, once initiated, may cause thermal breakdown as the electrical conductivity will increase because of heating.
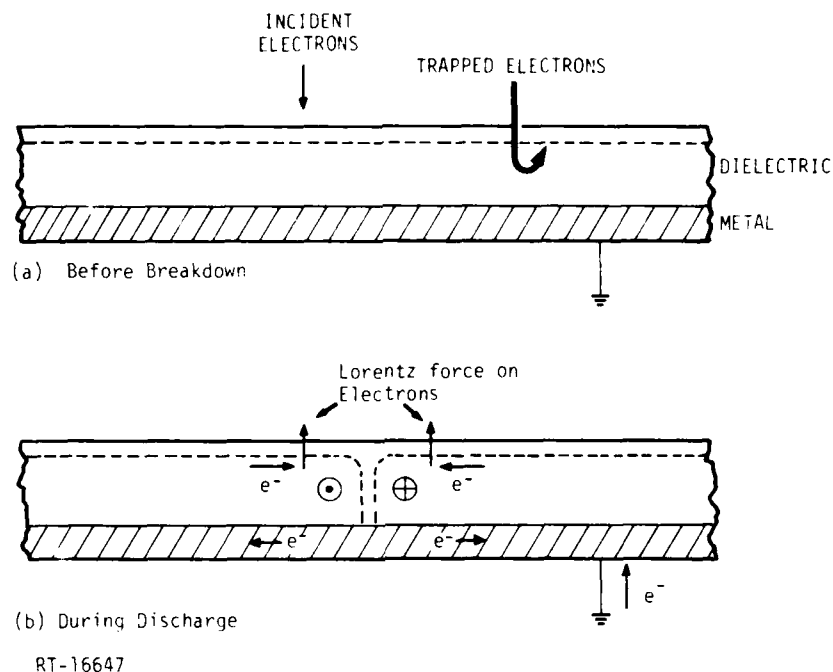
Figure 2.

Illustration of breakdown mechanism ($\odot$ and $\oplus$ are directions of H field, out of and into paper, respectively). The electrons are initially repelled from the punchthrough point, i.e. move away from the substrate. Subsequently, during blowoff, electrons flow up through the connection to system ground.

This model could be investigated by a few experiments which are designed to determine whether or not an outward emission of electrons follows from a punchthrough breakdown to the substrate and, if so, what fraction of the trapped charge goes to the substrate and what fraction is emitted.

34

One can also analytically model the breakdown process using some appropriate SGEMP computer code which includes the Lorentz $\vec{v} \times \vec{B}$ force, such as ABORC (cylindrically symmetric code) or MEEC-3D (a three-dimensional Cartesian-coordinate code). No present SGEMP code has the capability to simulate I^2R heating and breakthrough of the trapped charge from the dielectric surface. However, various approximations could be made to the real situation. For example, the problem could be started with the electrons at rest adjacent to the outer surface of the dielectric. Then, at time zero, an electrical short through the dielectric to the substrate could be simulated at one position. The code would then follow the electrons as they are accelerated toward the breakthrough point by the electric fields and away from the dielectric by the Lorentz force. The code would have to have the characteristic that electrons would reflect off the dielectric surface and not become trapped. In spite of the approximations which would be necessary, this analytical model might shed some light on the electron dynamics in this postulated breakdown process.

Some possible confirming evidence for this model was obtained accidentally during the arc discharge experiments (q.v. Section 3.4). Occasionally, the Mylar sheet between the copper foil and the aluminum can failed by punchthrough when the voltage pulse was applied. When this occurred, the upper copper foil bulged outward in the region of the punchthrough. Although this bulging could have been due to gas formed under the foil during the dielectric punchthrough, it might also have been due to the Lorentz force as current flows toward the breakdown point. Additional confirming evidence is seen in photomicrographs of discharges taken by Yadlowski (Ref 24) and Balmain et al. (Ref 15).

3.4 ELECTRICAL SIMULATION OF DISCHARGES - THE CAN EXPERIMENT

3.4.1 Rationale

Two important questions were raised in carrying out the modeling effort which also have a serious impact on the electrical testing program. The first of these is what constitutes a realistic physical model of the discharge in terms of a correct accounting for particle motion and the fields generated. The second question concerns what aspects of the discharge must be simulated electrically to excite the important modes of spacecraft response. While it is important to develop a good model for the discharge process, from the point of view of determining system effects it may not be necessary or practical to carry out an exact simulation. In fact, for testing on real spacecraft, it

would be desirable to develop low level, nondestructive electrical stimulation techniques to qualify spacecraft for survivability against the effects of EID.

The early models for electron induced discharge usually assumed that the discharge consisted of a punchthrough of the trapped charge from the surface of the dielectric to the substrate. In this case, a logical simulation of the discharge would be an arc discharge through a dielectric sheet. However, as we have discussed in Section 3.2 the body replacement currents would be quite small, on the order of the discharge current times the ratio Δ/L, where Δ is the thickness of the dielectric and L is a characteristic dimension of the spacecraft. A much larger response is produced when the released charge is emitted outward from the irradiated surface of the dielectric than for a punchthrough breakdown. A logical simulation of this effect would employ a capacitive drive technique similar to that used in reproducing the effect of emission of photoelectrons in simulating SGEMP responses (Refs 26,27).

In developing electrical test techniques and computer simulations for the effect of dielectric discharges on spacecraft responses, it is important to know how to approximate the important features of the discharge as electrical driving functions. The objective of this phase of the spacecraft charging program was to determine experimentally and theoretically the relative importance of arc discharges and the outward emission of charge in producing body return currents. The effect of test object complexities on the results, especially those which are difficult to model analytically, should be eliminated in this kind of a benchmark experiment in order to keep the variables at a minimum. Thus, the first test object was chosen to be a continuous conducting right circular cylinder rather than the SCATSAT, the so called "CAN Experiment."

In this simulation the body replacement currents on a cylindrical conducting can were measured for an arc discharge excitation that simulates a punchthrough breakdown of a charged dielectric sheet. The measurements were compared to the calculated response for three cases: (1) an arc discharge of essentially the same geometry as the experiment; (2) a uniform electron emission from the end of the can representing a blowoff discharge, and (3) a capacitative direct injection drive from the end of the can representing an electrical simulation of the blowoff process.* While the

---

*The capacitive direct injection technique is so named because current is injected directly to the test object from a plate which is capacitatively coupled to the object for current return.

computational techniques employed are discussed more fully in Section 6.4, for clarity, we present the results of their analysis in this section.

3.4.2 Experimental

The test geometry is illustrated in Figure 3. The test object is an aluminum can (0.685 m radius and 0.83 m long) which is mounted on a dielectric stand to isolate it from the ground. The capacitor arrangement chosen was developed in an attempt to provide sufficient capacitance for the discharge to give a detectable signal, with a geometry that has a low enough impedance to produce discharge pulses with widths on the order of tens of nanoseconds, and that does not unduly perturb the radiative fields from the arc discharge. The capacitor was placed on the top end of the can, and is an off-center, teardrop-shaped conducting sheet separated from the can by a 1 mil mylar foil. The area of the conducting sheet is about 750 cm^2 and the measured capacitance is 60 nF. A lead from the pointed end of the teardrop goes through a current probe and then forms a spark gap ($\simeq$1 mm) to the bare can on the axis of the can. Five $\dot{B}$ sensors, oriented to measure azimuthal magnetic fields, or equivalently axial and radial surface currents, are located on the can, two on the same end as the capacitor plate and three in a vertical line on the side of the can. (The dot over a quantity such as B denotes a time derivative.) During the experiments, two azimuthal locations of the sensors relative to the capacitive plate were used, one at 180° from the centerline of the plate as illustrated in Figure 3, and the other at 90°. Measurements of the $\dot{B}$ sensor responses were made with hardwire connections and subsequently with fiber optic links to transmit the sensor readings from the can to screenroom recorders. The fiber optic links were designed and constructed by J. Blackburn of HDL (Ref 28) and have a bandwidth of 400 MHz.

The layout of the hardwire connection to the sensors is shown in Figure 3. The balanced lines from the sensor, the balanced to unbalanced transformer (balun), and the initial length of unbalanced line are all inside the sealed can. The unbalanced line is grounded to the can where it feeds through at 180° from the sensor. This line goes directly to the oscilloscope where signals were recorded on film. The location of the instrumentation cable 180° from the sensors, combined with the small excitation of the cable, results in minimal effect on the measured quantities. When the fiber optic data links were used, the transmitter with its balanced input took the place of the balun. The line to the oscilloscope was then nonconductive plastic fiber. Comparison of data

for the hardwire and fiber optic configurations shows agreement within 50% except for the two smallest measured signals which differ by approximately 60%.

(b) SENSOR PLACEMENT

(a) EXPERIMENTAL SETUP. THE THICKNESS OF THE CHARGING CAPACITOR AND GAP SIZE ARE EXAGGERATED TO SHOW DETAIL

RT-16397
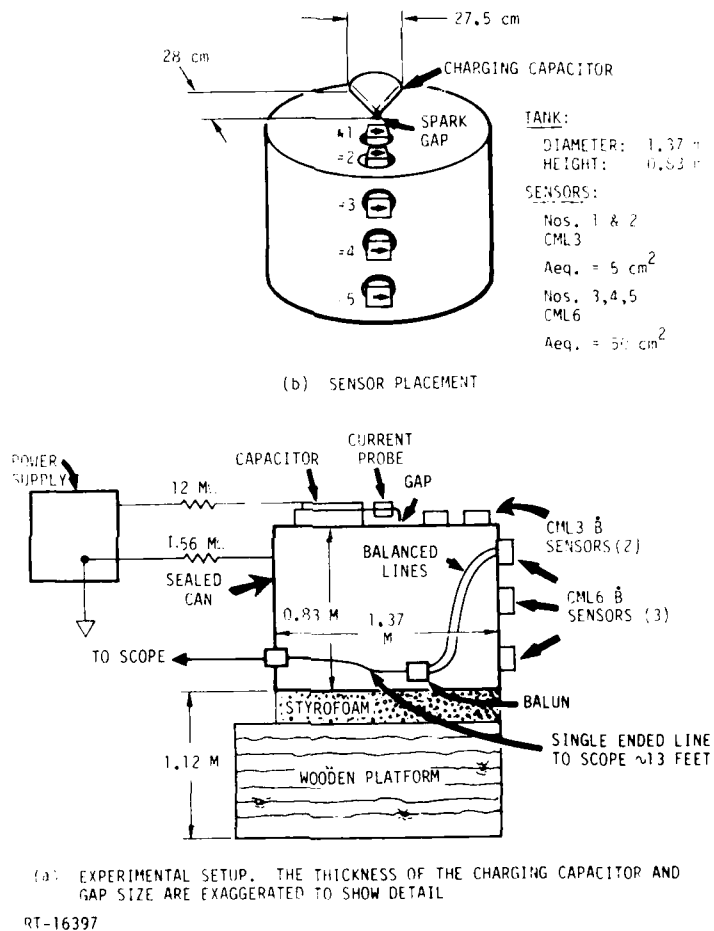
Figure 3. Test configuration

In the tests, the plate was charged slowly by a high voltage supply until a sufficiently high voltage had developed across the spark gap to cause a discharge. The gap width was adjusted so that the discharge occurred at about 1400 volts. The impedance of the charging circuit was sufficiently large (13.5 MΩ) so that it is effectively decoupled from the tank during the discharge.

38

Since the experiment was performed in air, the arc discharge is obviously due to air ionization in the gap, which is not the same as in a dielectric punchthrough discharge. However, the purpose of the present study is to determine the effect of a discharge current pulse, which we measure, on the response of the structure, and not to study the details of the discharge process itself, which is another interesting and important problem, but also very complex. Therefore, the method by which the discharge current pulse is created is not important for this discussion. In addition, a commonly-held theory of punchthrough discharge (Ref 29) indicates that dielectric breakdowns involve the formation of a gaseous channel through the dielectric, which could be similar to air ionization.

Typical measured time histories for the discharge current and for one $\dot{B}$ sensor (#1) at the 90° position (Set B) are shown in Figures 4 and 5. These records were obtained with the hardwire data link. The results using the fiber optics data links were similar in shape but included a higher frequency oscillation ($\simeq$80 MHz) superimposed on the main response curve. We have not determined whether this oscillation is real and it was just damped out in the hardware configuration, or whether it is an artifact of the fiber optics data link.
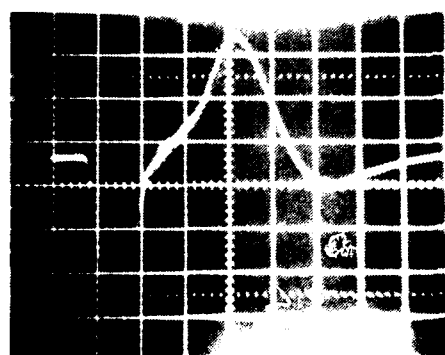
Vertical:	250 A/div
Horizontal:	50 nsec/div
Peaks:	-1000A, +750A
O Crossovers:	70 and 150 nsec

Figure 4. Discharge current waveform, hardwired configuration

The experimental data are summarized in Table 2 for the five sensor locations. The $\dot{B}$ values are shown as measured and scaled to 1000 A peak discharge current to be comparable for all three tests.

The measured $\dot{B}$ values on the side of the can were relatively small and close to the noise level of the instrumentation. Hence, one should not attach too much

significance to the differences between the indicated values on the side of the can and their spatial dependence for the hardwire and fiber optics instrumentation. Also, since we are comparing $\dot{B}$ values, rather than B or current, a relatively small difference in the assumed shape of the discharge pulse used in the calculation for the arc discharge could result in factors-of-two differences compared to experiment. Since, as is seen later, the experimental and calculated values on the side of the can are over an order of magnitude less than for outward emission of charge and for capacitive direct injection drive, the uncertainties regarding the effect of the hardwire instrumentation and the discrepancies between the measured and calculated $\dot{B}$ values do not alter the major conclusions of this study.
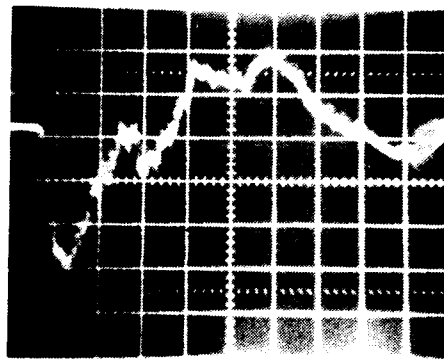
10 mV/div
20 nsec/div
Approximately 70 tesla/sec-div

Figure 5. Response measured by CML3 sensor at position 1

3.4.3 Calculations

Three sets of calculations were made using the fully-dynamic finite-difference SGEMP computer codes SABER (three dimensional in cylindrical coordinates, Ref 30) and ABORC (cylindrically symmetric, Ref 31).

The first calculation used SABER to simulate the experimental arc discharge problem. However, to avoid extremely small computational time steps, the distance between the can and the plate was made 1 cm. These results are scaled to the test configuration by the methods that are discussed in the next section and in Appendix A. Since the capacitance and inductance of the simulated discharge setup would not produce the experimental pulse shape, the plate was driven at the discharge point with a current pulse with the same shape as the experimental discharge current (Figure 4). Skin currents on the can in the vicinity of the five sensors were calculated for both the 180° and 90° positions relative to the areas and symmetry of the plate. The skin

40

currents, especially for points close to the discharge point, roughly follow the discharge pulse. The peak rate of change of the currents were obtained graphically, then converted to $\dot{B}$, and finally scaled. The scaled results are given in Table 2.

Table 2. Measured and Calculated $\dot{B}$ Values on Can

Data System	Sensor Location Relative to Line of Symmetry of Capacitor Area	Measured Peak Discharge Current (Amps)	1	2	Sensor 3	4	5
			Measured Peak $\dot{B}$ (Tesla/sec)				
H.W.[a]	180°	1000	490	140	16	16	17
F.O.[b]	180°	720	460	58	8.2	4.5	4.7
			(640)[c]	(81)[c]	(11)[c]	(6)[c]	(6.5)[c]
H.W.[a]	90°	860	820	160	18	19	18
			(954)[c]	(186)[c]	(21)[c]	(22)[c]	(21)[c]
			Calculated Peak $\dot{B}$ (Tesla/sec)				
	180°	d	90	16	2.7	1.2	0.8
		e	900	160	27	12	8
	90°	d	225	45	5	1.4	0.6
		e	2250	450	50	14	6
Capacitive drive from end of can		e	4.3×10^4	1.8×10^4	1.3×10^4	0.53×10^4	0.58×10^4
Outward emission from end of can		e	0.37×10^4	0.56×10^4	0.59×10^4	0.32×10^4	0.25×10^4

[a]H.W. = Hardwire

[b]F.O. = Fiber Optics

[c]Scaled to 1000 amps peak discharge current

[d]Calculated results are scaled to the same peak rate of change of the plate potential as in the arc discharge experiments

[e]Calculated results were scaled to the same peak rate of change of driving current as in the arc discharge experiments.

The ABORC code was used to calculate the body responses for a uniform emission of electrons from the end of the can. This calculation is supposed to approximate the outward emission of charge during a discharge although such emission is undoubtedly not uniform over a very large area. A triangular emission pulse (10 ns up and 10 ns

41

down) was used because information in the literature indicates that this is the shortest probable discharge pulse during a dielectric discharge. The emission current density was kept very low to avoid space-charge-limiting effects. Space-charge-limiting is not expected to be significant in dielectric discharges produced by electron irradiation because the dielectric surface at breakdown will usually have a negative potential with respect to the surrounding plasma. Therefore, the emitted charge escapes to infinity. The calculated responses at the locations of the sensors followed the triangular emission pulse. The calculated skin currents were differentiated graphically and scaled. The scaled values are given in Table 2. Since this problem and the capacitive drive simulation are cylindrically symmetric, there is no azimuthal dependence on the body current produced and only one set of calculations are given in Table 2 for each of these two problems.

A capacitive-drive simulation of the above outward emission was made using SABER. The capacitor plate had the same diameter as the can and was placed on the cylinder axis about 35 cm from one end of the can. The driver was a current source along the axis of the can from the can to the plate. Again, a triangular pulse (10 ns up and 10 ns down) was used in order to directly compare the response produced by the capacitive drive to that of the outward-emission case. The calculated responses followed the pulse. The graphically-differentiated skin currents were converted to B and scaled. The scaled results are shown in Table 2.

3.4.4 Scaling of Responses

The physical problems simulated for each of the three calculations differ significantly from the arc discharge experiment in terms of peak driving current, shape and duration of the pulse, and the distance of the capacitor plate from the can in the arc discharge calculation. Therefore, to realistically compare the results, the calculated results must be scaled to the experimental conditions in a consistent manner.

When comparing the body currents due to the outward emission of charge and the capacitive drive with those from the arc discharge experiment, the quantities of interest are the relative body currents if the total charge that is emitted outward is the same as the punchthrough charge and if the discharge times are comparable. In other words, the calculated body currents for outward emission and capacitive drive should be scaled to the experimental arc discharge problem by the peak current in the pulse. Actually, since $\dot{B}$ values are compared in Table 2, the scaling was done for these cases by peak rate-of-change of the discharge current, $\dot{i}_p$.

For the arc discharge calculation, the discharge pulse had the same shape as the experimental discharge pulse but its magnitude was different. The capacitance between the plate and the can was smaller in the calculations than in the experiment due to the greater plate separation distance. In Appendix A, an analysis is given for the response of a simple lumped-element model of the plate-can system. This analysis indicates that there are two logical methods for scaling the body currents: either proportional to the peak emission current (I_p), or proportional to the rate of change of the plate potential (V_p). Which case is more correct depends on the ratio of the capacitances between the plate and the portion of the can directly underneath the plate (C_p) and between the portion of the can underneath the plate and the remainder of the can. Because this ratio varies for different points on the can, it is not clear which scaling method is more appropriate for the different sensor locations. To help clarify the situation, the arc-discharge calculation was repeated, keeping all parameters constant except for a 33-fold increase in the dielectric constant in the 1 cm gap between the plate and the can. The skin currents on top of the can (sensor positions 1 and 2) were affected only slightly by the 33-fold change in the capacitance. Therefore, these currents evidently more closely with the driving current I_p than with the rate of change of the dipole potential, $\dot{V}_p \cong I_p/C_p$. However, far from the discharge point, at sensor location 5, the factor of 33 change in capacitance changed the skin currents by a factor of 6. At sensors 3 and 4, the ratio of the skin currents was between 2 and 4. Thus, the scaling for these positions is apparently a mixture of scaling by I_p and I_p/C_p. In Table 2, both methods of scaling are shown for comparison for the arc discharge calculations.

3.4.5 Discussion

The following observations can be made about results presented in Table 2.

1. When the experimental values are scaled to the same peak discharge current (1000 A), the measured $\dot{B}$ values at the same sensor locations are comparable (within about a factor of 3) for both the hardwire and fiber optic data for the 180° orientation and the 90° orientation. The largest relative discrepencies are on the side of the can where the $\dot{B}$ values are small and close to the noise level of the instrumentation. Hence these differences are probably due mainly to the difficulty of obtaining good absolute values.

43

2.   There appears to be a small but noticeable effect, less than a factor of two, in both the experimental and calculated arc discharge results at sensor 1 due to the asymmetry of the capacitor plate relative to the sensor locations. The sensor at 90° shows the largest response, which is reasonable since this position is closer to the sides of the capacitor plate than the sensor at 180°, and the local return currents should be larger close to the plate.

3.   The two methods of scaling the calculated arc discharge currents roughly bracket the experimental data, but scaling by $\dot{I}_p$ appears to give somewhat better agreement than scaling by $\dot{V}_p$. The indicated differences between the spatial variation of the calculated $\dot{B}$ values on the side of the can compared to experiment are probably due to the inaccuracies of measuring values whose magnitude is close to the noise level.

4.   The calculated and measured $\dot{B}$ responses due to an arc discharge increase rapidly as one approaches the location of the breakdown. This result is reasonable since the magnetic field around a thin beam of current varies inversely with the radial distance from the beam. Very close to the breakdown point the fields could become comparable to those due to outward emission or capacitive drive.

5.   The calculated responses on the side of the can (Sensors 3, 4, and 5) for outward emission are comparable to, but around a factor of 2 less than, those due to the capacitive drive. The smaller magnitude for the outward emission probably results because the electrons are emitted with a cosine angular distribution so a significant fraction of the electrons have only a small velocity component normal to the end of the plate and are not as effective in producing return currents as the capacitive-drive current. The responses for sensors 1 and 2 are less than for sensor 3 for outward emission because the electrons are emitted uniformly in area from the end of the can so there is less total emission inside the radii corresponding to sensors 1 and 2 than for sensor 3.

6.   The responses due to the outward emission and the capacitive direct injection are more than an order of magnitude larger at all five sensor locations than the experimental and calculated responses due to the arc discharge. This ratio is even larger at the positions farthest away from the excitation point (sensors 3, 4, and 5). This finding is the most significant result of this experiment. Thus, if a significant fraction (say, $\cong 10$ percent) of the charge trapped in the dielectric is emitted outward during a discharge, the body currents generated by this outward emission will be larger

than those generated by punchthrough of the remaining charge to the substrate, except possibly very close to the punchthrough spot. Therefore, in simulating the surface replacement currents which flow at points of interest reasonably far from the discharge point, a capacitive direct injection drive technique should be used. Even close to the discharge point, the electromagnetic fields due to punchthrough would be reasonably simulated by the current flowing through the pulser wire in the capacitive direct injection technique, assuming the punchthrough and capacitive-drive currents are the same. To simulate coupling of a punchthrough discharge into a nearby cable, the drive point for the capacitive direct injection could be placed close to the cable where the discharge might occur. However, still to be answered is the question of the fraction of the discharge current that is emitted outward versus what punches through, and thus the validity of the proposed simulation technique. Answering this question will require careful measurement of the flow of charge during breakdown to determine the relative amounts that flow to the substrate, to the edges, and that is emitted outward.

4. SCATSAT DESIGN AND CONSTRUCTION

The electrical test program was structured around a test object which reproduced with reasonable accuracy the important electromagnetic features of the P78-2 SCAT:1A spacecraft. This section will describe the design process for that model, the features of the P78-2 which constrained the design, and the final implementation.

4.1 DESIGN PHILOSOPHY

The first and key consideration was what size to make the object. The P78-2 is 1.7 m in diameter by 1.8 m high with instrumentation booms of from 2 to 7 meters and a 100 meter long experiment antenna. A smaller model than this was desirable to facilitate handling (reasonable size and weight) and to reduce the space requirements in the laboratory.

But it was necessary for the model to be large enough so that small details which are important to the EID response could be faithfully reproduced. Also, too small a size causes instrumentation and frequency range problems. Thus, something of the order of half scale was about as small as was reasonable for the main body. Experience with other satellite models in the approximately one to one and a half meter size, both from construction and electrical testing, were also important considerations. Also, a model of this size will fit conveniently in one of the vacuum tanks with electron sources which have become available since this program was begun to facilitate electron spraying experiments to validate the electrical techniques developed. The final size of 65 percent was chosen for the model from material considerations, notably the ready availability of ¾" honeycomb for constructing the simulated solar array substrates.

After establishing the size of the model, the key P78-2 features which would be incorporated were selected. These included the following:

1. General structural and electromagnetic construction as near that of P78-2 as possible.

2. An experiment penetration into each major compartment of the spacecraft.

46

3. One boom penetration.

4. The solar array penetration.

5. The forward antenna penetration.

6. The reference band penetration.

7. The experiment antenna penetration.

8. Main cable layout as in P78-2 including equipment boxes and overall shielding.

These take care of the major electromagnetic features. The surface treatments on the exterior were also planned for modification to permit electron spraying experiments.

The level of detail which must be included to accurately reproduce EM penetration must also be considered. The cables were constructed in the same manner as the SCATHA spacecraft, namely all shielded wires possess an overshield wherever the cables are outside of the EMI enclosure. However, fewer wires are included in the model than in the real spacecraft. The solar array pickup wires are routed and shielded as they are on the SCATHA and terminated at the correct location. The belly band segments which close out the equipment compartments are grounded as in the SCATHA. The experiment penetrations have their edges sealed with finger stock to simulate real experiments. Of course, no electronics are included so that wires in the simulated bundle are terminated with resistors at the experiment boxes. The shield termination scheme is similar to that employed in the real satellite.

4.2 P78-2 DESCRIPTION

This section describes the essential features of the SCATHA P78-2 spacecraft as gleaned from drawings and a meeting at Martin-Denver, September 14, 1977 from which the model was prepared. As the satellite was still in process of assembly, it is possible that some of the charge elements were subsequently changed. The discussion will be divided into two parts: electromagnetic considerations and surface treatements.

4.2.1 Electromagnetic Considerations

The P78-2 is atypical of most present satellites in its EM configuration because it is a well-sealed Faraday cage. However there is a trend toward such designs in current

47

and future military satellites such as FLTSATCOM and DSCS-III. The structure may be thought of as being in three parts: a topmost cavity inside the top solar array, a central equipment bay (called "between decks" by Martin), and a lower cavity inside the bottom solar array. The latter two cavities are formed around a central thrust tube so that they are doughnut shaped. These two cavities comprise the "Faraday cage" and very great care appears to have been taken in sealing it up (Figure 6). For example:

1. The basic cavity is formed by the thrust tube (metal sheet), the inner face sheet of the lower solar array (metal sheet), the aft thermal closeout (metal sheet), a belly band around the equipment bay exterior (metal sheet), and a top EMI cover (a welded mesh of 0.001 inch wire on ½ inch centers welded to a frame). Minimum metal thickness is 0.005 inch except for the mesh.

2. Great care has been taken to seal all metal joints through the use of thin metal shims (with a maximum gap length of 3/4 inch) between the belly band and solar array face sheet, EMI finger stock surrounding all experiments which look through the belly band, solar array, or thermal closeout, and the use of frequent welded ground straps on bonded doublers, etc.

3. Penetrations such as the passage of solar array wires into the lower cavity are shielded either with braid shields or conductive tape to the face sheet over unshielded wires. Even the blocking diodes have an aluminum cover on them. The pickup cable joining the various strings is similarly shielded. The only exception that was found to this during our survey was the wire from the "Reference Band," a 1 inch wide, circumferentially complete band around the base of the spacecraft on the outside. This wire is shielded (RG 400), but the shield begins about a half inch inside the face sheet and is only pigtailed to the face sheet ground. Also, there is about a 3/4 inch hole (allowed by specification) around the wire where it penetrates the aluminum face sheet.

4. All system or experiment cables which enter the Faraday cage are wrapped with an overall shield consisting of a lengthwise wrap of 0.001 inch aluminum foil, with a 1/2 inch overlap doubled back, then a string tie over the shield. The shield is grounded to the Faraday cage where it enters and at connector backshells at the other end (Exception: SC2 boom experiments are not grounded to the shields. The overall shield floats at the far end.)

48

The method of terminating shields is to solder a length of braid to the back shell and overlap the foil on this braid, then apply pressure via the string tie.
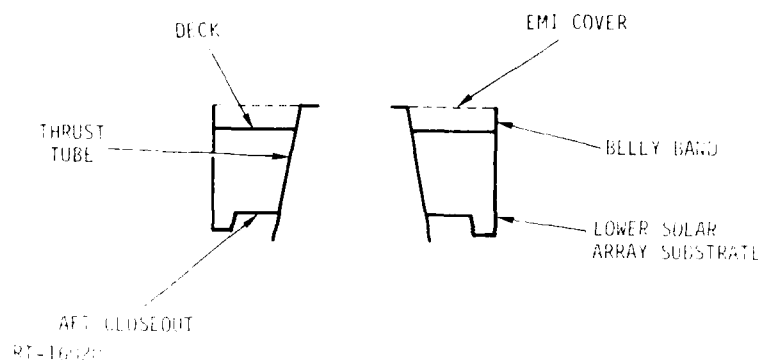
Figure 6. Lower part of P78-2, EMI tight enclosure

The upper cavity (inside the top solar array) is shown in Figure 7. It is not intended to be a Faraday cage. It is, however, surrounded completely by metal, i.e. the top solar array face sheet (metal sheet), the top thermal close out (metal sheet, 1/2 mil stainless steel), the EMI cover, and a thermal closeout over the top of the thrust tube (goldized mylar, gold toward the bottom). The grounding of the top thermal closeout to the solar array face sheet is via a metal ring, but no great care is taken to ensure a metal to metal contact. The grounding of the gold to the thrust tube is similarly uncertain. Thus, the top cavity will have some shielding properties though it is not intended to be a Faraday cage.
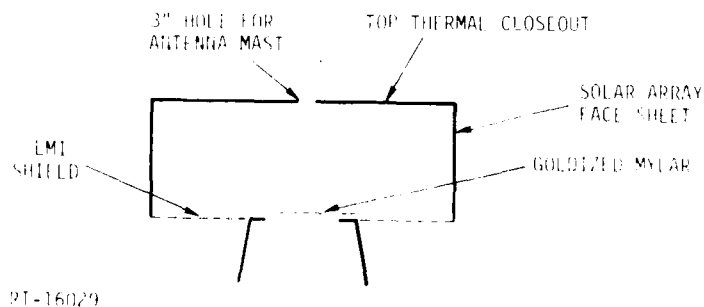
Figure 7. Top non-EMI tight cavity

49

Solar array wires from the upper solar array are shielded from the point where they enter the Faraday cage to the Power Control Unit. They are unshielded outside the cage, i.e. inside the top cavity.

All system wires are also individually shielded, even inside the Faraday cage as well as inside the overall shielded external cables. There are no unshielded wires in the harness at all. The method of terminating the individual shields is to expose a length of the shield near the connector, then use the same overbraid soldered to the back shell to pick up the individual shields, as shown in Figure 8. This is done with pressure as in the case of grounding the foil over all shield. This treatment is used at both ends of all cables.
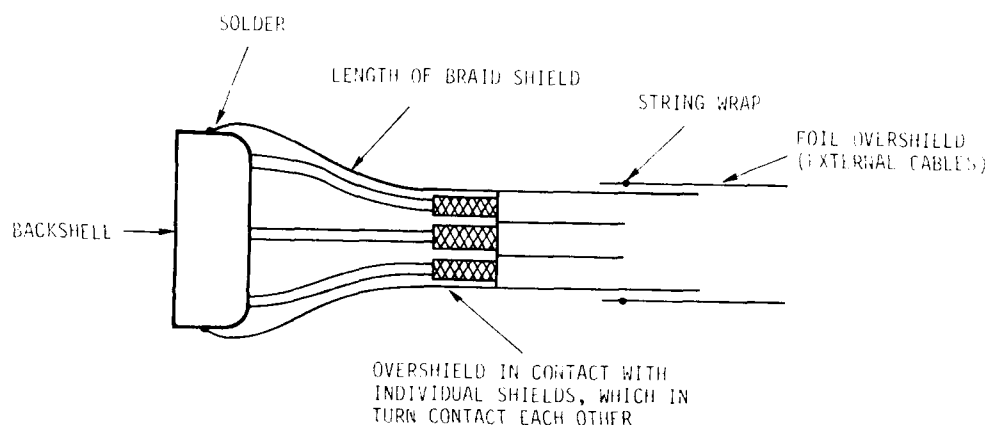
RT-16030

Figure 8. Treatment of cable shields

In conclusion, the spacecraft is extremely well designed from an EM tightness standpoint. Such a design has the major advantage that external disturbances are not likely to be coupled into interior circuits. On the other hand, if one wants to study internal effects one may not see much. However, discharges may still be induced by high energy electrons which penetrate the thin top thermal closeout and embed themselves in interior dielectrics, or through discharges of electrons which are stopped in the mylar which forms the manhole closeout.

4.2.2 Surface Treatments

External:

In general, the top surface of the satellite is to be conductive, the bottom surface nonconductive, and the sides a mixture.

50

The top thermal closeout is a 1/2 mil stainless with a thin layer (3000 Å) of gold, painted with an unspecified (at the time of our visit) pattern of black conductive paint (~1 mil thick). There is also an area ~17 x 18 inches that is the same construction as the EMI grid, i.e., 1 mil wires on 1/2 inch centers. Behind the grid is a cone which goes down into the deck mounted SC5 experiment box. The cone is made of 1/2 mil stainless with gold flash inside and out.

The bottom closeout is aluminum, 0.005 inch minimum thickness, painted on the outside with a nonconductive organic paint (0.001 inch thick) to provide the required nonconductive surface, except for an unpainted area of 7.9 inch radius around the SC7-3 experiment.

The side of the satellite is a mixture of conductive and nonconductive areas achieved in several ways. In general, the belly band is conductive (metal) while the solar array exterior is nonconductive (quartz cover plates over the solar cells). However, there are required conductive areas which extend into the solar array substrate. These are achieved by placing a metal foil in the area and then painting it with conductive paint. The cells are excluded from these regions. One exception to this is the conductive region around SC9. The cells extend into this region and the ground plane is achieved by using conductive transparent coatings on certain of the cover plates. The cover plates are connected to one another, then to the inside aluminum face sheets by means of tiny, redundant wires. On the belly band, a nonconductive area is required around SC1-1 and -2 for a distance of 28 cm. This consists of a second surface mirror of Teflon with vacuum deposited silver on the inside surface. Figure 9 shows the nonconductive (outlined with cross hatch) and conductive areas on the side, locating specifically the areas just described. The drawing shows the side of the cylinder unrolled so that it is flat.

The five instrument booms and the antenna mast are made of graphite epoxy. The surface is made up of bands of a thin platinum flashing (reported to be Angstroms thick) about an inch wide with 1/4 inch spacing between bands. The experiments (or antenna cage) at the ends of the booms are grounded to the main structure via the cable overall shield with the exception of SC2-1 and SC2-2 which are floating.

Internal:

The inside face sheets of the solar array substrates are bare aluminum, except for a band of black, nonconductive paint a few inches wide at the lower end of the bottom array. The deck is coated with black, nonconductive paint on top and bottom. The

thrust tube is V.D. gold inside (exposed to space) and black, nonconductive paint outside (inside the cavity). The thermal closeouts are bare metal inside. The manhole thermal closeout is goidized film, gold toward space, film inside.
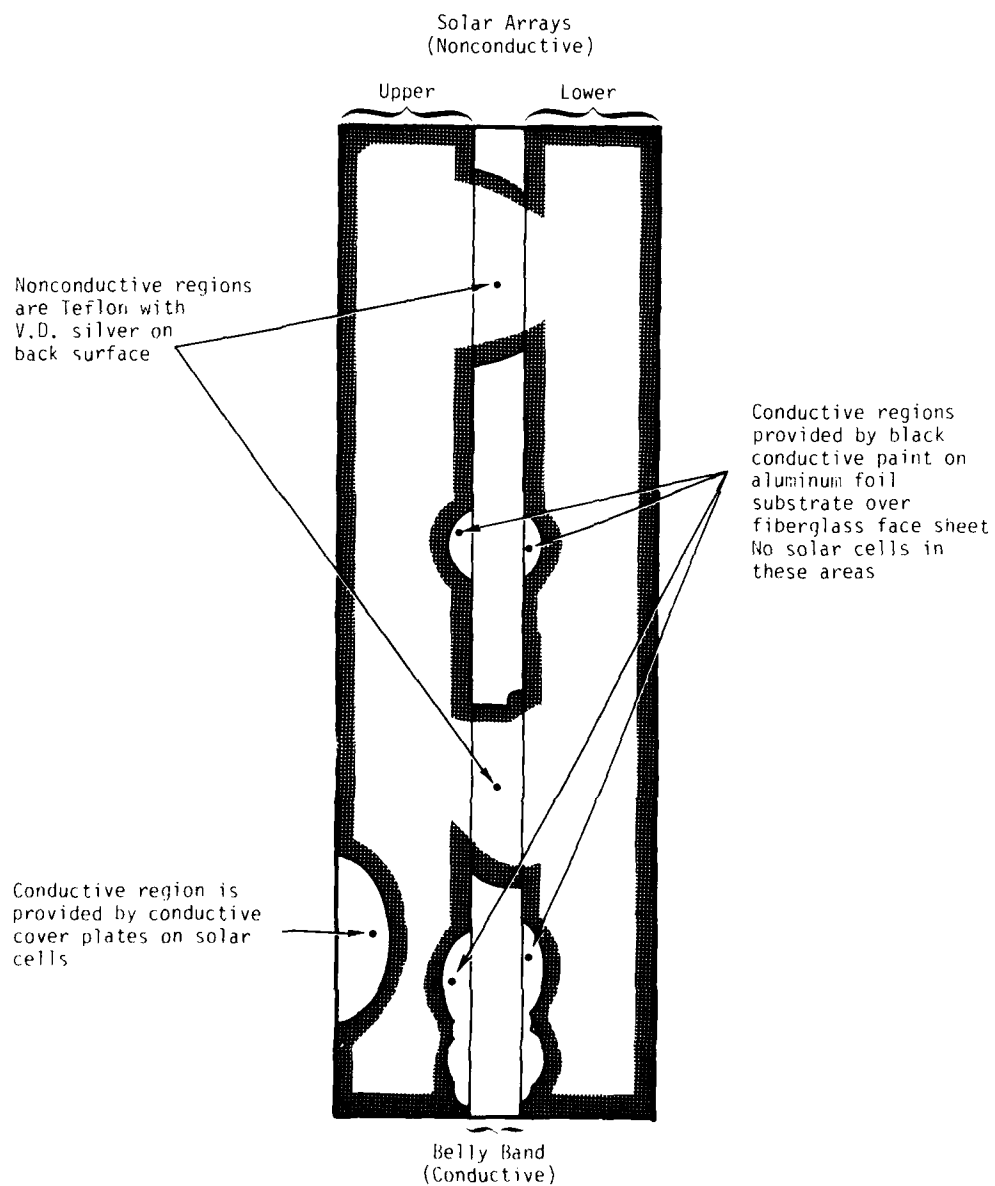
Figure 9. Surface treatments

4.2.3 Miscellaneous

Solar Array:

The solar array consists of 2 x 4 cm cells, two in parallel by 68 cells long, per string. Strings begin and end at various places on the array. The return wires are routed along the underside of the substrate directly underneath the cell strings as shown in Figure 10. The power end of the string (+) goes directly to a pair of blocking diodes and then the power and return are twisted together in the pickup string. Connectors are mounted on the array back at approximately 215° upper and approximately 200° lower. Cables go directly from there to the PCU. The gap between strings is 0.015 to 0.020 inch and the gap between ends is one cell, 2 cm.
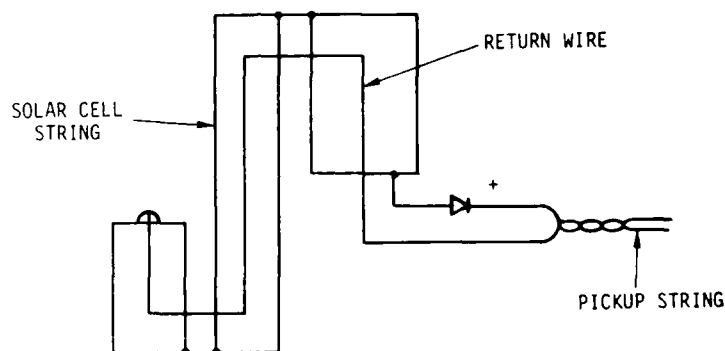
RT-16032

Figure 10. Solar cell string

Grounding:

The primary and secondary power use a single point ground located at a point on the lower face sheet of the main deck near the PCU. Signals are routed through the chassis for return.

The features of the cable harness in the P78-2 were not fully determined at the time of our visit especially in terms of the detailed cable layout. It was our perception that the P78-2 (and SCATSAT) would have a main bundle running around the inside of the central tube at deck level, with a branch into each of the seven bays both above and below the main deck, a branch going to the top antenna array, and a branch to an "experiment" box just under the forward thermal closeout. The latter two cable

53

branches are wrapped in aluminum foil, well grounded at both ends. All wires in the cable bundle were shielded in the model, as in the real satellite. The various experiment and housekeeping electronics boxes were simulated with simple chassis boxes with their locations determined from P78-2 drawings as they were installed.

4.3 SCATSAT MODEL

The 65 percent scale model of the P78-2 dubbed SCATSAT, is shown in the drawings of Figures 11, 12, and 13. Figure 11 is a side view showing the major dimensions of the SCATSAT, the construction of the tripod and antenna, the solar array substrate construction, details of the belly band grounding and reference band construction, and the thermal closeout construction. Figure 12 is a top view showing rib and bay locations, boom dimensions, and the EMI screen. Figure 13 shows a view of one of the ribs with details of the boom mounting and belly band.
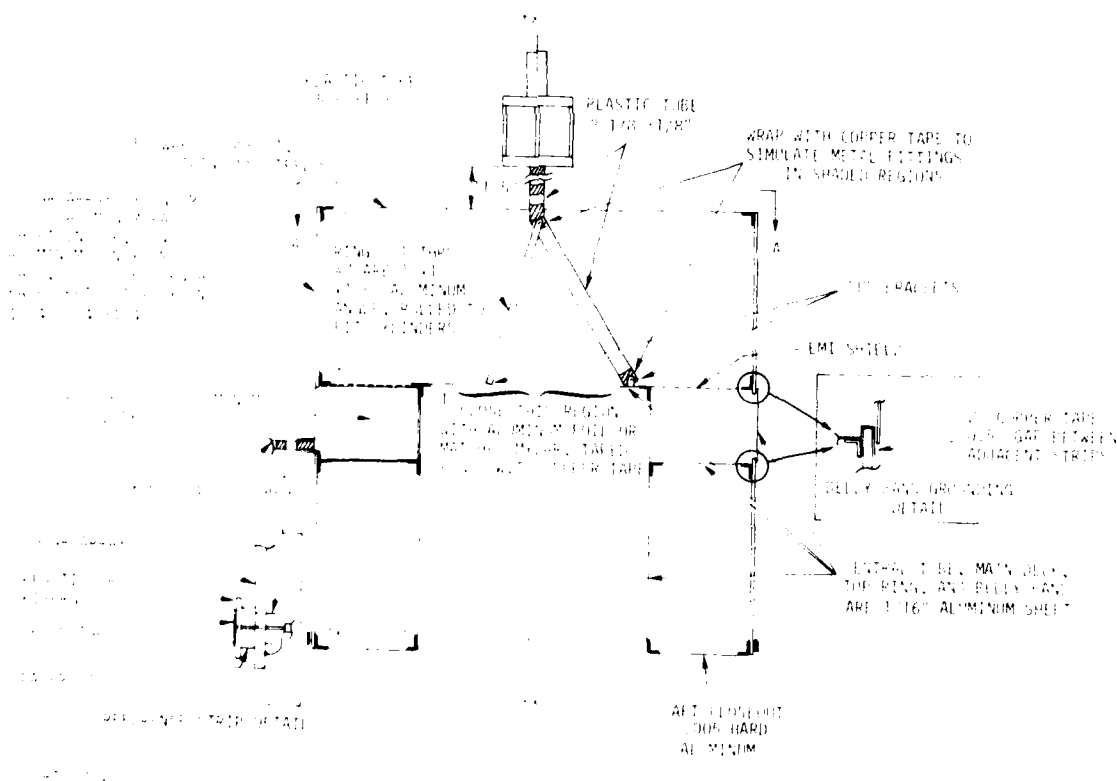
Figure 11. General SCATSAT layout
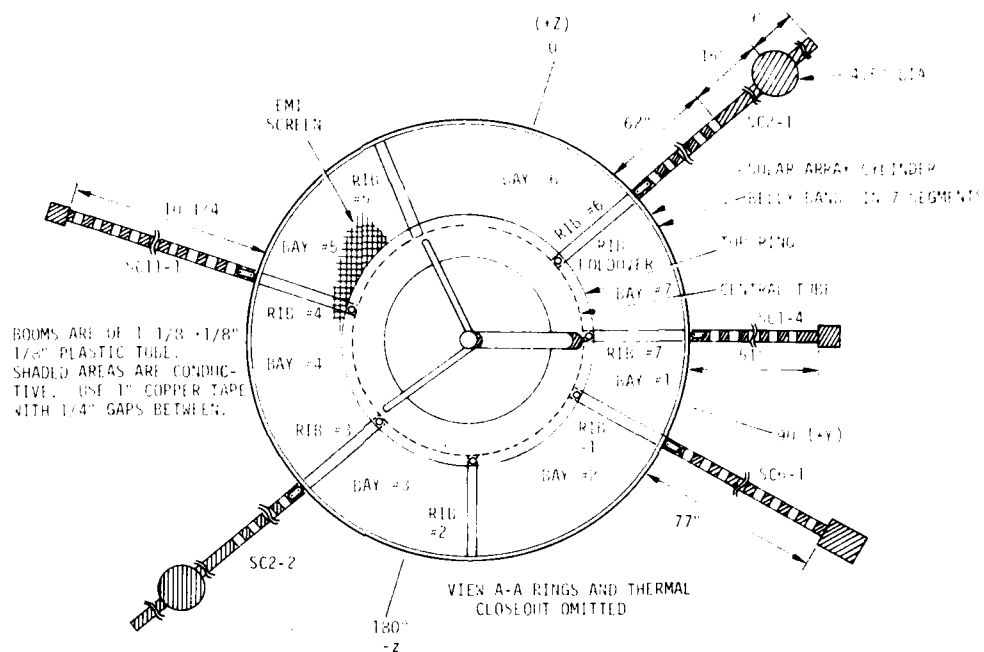
RT-17147

Figure 12. Top view of SCATSAT
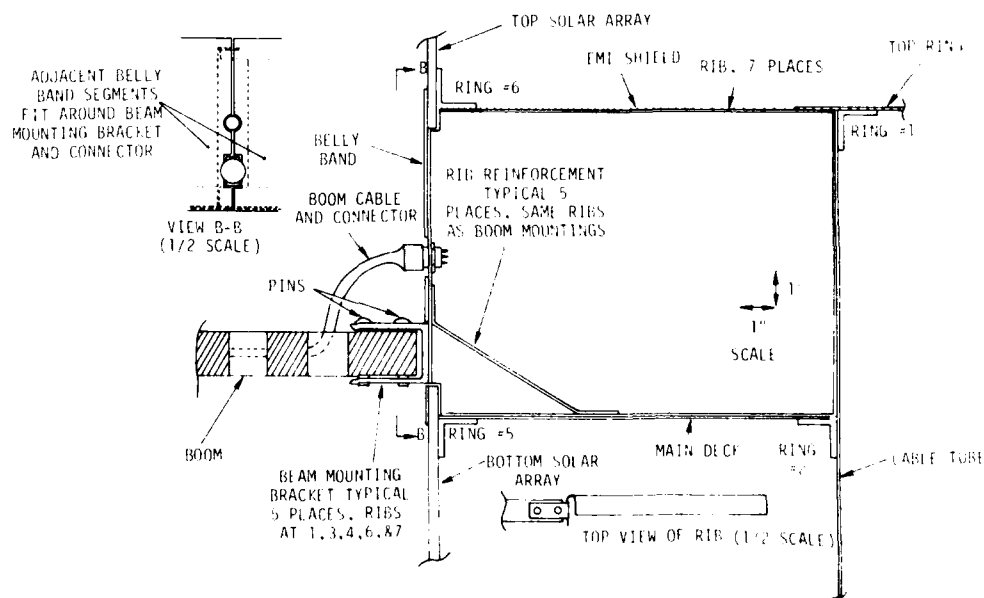
RT-17149

Figure 13. Detail of rib and boom mounting

A photo of the finished SCATSAT is shown in Figure 14 with the top thermal closeout in place and in Figure 15 with the closeout removed so that internal details can be seen.

Details of the model will be discussed in the following sections.
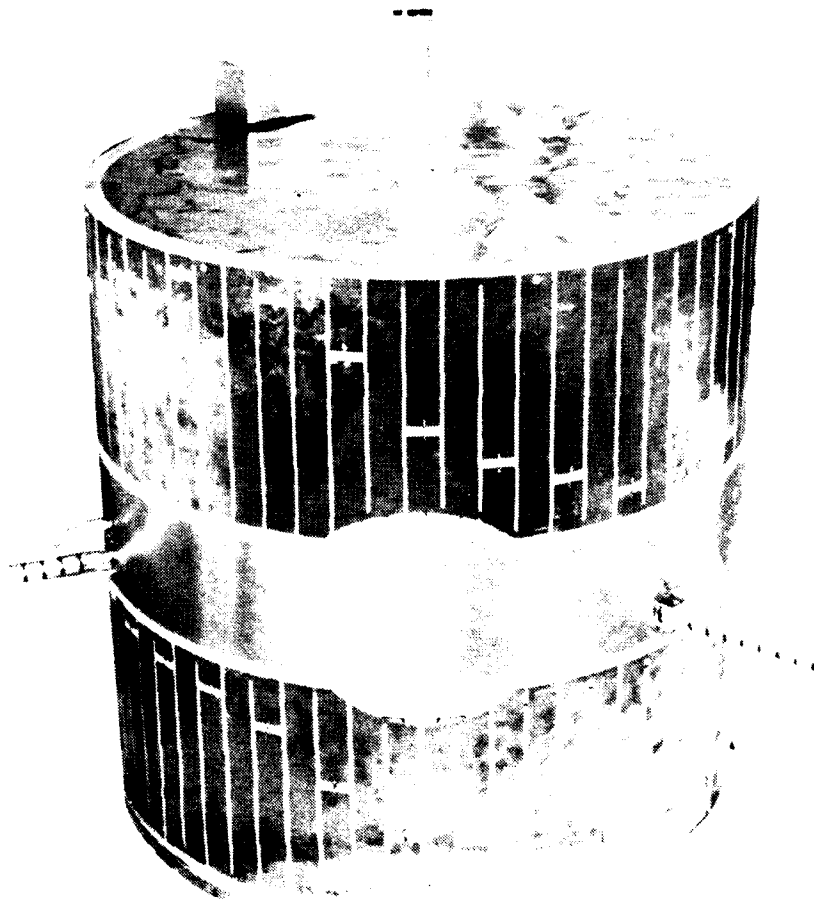
Figure 14. SCATSAT side view
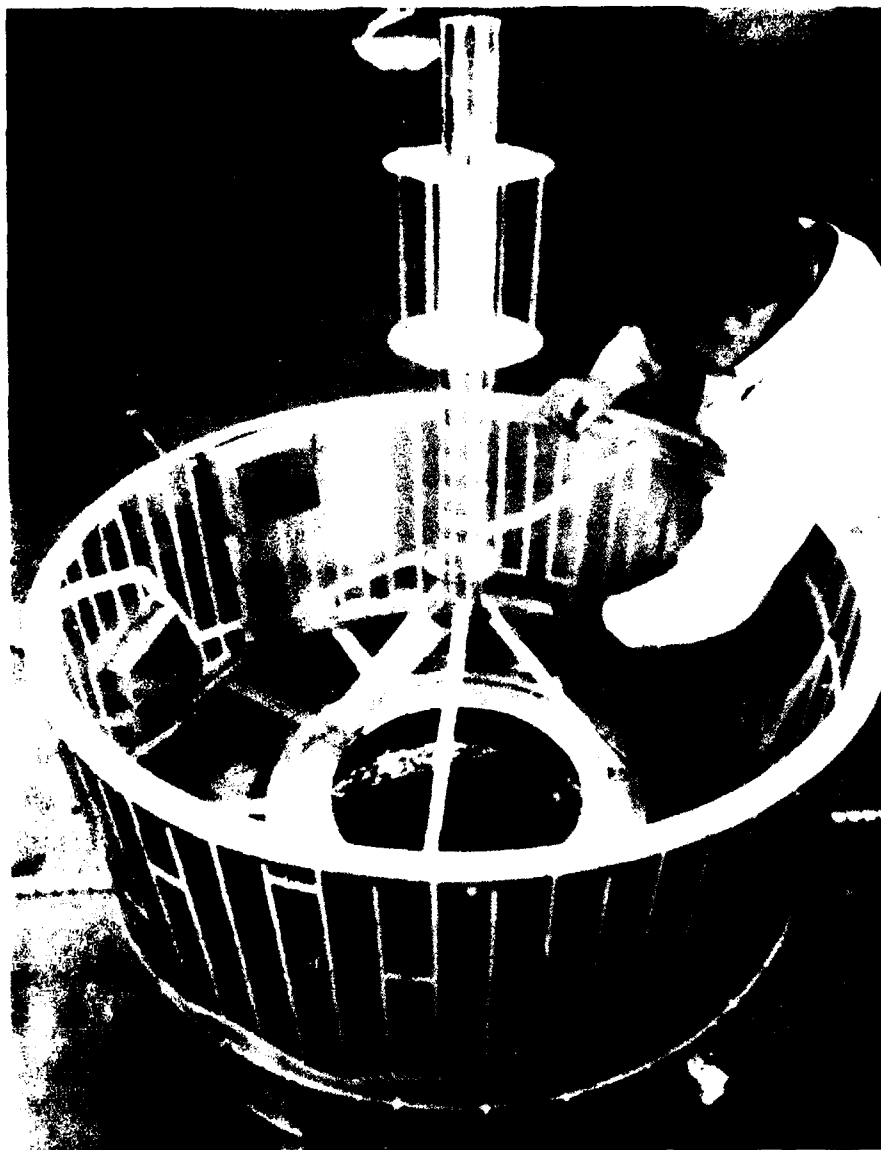
Figure 15. Interior details of SCATSAT

4.3.1 Forward Antenna Penetration

A good view of the forward antenna is seen in Figure 15. In keeping with the level of detail required to adequately simulate the EM characteristics of the P78-2, the SCATSAT antenna simulation includes the main structure, which is grounded via the cable shield, but does not include the actual radiating elements. Thus, coupling to the cable shield but not to the center lead is simulated. The RF lead is a coaxial cable and

57

is wrapped with a spiral wrap of double sided aluminized mylar tape as an overshield. The overshield is grounded to the connector backshell at the antenna end and to the main bundle cable wrap where the RF cable enters the bundle. This is a simulation of the P78-2 treatment. The tape used was supplied by Martin Marietta and is the same as used on the P78-2.

The mast is of plastic tube to simulate the basically nonconductive graphite epoxy and is wrapped with aluminum tape to simulate the bands of metal flashing on the mast.

4.3.2 Experiment Booms and Antenna

The five experiment booms were simulated with plastic tube and bands of aluminum tape as was the forward antenna mast. A shielded cable was routed inside each boom and each of these cables was wrapped with an over shield of the same aluminized tape as used on the forward antenna lead. This is a simulation of the real treatment. Four of the booms had an external only simulation where the overshield was appropriately terminated at each end, but the cable itself was simply dead ended, i.e., did not penetrate SCATSAT. The fifth boom, SC1-4 had a piece of real spacecraft cable in the boom and this cable penetrated the SCATSAT into bay 7. The overshield of SC1-4 was terminated to the connector backshell while the cable shield and center wires were brought through the connector without being grounded. The use of a connector is not realistic but these are a necessary addition to SCATSAT so that the booms could be removed for transport. The overshield was grounded to the "experiments," except for SC2-1 and SC2-2 which were left floating. The experiments were simulated by metal boxes.

The 100 meter experiment antenna was simulated by an inductor formed of ~65 turns of number 22 wire around a 1.4 inch diameter by 65 inch long plastic tube and then loaded with a 60 cm diameter plate on the far end to provide a structure where resonant frequencies approximated what we estimated to be those for the real antennas. The satellite end was attached to the satellite body to simulate a low impedance termination to the satellite.

4.3.3 Cable Bundles and Equipment Boxes

The complex cable harness of the P78-2 was simulated by a cable bundle which included the major branches of the P78-2 harness but which eliminated minor branches unless they were considered especially important. The basis for the cable design was

58

MMC drawing 85800000012 "Checkout Diagram - Electrical System, Airborne." This massive drawing (55 pages) was studied in detail to create a table which divided the spacecraft into major regions and then determined the total number of wires interconnecting the regions. This gave a simplified "map" of the ends of groups of wires and the weight (or number) of wires in that group. The intent was to simulate both of these parameters in creating the SCATSAT harness. However, by just including a cable to represent each group in the harness yielded the desired complexity without adding additional cables to simulate weight.

In each region, the cables were terminated in a box which represented one or more boxes in that region. The various termination points (boxes) are shown in Figure 16 and/or are described in the following list. Two photographs of the boxes are shown in Figure 17.

1. Boxes 1-7. One in each of the seven compartments on top at the main deck, in the top Faraday cage.

2. Boxes 3B-6B. Four boxes under the respective numbers listed above, inside the lower Faraday cage.

3. 4/5 Aft. A box mounted against the lower thermal barrier, under Rib 4.

4. 1 Forward. Mounted under and against the top thermal barrier, above Bay 1.

5. 5 Forward. Mounted outside the satellite, above the top thermal barrier, above Bay 5.

6. 7 Boom. At the end of the boom on Rib 7.

7. ML12-3, -4, -6. Passing through the belly band in Bay 6, with conductive finger stock surrounding the penetrations.

8. Omni antenna. Mounted on top of a tripod mast passing through the blanket. Conductive areas consist of two discs separated by four posts.

9. SAT output. From the top solar array simulation.

10. SAB output. From the lower solar array simulation.

11. SC-1-1, -2. Boxes penetrating the honeycomb material, with finger stock to minimize leakage.

12. Reference band. A metal band spaced away and insulated from the lower edge of the lower solar array cylinder.

13. A1M. A simulation of an open ended cable connected to the apogee insertion motor prior to its ejection.
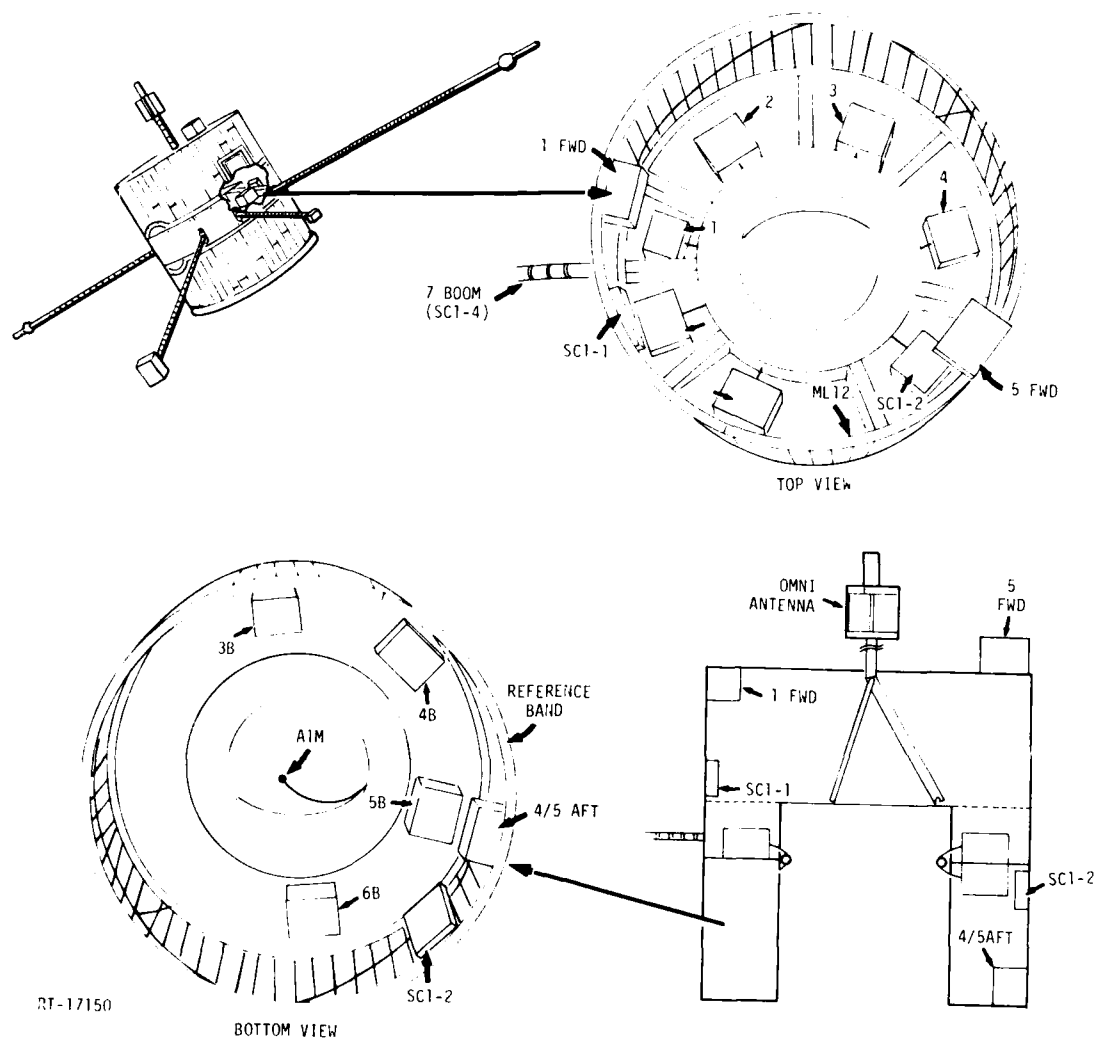
Figure 16. Locations of simulated experiments and equipment boxes

All interconnecting cables were shielded as are the P78-2 cables. The majority of the cable used was a small braided shielded type coaxial cable with plastic cover, similar to RG174. The center wire was unused, using the shield braid for terminations. One length of larger type RG58 coaxial cable connected to omni antenna with box 1. The center wire was also unused on this cable.

60
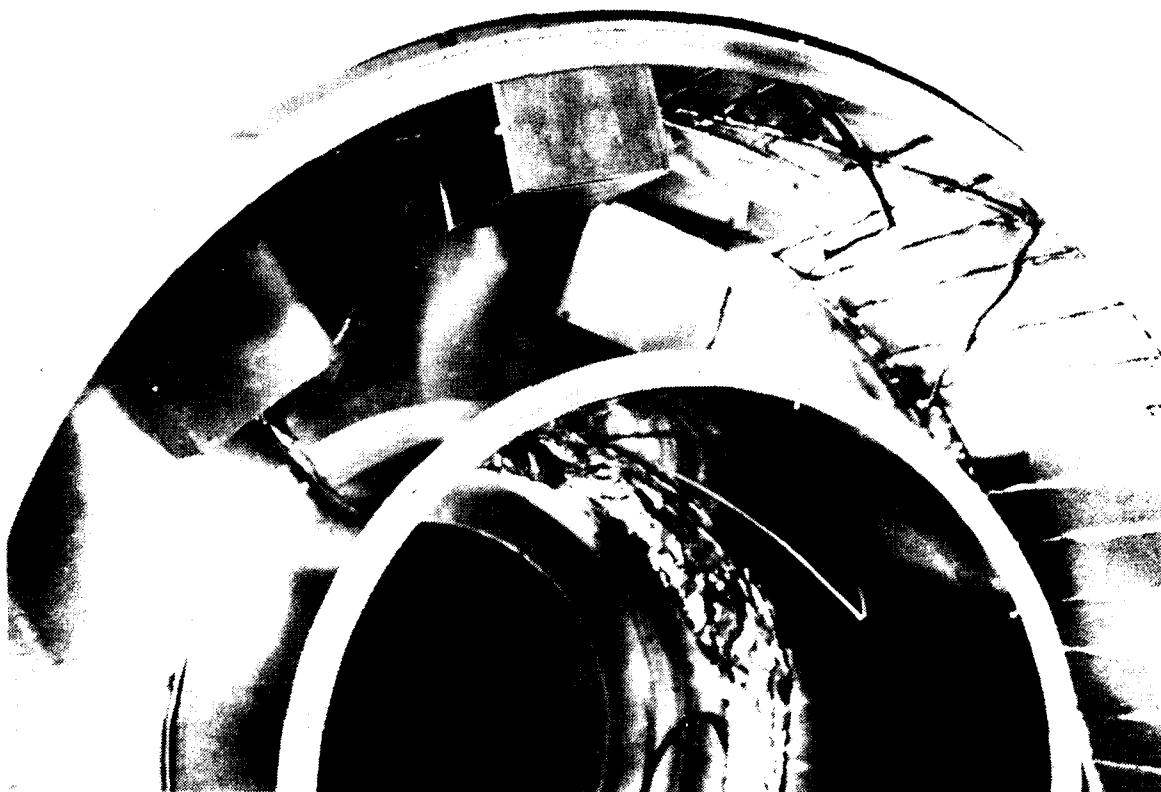
(a). Below Deck
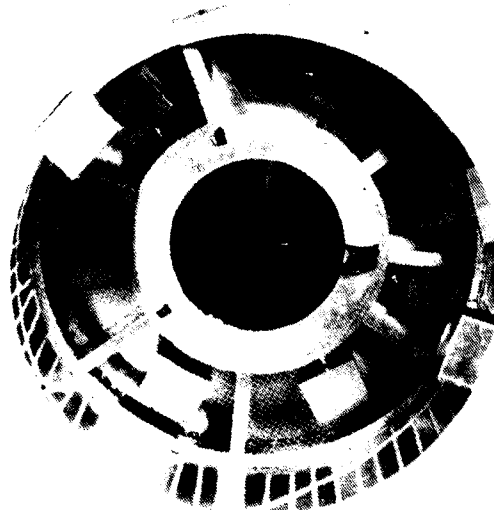
(b). Above Deck (note EMI screen)

Figure 17. Box layout in the SCATSAT

Samples of 3 conductor and 7 conductor shielded cable of the type used in the P78-2 satellite were used in a few locations. The shields were terminated in the same manner as the coaxial cables. One wire of each of these cables was terminated to the boxes with a 1000 ohm resistor at each end.

The two cables to the solar arrays are shielded twisted pairs. Shields are handled in the normal manner. One wire interconnecting the negative leads (drain wires) terminates directly to box 3B. The other lead of each terminates to the box through a 10 ohm resistor to simulate the load.

One unusual cable termination is that at the reference band. A coaxial cable has its shield connected to the metal inside the honeycomb near the 1.9 cm hole. The center wire connects a 10 megohm resistor passing through the hole and connecting to the reference band. The center wire is unterminated at the other end of the cable.

Table 3 lists the types of the 61 cables and their interconnection points.

Table 3. SCATSAT Cable Layout

Cable No.	Type	From Box	To Box	Cable No.	Type	From Box	To Box
1	A	1	2	31	A	4	3B
2	A	1	4	32	A	4	4B
3	A	1	5	33	A	4	5B
4	A	1	6	34	A	4	6B
5	A	1	7	35	A	5	3B
6	A	1	3B	36	A	5	4B
7	A	1	4B	37	A	5	5B
8	A	1	5B	38	A	5	6B
9	B	1	Ant	39	D	5	4/5 Aft
10	A	2	4	40	A	6	3B
11	A	2	6	41	A	6	4B
12	A	2	6	42	A	6	5B
13	A	2	3B	43	A	6	6B
14	A	2	4B	44	A	6	ML12-3
15	A	2	5B	45	A	6	ML12-3
16	A	2	6B	46	A	6	ML12-4
17	A	3	6	47	A	6	ML12-4
18	A	3	4B	48	A	6	ML12-6
19	A	3	5B	49	A	6	ML12-6
20	A	3	6B	50	A	1	3B
21	C	3	1 Forward	51	D	7	4B
22	A	3	SC1-1	52	A	7	5B
23	A	3	SC1-1	53	A	7	6B
24	A	3	SC1-2	54	A	7	6B
25	A	3	SC1-2	55	D	3B	6B
26	C	3	7 Boom	56	A	3B	AIM
27	A	4	5	57	E	3B	SAT
28	A	4	6	58	E	3B	SAB
29	A	4	6	59	D	4B	5 FWD
30	A	4	7	60	A	5B	1 FWD
31	A	4	3B	61	A	SC1-2	Ref Band
32	A	4	4B				

A. 50 ohm cable (RG174)
B. 50 ohm cable (RG58)
C. 3 conductor shielded cable from P78-2
D. 7 conductor shielded cable from P78-2
E. twisted shielded pair

62

All but one of the cables terminates in one of the 11 boxes above or below the main deck at one or both ends. The cables are formed in a loop inside the central tube, which is open to the surroundings. Cables pass through holes in the tube, radially to each of the boxes. The main cable loop is covered on all sides with aluminum foil secured to the tube wall with conductive metal tape, effectively shielding the bundle. The smaller groups of cables (maximum 10) passing into the metal boxes had their shields bared, tied together for mutual contact, and the bundles wrapped with metal tape which then connected to the outsides of the boxes. All shields then make contact to each other and to the box where they terminate.

The interconnection of the solar panel arrays attempted to simulate important details of the P78-2. Copper tape was laid on the solar array sustrates in the same pattern as the P78-2 solar cable, complete with negative interconnections and drain wires. The drain wires were covered with metal tape in the lower half, and insulating tape in the upper half. Direct interconnections substituted for diode isolation on the positive terminals. Interconnection of array banks was done with twisted pair cable, unshielded on the top, shielded on the lower set. Both upper and lower banks were connected to box 3B, as already noted, with twisted shielded pair cable.

Shielded cable extending outside the satellite body was overwrapped with aluminized Mylar foil, terminating at the metal box or antenna farthest from the body and at the body in the case of the 7 boom. The outer wrap over the omni antenna cable terminates at the foil shield over the main cable bundle in the central tube.

4.3.4 Experiment Penetrations

Experiment penetrations into each of the three major compartments, lower Faraday cage, upper Faraday cage (between decks), and the unshielded upper bay, were also simulated. The experiments simulated were respectively SC1-1, SC1-2 and ML12.

SC1-1 and SC1-2 look through the upper and lower solar arrays. The experiments were simulated with a pair of 8 inch square by 2 inch deep metal boxes. Holes were cut in the solar array substrates and copper tape was used to cover the exposed honeycomb to (1) make contact with the aluminum facesheet and (2) provide a contact surface for finger stock. Finger stock was placed on all four sides of the two experiment boxes and they were pressed into the holes so that the finger stock was well compressed. The general layout is shown in Figure 18. Note that no attempt was made to simulate the experiment samples in their attachment to cables. For electron spraying tests this will be done.

63

FINGER STOCK

ALUMINUM FACE SHEET

COPPER TAPE   EXPERIMENT

RT-17144
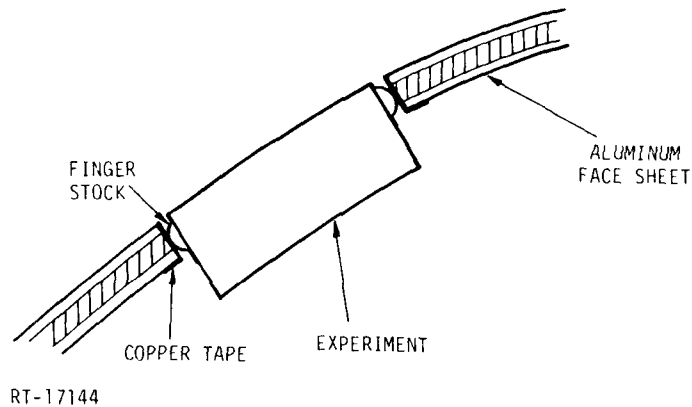
Figure 18. SC1-1 and SC1-2 experiment simulations

The ML12-3,-4 and -6 experiments look out through the belly band in Bay 6. The boxes are not mounted on the belly band but on a plate behind the belly band. An EMI seal is provided by means of finger stock which grounds the mounting plate to the adjacent rib and the belly band. The general arrangement is shown in Figure 19. Again, the experiments were simulated as metal boxes with no attempt made to simulate the material samples or other detail.

BELLY BAND

FINGERSTOCK

ML12-3

ML12-6

ML12-4

MOUNTING PLATE

FINGERSTOCK

RIB

RT-17145
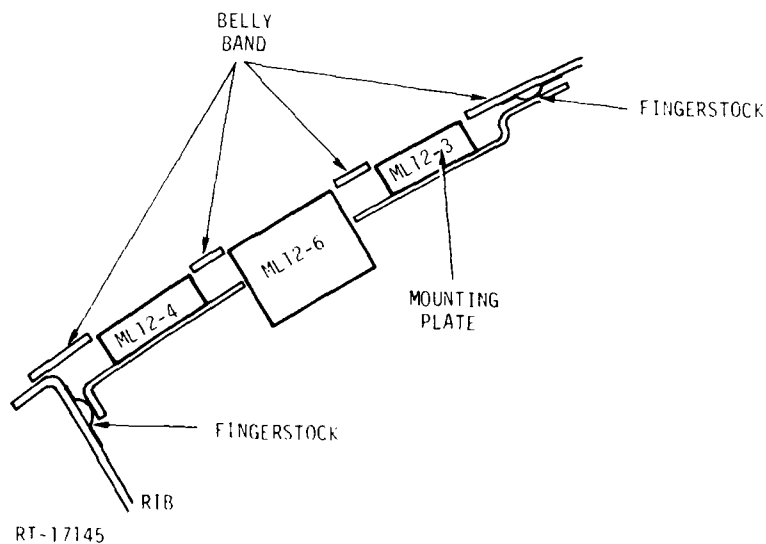
Figure 19. ML12 experiment simulations

In the experiment simulation the cabling in each experiment has not been included partly because of our perception that little energy would couple through them.

64

4.3.5 Solar Arrays

The solar arrays are potentially a major penetration into spacecraft and this penetration is monitored on the P78-2. A reasonably accurate solar array simulation is therefore desirable. The solar cells are simulated by strips of copper tape laid on the fiberglass outer facesheet of the substrate in a pattern duplicating the P78-2 layout. The pickup wires and entry points are also accurately simulated including the negative wire routing under the "cell" strings. These wires on the top array are left unshielded while the bottom array wires are covered with copper tape for shielding. A twisted pair interconnects the strings on the top array then becomes a twisted shielded pair for entry into the Faraday cage and ultimate termination of the "CU" (box 3B). The lower array uses all twisted shielded pair for interconnecting the strings and terminating the array at the "PCU." In the "PCU" each negative lead is grounded while the positive leads are loaded with a 10 ohm resistor to simulate the load on the array. The array "cells' and backplane wiring can be seen in Figures 14 and 15. For electron spraying experiments dielectric simulations of cover glasses will be included.

4.3.6 Reference Band

The reference band was simulated by a band of aluminum one inch wide and supported on dielectric spacers a half inch away from the surface of the lower array substrate. It was connected to the SC1-2 experiment by a shielded cable terminated as shown in Figure 20. The shield was grounded to the SC1-2 chassis at the other end.
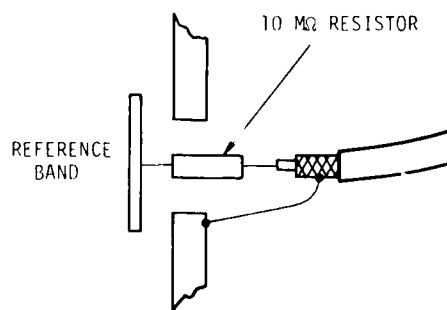
RT-17146

Figure 20. Reference band detail

4.3.7 Features Not Simulated

The SCATSAT is intended to be a reasonably accurate simulation of the P78-2 spacecraft but it is never-the-less only a simulation. There may be features which are

important to the EM response of the P78-2 which were left out or are only poorly simulated. Development of the model involved elements which were left out deliberately because we judge them to be unimportant. It is possible that one of these should have been included but were not through simple oversight or poor perception.

The SCATSAT is intended to simulate:

1. The basic structure of the P78-2
2. The Faraday cage or EMI enclosure (first level of shielding)
3. The cable harness shields (second level of shielding)
4. Some real wires
5. The solar arrays
6. Some experiment penetrations.

The largest and most easily recognized omission was details of the experiments, e.g., the various samples which are exposed to the environment and monitored for charge buildup, or sensors, antennas, particle experiment sources, as well as their connection to electronics and subsequently into the cable harness and other electronics. Because of the high degree of shielding in the P78-2 it is unlikely that arcs on the exterior will cause damage or even upset of the spacecraft electronics. But an arc in or to a material sample or other experiment can possibly enter the experiment package directly with the potential for upset or damage. This is an area which has not been adequately investigated to our knowledge.

4.3.8 Possible Satellite Modification

The SCATHA satellite is representative of many near future spacecraft designs such as DSCS-III in its use of a tightly sealed electromagnetic configuration to reduce EID/SGEMP effects. There are several older satellite types, many of which are currently flying, which have a much more open construction and which have shown EID effects. Examples are DSCS II and Intelsat IV. With a few simple modifications, the SCATSAT can be made to more closely simulate these spacecraft. A series of possible modifications and the satellites represented is shown in Table 4. These modifications will also yield characteristic responses to EID for specific defects in the SCATHA Faraday cage. These defects may occur during construction or once the spacecraft is in orbit. An example of an in orbit defect would be a deterioration of the external cable shielding.

Table 4. Possible SCATSAT Penetration Modifications

MODIFICATION	REPRESENTATIVE OF
Open top thermal Barrier and gap at outer edge	Intelsat IV, DSCS II
Replace SC1-1 and -2, ML12 with more open penetrations, earth sensors, thrusters, etc.	Many older satellites
Open bottom thermal barrier and introduce gap at outer edge	SKYNET
Isolate belly band	
Remove EMI Screen	Most older satellites
Float solar array substrates except for drain wire	Many satellites
Lower thermal barrier removed	DSCS II
Removing external cable shields	Many satellites

5. SCATSAT MODEL ELECTRICAL TESTS

This section discusses the electrical tests carried out on the SCATSAT model to simulate EID response. We have included the original test plan which was more elaborate than that carried out in practice. This has been done because the original plan indicated the rationale for all of the drive and measurement points chosen. The measurements carried out represented the perception of the testers as to which combinations were the most important. By presenting the entire test matrix, we solicit comments and suggestions for the reader as to whether other tests should be carried out.

5.1 ORIGINAL TEST PLAN

The original test plan was meant to be exhaustive in that it represented all of the measurements which we thought ought to be made. It described the proposed places where the SCATSAT model should be driven and why, the measurements to be made and how, and general test needs. The goals of this part of the experimental program were:

1. Analysis verification for simulating electron induced discharges with computer models

2. A partial determination of the simulation quality of laboratory electrical test techniques (validation of the technique adopted depends on the performance of electron spraying experiments)

3. Determination of coupling to and the electromagnetic tightness of the P78-2 spacecraft.

The test plan was based on two assumptions. First in the absence of detailed charging prediction of data for the P78-2, that any dielectric material on the outside may accumulate a sufficient surface charge to break down, therefore, making all external dielectric materials candidates. Second, that some high energy electrons (natural and artificial trapped) may be energetic enough to penetrate the top thermal barrier and subsequently be stopped in the layer of nonconductive paint on the equipment shelf or in cables or electronic boxes. We therefore identified some internal drive points as well as the external ones.

68

5.1.1 Drive Points

External: Dielectric surfaces on the spacecraft exterior are predominantly on the side (solar array cover plates and second surface mirrors) and bottom (nonconductive paint). The fourteen candidate drive points selected are listed in Table 5 and shown in Figure 21. The rationale for this selection is based on the previously discussed possibility of an arc at any arbitrary location on the outside, as well as the reasons given in Table 5.

Table 5. Candidate External Drive Locations for SCATSAT

DRIVE LOCATION	RATIONALE
A	Symmetrical excitation of structure, use arc and emission drive to quantify relative importance.
B	Asymmetrical excitation of structure on top.
C & D	Excites SC1-2 and -1 respectively, good candidate for electron spraying experiments, asymmetric side excitation.
E	Excites reference band near entry point.
F	Excites ML 12 and lower solar array 140° from entry.
G & H	Excites SC1-2 and solar arrays at entry point.
I	Excites SC1-1 and solar arrays 180° from entry point.
J	Excites reference ban 180° from entry.
K & L	Excites solar arrays 90° from entry point and ML-12 and SC1-2 from midway between.
M	Aft drive opposite "B", excites REM, possibly reference band.
N	Asymmetric side excitation on solar array rather than body.

Note that there is no dielectric material at point A on the top of the spacecraft. This point was included to provide a symmetric drive point for which arc discharge vs electron emission as a structural response driver could be tested. Point B was a legitimate candidate since it is in approximately the location of the SC1-3 experiment, which contains four six by six inch dielectric samples. Such samples are the only dielectric surfaces on the top of the satellite.

Internal: Dielectric surfaces on the spacecraft interior are either nonconductive paint or thermal wraps. Four tentative drive locations were selected. They are listed in Table 6 and shown in Figure 22. This was a very preliminary selection and more drive points were expected to be added when details of the cable routing were known. While no points were specified, it would also be reasonable to directly drive cables to simulate

69
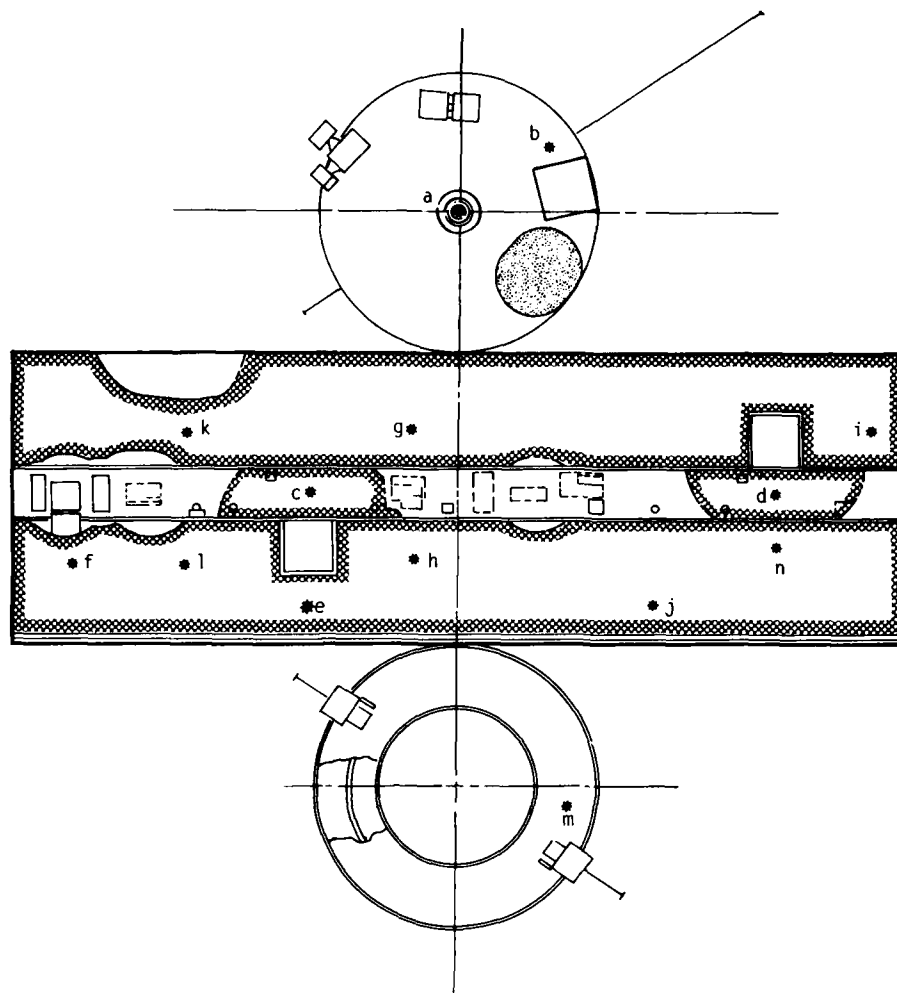
RT-16136

Figure 21. Candidate external drive point locations

discharges occuring in their dielectric. However such excitations should be supported by model calculations to determine whether for high energy electrons entering the cable harness can create discharges.

Table 6. Candidate Internal Drive Locations for SCATSAT

DRIVE LOCATION	RATIONALE
O	Discharge in paint on shelf, predominantly E field cable excitation.
P	Discharge in paint on inside (exposed) surface of central tube, predominantly E field cable excitation.
Q	Discharge in manhole closeout, excites upper cavity.
R	Discharge in tank thermal cover, excites lower cavity of Faraday cage.

70
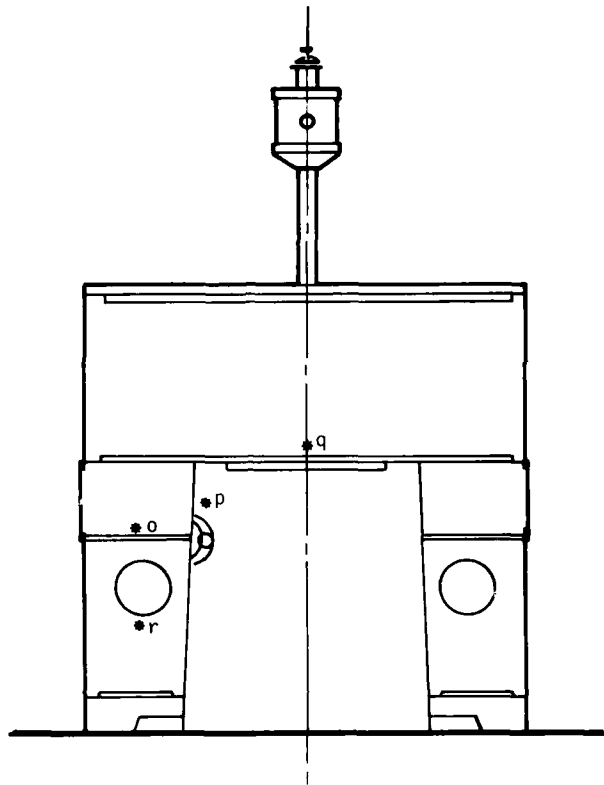
RT-16137

Figure 22. Candidate internal drive point locations

5.1.2 Drive Techniques

Drive techniques which have been considered include arc discharge (AD), capacitive direct injection drive (CDI), direct current injection (CI) into penetrations, and, for completeness, electron spraying in a vacuum tank (ES).

The relative drive effectiveness of arc discharge and capacitive direct injection drive were partially tested in the can experiment described in Section 3.4. It was shown, as expected, that capacitive direct injection is the more effective drive, i.e., produces larger structural responses, so that electrical tests used only the later. The next phase of experiments will be a direct comparison between two techniques (possibly supplemented by direct injection of penetrations) driving the same test points or those excited in the MMC EMC/EMI tests.

Capacitive direct injection to simulate the emission of charge which accompanies the arc is a well developed technique (Refs 26,27). We have used a pulser mounted on a capacitively coupled return plate which then attaches via a wire to the point of

simulated discharge on the test object. Some of the discharge characteristics and effects are known, but much remains unknown (See Section 3.2). For example, the pulse time history for arcs is reasonably defined from available literature. Based on this survey, we planned to use two pulses, one of ~10 ns rise and fall time and a second with a 10 ns rise and a somewhat longer fall time of ~100 ns. Similarly, the effective electron emission current due to the discharge is estimated from literature to be of the order of 1 A/cm^2 with the maximum total area contributing to emission being ~10^4 cm^2.

Conveniently available drive levels for simulating electron emission are of the order of amps at most using an ANVIL Model 160 pulser. Measurement sensitivities of the HDL fiber optic links employed in the tests are of the order to 0.1 to 1 mV. Between the outside of the SCATSAT and the inside, there are at least two shield levels and in some cases three. Thus, there could not be more than about 60 dB of attenuation between drive and any internal current measurement in order to have acceptable signal to noise ratio. This was a problem because the SCATSAT, just as the P78-2 satellite it represents, is relatively tightly shielded against penetrations by outside EM disturbances. The possibility of going to a noninsulated high level drive to overcome this problem was considered. A scheme we examined was utilizing one or more trays of the IRT Marx generator. This technique would result in about a factor of 300-1000 increase in drive level.

Simulation testing for the electron emission drive mode is simpler than that for arc discharges due to the repeatability and reproducibility of the drive source. This allowed making a complete set of measurements with several drive pulses instead of having to make all the measurements at once, thus reducing the sensor and data links requirements as well as minimizing disturbance of the SCATSAT EM configuration by the instrumentation. If the arc discharge itself should be the important driver, the test program would be significantly more complex provided that a punchthrough simulation (as opposed to the use of a simple spark gap were required). The dielectric through which the arc is driven would probably have to be replaced after each shot and all of the pertinent measurements would have to be made on each shot. This substantiates importance of the "can" experiment directed at quantifying the relative importance of these drivers so that a decision could be made regarding the need for arc discharge testing.

72

5.1.3 Measurements

Measurements taken included surface currents (in the form of $\dot{B}$), "Solar array" cable currents, currents on cable and wire shields, and wire load voltages. On each test the drive function was characterized by measuring the arc current or emission current time histories.

An electron induced discharge will excite structural responses in the form of surface currents and electromagnetic fields which may then couple into the SCATSAT via solar array wiring, leakage around thermal closeouts and experiments, shield penetration, etc. Because leakage signals may be small and will be related to the magnitude of the external response, the latter is an important measurement for external excitations. Seven candidate measurement locations were selected for characterizing the external response. These are shown in Figure 23. Note that points 2 through 7 are on the same line around the spacecraft on which drive points A,B,C,D, and N are located. The $\dot{B}$ sensors are oriented to measure currents flowing along this line, as excited by each of the five drive points. Probe 1 is 90° from this line and is oriented to measure circumferential current, which should be negligible for drive at A, larger for drive at B, and greatest for drives at C, D, and N. Probe 3 was deleted for drive at point D.

The second major response characteristic of the satellite is the current induced on the overall cable shields used on all cables outside the Faraday cage. As a minimum, it was felt that measurements should include the shield current on the main bundle running around the inside of the central tube, a branch up the antenna tripod to a top mounted experiment, one or more branches into equipment compartments, and one of the boom mounted experiment cables.

Current on individual wire shields and wire load voltages were measured inside the equipment compartments. The exact points were determined from an examination of the P78-2 harness drawings and the final SCATSAT harness design. Load voltages were measured directly across load resistances while individual shield currents were measured with current probes. One wire signal which we felt was important to monitor was the reference band voltage.

The "solar array" was expected to be a major penetration on SCATSAT and the common and differential mode currents on the solar array cable were to be measured where it goes into the simulated PCU.

73

5.1.4 Test Sequence

A complete test sequence using the drive points, drive techniques, and measurements just discussed was formulated. In acuality, the measurements taken during this phase of the program formed a modest subset of the complete program. This sequence is shown in Tables 7 through 9 along with the purpose of each test. Basically, the first four tests were designed to completely characterize the external and internal responses of the SCATSAT to different external drive locations while tests 5 through 14 were chosen to drive one or more specific penetrations. The solar array penetration was characterized for all of the drive locations, many of which are on the solar array. Tests 15 through 18 (tentatively) characterized the internal response to internal drives.
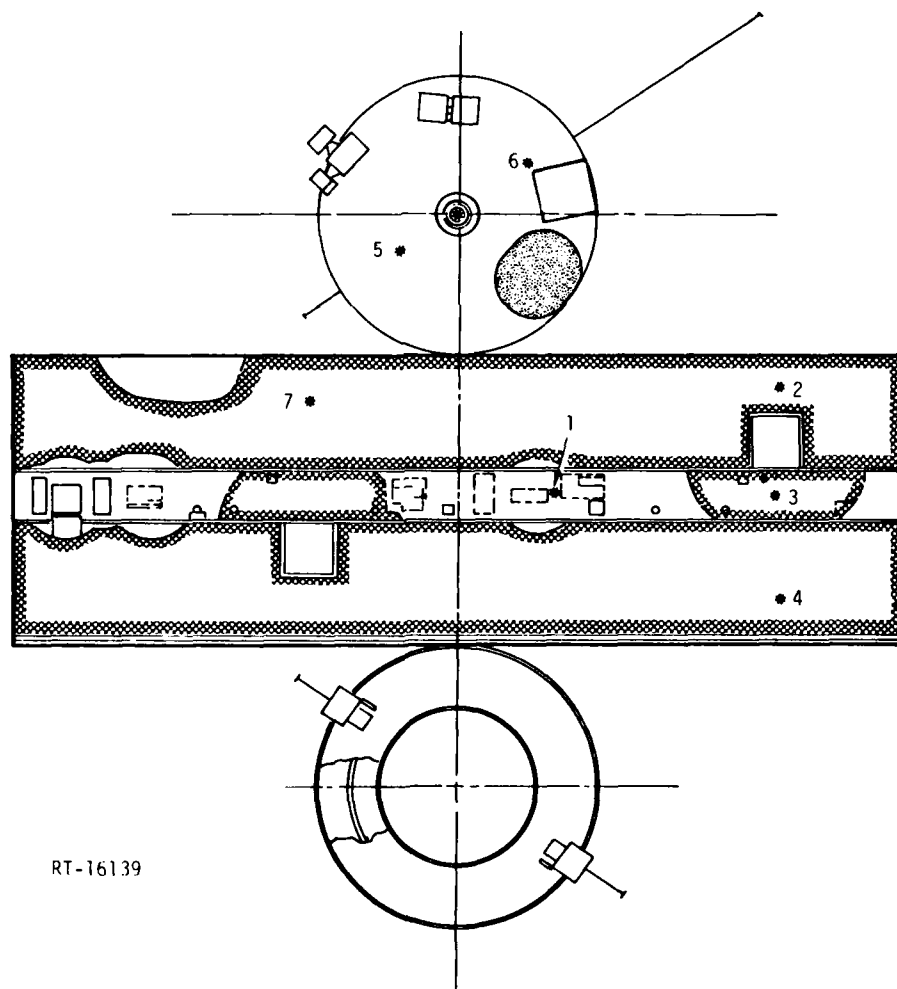
RT-16139

Figure 23. External surface current measurement points

74

Table 7. Complete Test Sequence, External Measurements

TEST #	EXTERNAL DRIVE POINT	EXTERNAL MEASUREMENTS	DRIVE TECHNIQUES	PURPOSE OF TEST
1	A	$6,2,3,4, (\dot{J}_{A\&R})^1$ Discharge Current, Voltage	AD ES (Top on) CD	Test relative effectiveness of AD $\underline{vs}$ CD as I_R driver, validate against ES, validate AD drive technique.
2	D	$2,6,5,7,4 \ (\dot{J}_{A\&R})$ $1 \quad (\dot{J}_\phi)$ Discharge current	CD ES (Side-on) AD	Same as 1, for side-on excitation of the body.
3	N	$2,6,5,7,4 \ (\dot{J}_{A\&R})$ $1 \quad (\dot{J}_\phi)$	AD CD ES	Test structural excitation from arc on solar array.
4	B'	$7,5,6,2,3,4 \ (\dot{J}_{A\&R})$ $1 \quad (\dot{J}_\phi)$ Discharge current	CD AD ES	Same as 1 for asymmetric top excitation.

[1] A denotes along axis of symmetry of SCATSAT Body

R is radial direction, perpendicular to axis of symmetry and to outer surface.

ϕ is the Azimuthal direction, perpendicular to axis of symmetry and radial direction.

5.1.5 General Test Requirements

The test object must be placed in an area relatively free of metallic boundaries which reflect electromagnetic energy back onto the test object. Past electrical test programs on similar size objects have shown that reflections can be acceptably minimized by placing the object four to five feet off the ground, a similar distance from any overhead metal containing structures, and with a clear area of a few object diameters provided around it also. A screen room is required for data taking because significant electromagnetic interference is radiated from the object. We have used a "highbay" area in IRT's facility at 7070 Convoy Court. This is the same one which has been used in past satellite model electrical tests.

5.2 CAPACITIVE DIRECT INJECTION

5.2.1 Short Pulse

A Pulsar Associates, Inc. Anvil-L system was used to provide short pulse current injection into the satellite while maintaining the dielectric isolation of the SCATSAT from its surroundings. The drive set up is shown in Figure 24. The pulser itself is

75

battery-powered, normally producing a 160 volt, 1 ns nominal risetime pulse into a 50 ohm load, using a transistor operating in the avalanche mode as the switch. A control module coupled to the pulser by a fiber optic cable enables the e perimenter to fire single or repetitive pulses.

Table 8. Complete Test Sequence, Internal Measurements

TEST #	EXTERNAL DRIVE POINT	INTERNAL MEASUREMENTS	DRIVE TECHNIQUE	PURPOSE OF TEST
1	A	Reference band voltage, solar array cable current, external cable shield current, cable load voltage, ML 12 cable current, SC1-1 & 2 cable current, internal fields(?)	All. Baseline response experiment, for top excitation.	AD vs CD as solar array driver. Coupling of external response to solar array. Coupling of external response to external cable. Coupling of external response to system loads. Coupling of external response to experiment penetration. Coupling of external response to interior.
2	D	Reference band voltage, solar array cable current, external cable shield current, cable load voltage, ML 12 cable current, SC1-1 & 2 cable current, internal fields (?).	All. Baseline response experiment, for side excitation.	AD vs CD as solar array driver. Coupling of external response to solar array. Coupling of external response to external cable. Coupling of external response to system loads. Coupling of external response to experiment penetration. Coupling of external response to interior.
3	N	Solar array (SA) cable current, reference band voltage.	AD, CD	Coupling of arc on lower SA (opposite SA entry point) to SA cables. D to N comparison..
5	C	Reference band voltage, solar array cable current, SC1-2 cable current.	AD, CD	Same as D but adjacent to SA entry point.
6	H	Solar array cable current, reference band voltage.	TBD	Same as N but adjacent to SA entry point, lower array.
7	G	Solar array cable current, reference band voltage.	TBD	Same as N but adjacent to SA entry point, upper array.
8	F	Solar array cable current, reference band voltage.	TBD	Coupling to SA from arc 140° from entry point, coupling to ML 12 from closest arc.
9	I	Solar array cable current	TBD	Same as N for upper array arc
10	K	Solar array cable current, reference band voltage.	TBD	Coupling of upper SA arc 90° from entry point to solar array cable.
11	L	Solar array cable current, reference band voltage.	TBD	Same as K for arc on lower solar array.
12	M	Solar array cable current, propellant line current, reference band voltage	TBD	Test coupling to solar array, reference band, REM from arc on bottom.
13	E'	Reference band voltage, solar array cable current.	TBD	Test coupling to reference band from arc near entry point.
14	J'	Reference band voltage, solar array cable current.	TBD	Test coupling to reference band from arc opposite entry point.

76

Table 9. Test Sequence, Internal Drive and Measurements

TEST #	INTERNAL DRIVE POINT	INTERNAL MEASUREMENTS	DRIVE TECHNIQUE	PURPOSE OF TEST
15	0	Wire shield current, wire load voltage, internal fields.	CD	Coupling of internal arcs to wire shields and loads inside the EMI enclosure.
16	P	Cable shield current, wire load voltage.	AD, CD	Coupling of arcs inside central tube to main cable bundle.
17	Q	Cable shield current, wire load voltage.	AD, CD	Coupling of arc in manhole close out to cable shields in upper cavity.
18	R	Cable shield current, wire load voltage, propellant line current.	CD	Coupling of arc on tank insulation to wire shields and loads inside the lower EMI enclosure.
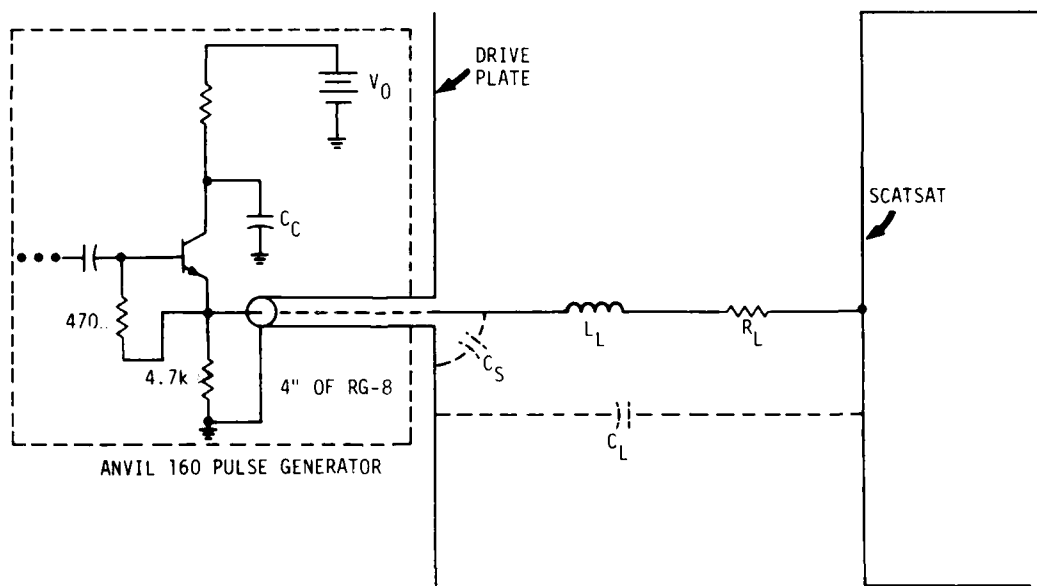
RT-16858

Figure 24. Test setup for current injection testing

The Anvil pulser is configured to permit injecting current into a given point on the satellite, with charge return accomplished by a large area disc serving as a capacitor.

Experiments using varying RLC values led to the adoption of a 69 cm diameter plate connected to the pulser cable shield, spaced 30 cm from the surface around the

77

drive point. A wire containing a 100 ohm resistor connects the pulser center conductor to the desired location - it is incorporated to damp out ringing in the drive pulse. A typical pulse shape is shown in Figure 25. It has a t_r (10-90) of about 3 ns and a FWHM of about 10 ns.
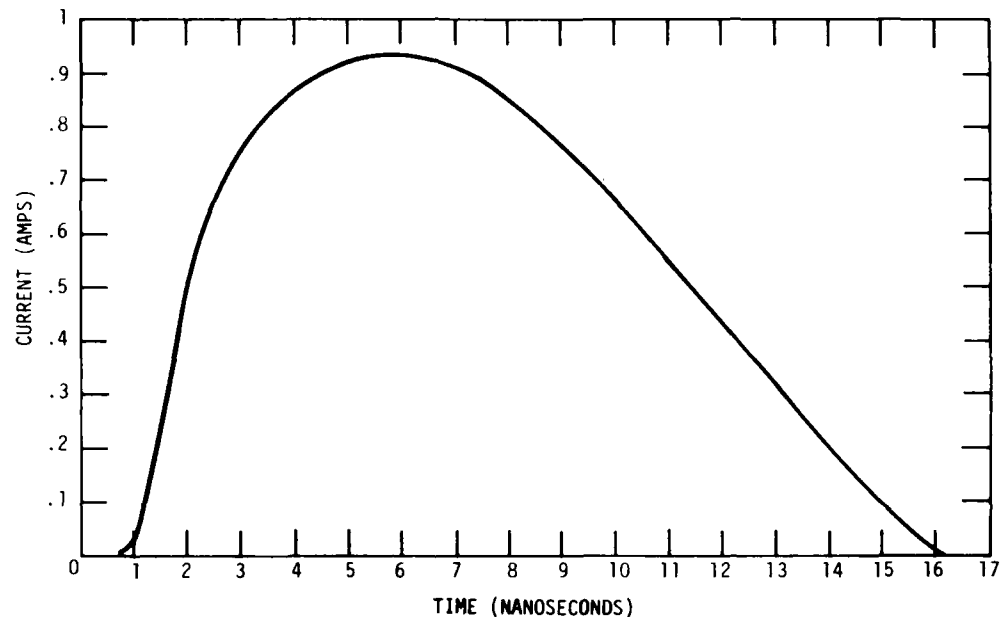
RT-16864

Figure 25. Fast pulse from Anvil L Pulser

5.2.2 Long Pulse

A relatively slow pulse was desired for the purpose of exciting lower frequency modes [and because longer pulses return currents consequent to discharge have been reported (Ref 23)]. Various schemes of integrating the pulse before injection to the satellite body resulted in impedance mismatches and oscillations. An analysis of the driver characteristics using the circuit analysis code TRAC indicated that a large increase in driver plate capacitance would permit a comparable increase in series inductance, widening the pulse without instability. The results of this analysis are covered in Appendix B. Figure 26 compares the "long" and "short" pulse current waveforms derived from typical photographs. The rise time is comparable but the fall time is about 30 ns.

78
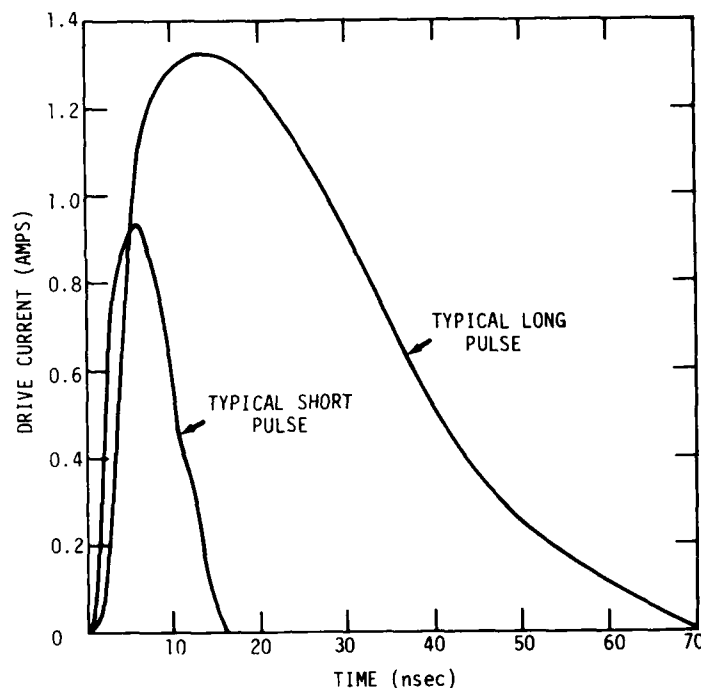
RT-17151

Figure 26. Typical short and long pulse current waveforms

The driver plate used for the slow pulse was somewhat larger in diameter than the satellite, 125 cm. Preliminary tests were limited to placement at point A only. The driver plate could be effectively wrapped around the cylindrical wall of the satellite to increase capacitance.

5.3 SENSORS AND DATA LINKS

There were two basic kinds of sensors used for the SCATSAT testing, surface current derivative ($\dot{B}$) sensors and various current (I) sensors.

5.3.1 Surface Currents

A $\dot{B}$ sensor built by EG&G, the model CMLX3B, is a modification of the CMLX3A design which permits surface mounting without structural damage. It retains the reduced electron emission when exposed to X-rays, capability of operation in vacuum, frequency response and sensitivity of the earlier design (Ref 32). It was decided to use the 3B to minimize the required penetrations (for signal cables in the case of the 3B's) for sensor mounting.

79

Output leads are a pair of coaxial cables projecting from the sensor ground plane at right angles to the loop axis. Taking measurements at two orientations without shifting surface position requires extensive relocation of connecting cables, rather than simply turning the sensor 90° and re-fasting in place.

Six locations were actually examined during this series of tests. all were on a plane through the satellite axis passing through the centers of boxes SC1-1 and SC1-2. Sensors were oriented to measure rate of change of current flow along the plane ($\dot{J}_z$) for all six sensors. Positions 2 and 3 were also run with sensors at right angles ($\dot{J}_\phi$), for the drive point at top center (position A).

5.3.2 Wire and Cable Currents

Three types of current sensors were used to determine current waveforms through cables or shields. For measurements involving a single small wire, a Tektronix CT2 probe provided adequate bandwidth, sensitivity, and peak current capability. A Singer type 95080-1 permitted current measurement of small groups of wires or wires with shields. It has a 4 ohm sensitivity, versus 1 ohm for the other current sensors used, and is useful to about 200 MHz.

A Singer type 91550-2 probe is physically large, has a bandwidth to about 100 MHz, and can be clamped over a relatively large cable bundle. One was used to measure current in the main cable bundle circling the central tube. The foil shield over the cable was altered to include the sensor.

5.3.3 Fiber-Optic Data Link

HDL-designed fiber optic data links (Ref 28) were provided for this test series. Briefly, a self-contained battery powered transmitter is placed in or on the satellite body, with only dielectric materials connecting it to the outside world. One or two coaxial cables connect to a nearby sensor. Transmitter functions include remote control, signal conditioning and conversion to modulated light which is transmitted over glass fiber, and a method of remotely calibrating the system gain.

A separate fiber optic link is used for the control functions of turning the transmitter on and off, inserting a calibration signal, and switching in desired nv rements of attenuation. Since the transmitter requires relatively large amounts of ..wer, which is supplied by a battery of limited energy, the remote controls are ....t.

At the opposite ends of the fiber optic cables inside a screen room are receivers, control modules, power supplies, and oscilloscopes. Controls for the drive pulser are also in the screen room to allow operation from one location.

Normal operation consists of placing sensors in desired locations on the satellite and connecting them to their respective transmitters. Current sensors that were used have single output cables, requiring removal of baluns and moving the input connection to the exterior of the cases. Signals are reversed for single-ended operation, but not differential. After an operational check of the links, the satellite is closed and the drive pulser is put into its first desired position. The sensors were left intact while the drive points were moved during a test session, due to the relative ease of repositioning the pulse driver assembly.

Experience with the links has proved the necessity of a stringent operating procedure including calibration checks. Built-in calibration signals may be monitored to check system gain. It was advisable to recheck this gain each time a transmitter was used for a measurement or series of photos at different sweep speeds. Also, records were kept concerning receiver photo-diode current levels, which were continually changing between data shots. The greatest variation in system gain resulted from ambient temperature changes; room temperatures in the 80's sometimes produced marginal operating conditions as system gain was drastically reduced.

Each transmitter exhibits its own pattern of linearity or range of input voltage which can be considered to be within its linear range. It is possible to tune each transmitter to operate within its "linear" region, but normal ambient temperature changes, battery conditions, and laser on time prevent maintaining the system at its optimum settings. In practice, attempts were made to drive the transmitters at lower levels than that of the calibration signals and to determine gains from parameters at each measurement photo.

The electrically isolated data links, while troublesome to use, are necessary. If cables were used to carry the sensor signals to the recording instrument, these cables would ring at a frequency determined by their length and end loading. Since the satellite end of the cables are basically being driven directly, the ringing currents would be very large and would mask the smaller, desired responses. They would also change the distribution of currents on the test object from that which occurs in the normal free space environment of the satellite.

5.4 GENERAL EXPERIMENTAL SETUP

The general experiments setup is shown in Figure 27. The principal concern in carrying out these measurements is the need to simulate reasonably well the free space electromagnetic environment that exists around the real satellite. That is, there should be no significant reflections from nearby metal back toward the model since these could cause a change in its response. Past experimental programs have addressed this problem for right circular cylinders, similar to the main body of SCATSAT model, and have shown that metal a couple of object diameters or greater away from the object is not a problem.

As the figure shows, the floor and ceiling were about one object dimension from the SCATSAT model. An additional concern was whether reflection of energy radiated from booms back toward the SCATSAT model. Both of these problems were therefore addressed by an analytical and experimental study to model such reflectances for simple geometries. This work is described in Appendix C.

On the basis of this study, it appears that a separation distance of ~1-2 meters from any boundary is adequate to avoid ground interference problems during electrical tests of the SCATSAT. In fact, no evidence of reflections were seen in the test data.

5.5 QUALITATIVE DISCUSSION OF DATA

The test program resulted in data taken for the matrix of test conditions and satellite configurations shown in Table 10. Measurement points are listed in Table 11. Not all possible combinations of test conditions and satellite configurations described in Section 5.1 were tested nor were a full set of measurements taken for each combination. There drive points are a subset of those identified in Table 5. The short and long pulse widths refer to the 10 ns and 30 ns FWHM capacitative direct injection drive pulses shown in Figure 26. Several experimental configurations for the SCATSAT were examined. These included response with no booms attached (0), SC1-4 alone (1), and all booms attached (5). In addition, measurements were taken with the top antenna penetration open and closed and with the antenna on and off. The r, z and o directions are those commonly used for cylindrical coordinates.

Typical data photographs are shown in Figure 28. These were selected from the data for drive point A which is by far the most complete set of data taken.

METAL DOOR

CHAIN LINK CAGE

3.8 m

2.9 m   SCATSAT
             D=1.1 m   2.7 m

MISCELLANEOUS (MOSTLY NONCONDUCTIVE)

3.5 m

TOP VIEW

SCREEN
ROOM

ALUMINIZED VAPOR BARRIER

1.8 m   1.5 m

SHORT PULSE DRIVER

SCATSAT

1.3 m

CONCRETE FLOOR

RT-17137   SIDE VIEW
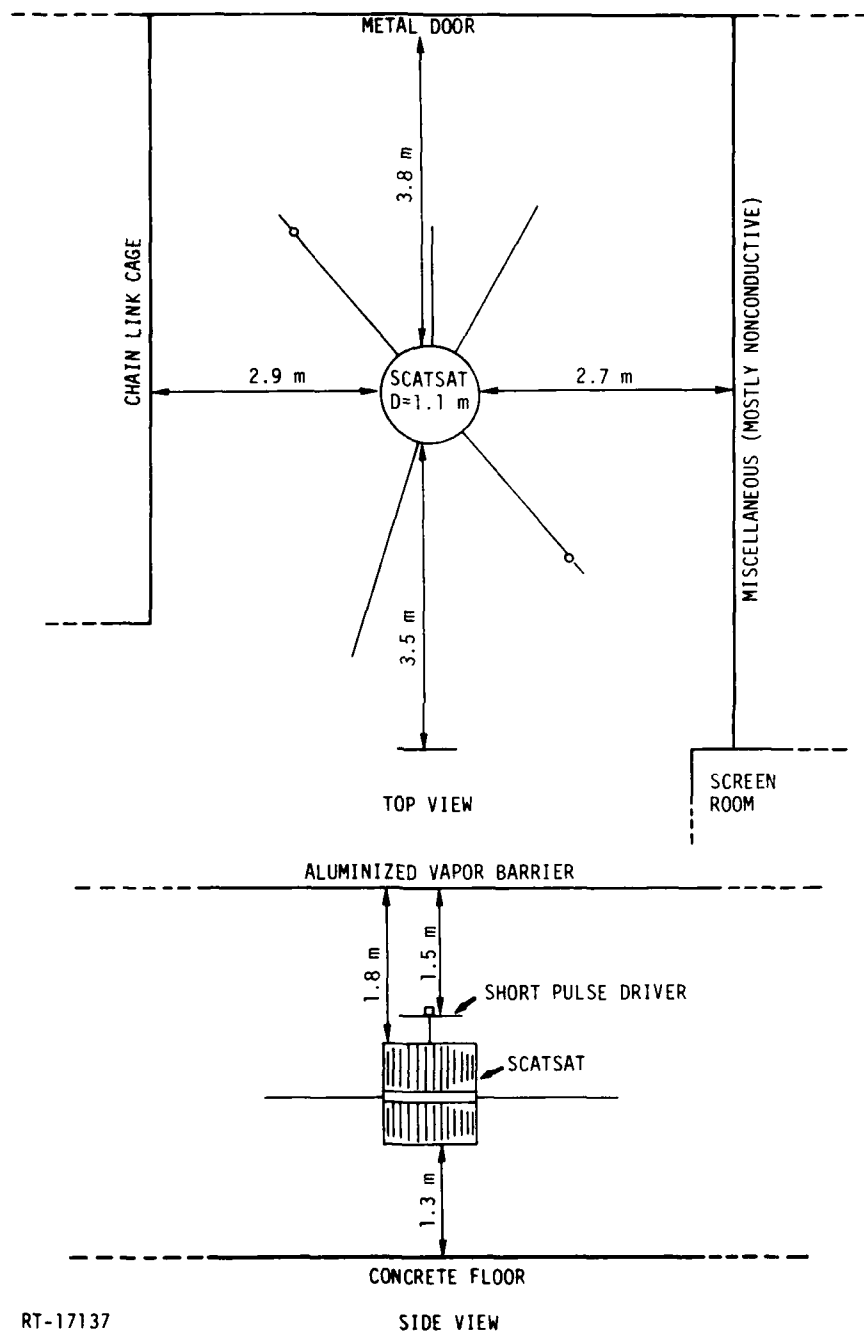
Figure 27. Experimental setup

83

Table 10. SCATSAT Model Test Conditions and Satellite Configurations

Drive	Pulsewidth	Booms	Ant. Penetrations
A	Long, short	5,1,0	Open, sealed
B	Short	5	Open
C	Short	5,0	Open
G	Short	5	Open

Table 11. SCATSAT Model Measurement Locations

Surface Current Measurements		
Location	Orientation[1]	Boom/Cable Currents (I)
2	z, ϕ	SC 1-4 boom
3	z, ϕ	SC 1-4 internal shield
4	z	3B cable
5	r	Lower solar array
6	r	Main loop bundle
7	z	Long antenna

[1]Orientation of $\dot{B}$ sensor to measure the tabulated current component.

The photographs were examined to determine the peak amplitudes of positive and negative excursions and the dominant frequencies in each record. These are summarized in Tables 12 and 13 for external surface current derivatives, expressed as $\dot{B}_s$ and boom or cable currents. The peak amplitudes have been normalized to a constant 1000 mA drive current. To convert from $\dot{B}$ (Teslas/sec) to $\dot{J}$(amp/m) the relationship $\dot{J}(amp/m) = \dot{B}(tesla/sec)/4\pi 10^{-7}$ may be used. Note that the magnetic field component producing a given current is orthogonal to that component, i.e. B_ϕ is produced by J_z.

The dominant frequencies in the time histories were determined by visual examination of the photographs. The quantitative frequency data were inferred from the average time between adjacent peaks, where at least two cycles, and usually more, were distinguishable. In most cases, more than one frequency was present. However, frequencies were similarly inferred from the time between peaks if at least two cycles of the lower frequency were visible. Qualitative data were also noted where higher or lower frequencies were clearly present but not sufficiently clear so that the frequency could be determined.

84
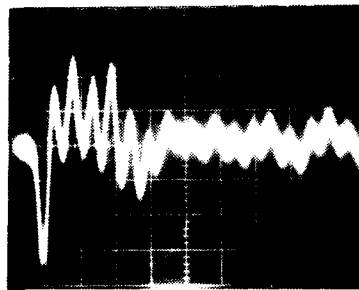
A. Short Pulse,
   Sensor 2 B_z
   Vert: 28 Teslas/sec/div
   Hor: 10 ns/div
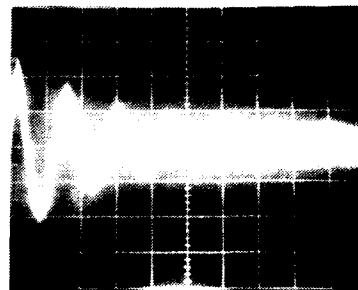
B. Long Pulse,
   3B Cable Current
   Vert: 24 mA/div
   Hor: 1000 ns/div
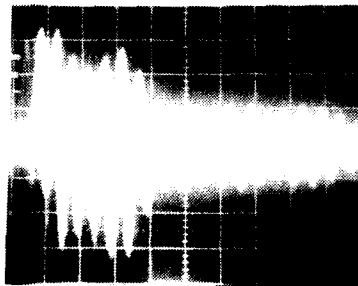
C. Long Pulse,
   SCI-4 Boom Current
   Vert: 5.8 mA/div
   Hor: 50 ns/div
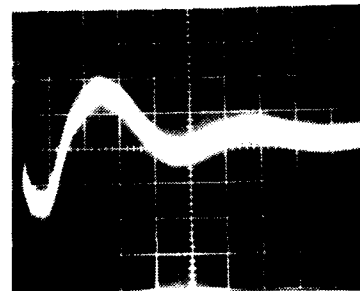
D. Long Pulse,
   Lower Solar Array Current
   Vert: 2 mA/div
   Hor: 200 ns/div

Figure 28. Typical data photos, Drive A

5.5.1 Drive Point A, Symmetric Top Excitation

Drive point A symmetrically excites the exterior of the SCATSAT. A continuous right circular cylinder driven in this way would be expected to have axial $\dot{B}_\phi$ responses greatest near the drive point and falling off continuously toward the far end of the can such as was observed in the "CAN" experiment. The measured SCATSAT responses do not follow this trend. Sensor 3, which is midway down the side of the SCATSAT on the belly bound, has a larger response for both the long and short pulse drive and for the five boom and no boom configurations than sensor 2 near the top of the SCATSAT which is closer to the drive point. The fact that this pattern showed up consistently in four separate tests suggests that it is very real and not a measurement anomally. Nor does

85

Table 12. External $\dot{B}$ Sensor Data*

Drive	Pulse Width	Location	Orientation	5	No. of Booms 1	0	Antenna Penetration	Omni Antenna
A	Long	2	z[b]	-19,+9[1] 285/140[2]	x[3]	-17,+11 265/140	Open	On
		2	ø	-8.7,+8.7 110	x	-35,+27 190	Open	On
		3	z	+30,-11 130/330	x	-31,+144 170	Open	On
		3	ø	+12,-31 36/HF[4]	x	x	Open	On
	Short	2	z	-80/+50 185/LF[5]	x	-76,+61 180	Open	Off
		2	ø	+35,-19 190/33	x	-54,+27 73/HF	Open	Off
		3	z	+130,-120 170	x	-205,340 61	Open	Off
		3	ø	+54,-160 35/200	x	+21,-24 176	Open	Off
		4	z	+30,-36 76/37	x	x	Open	Off
		7	z	-150,+220 230/74	x	x	Open	Off
B	Short	2	z	-290,+270 150	x	x	Open	Off
		4	z	+35,-49 210/ 50	x	x	Open	Off
		7	z	-110,+130 170/38/60	x	x	Open	Off
C	Short	2	z	-45,+120 37/200	x	-39,+91 200	Open	On
		4	z	-24,+21 38/250	x	-28,+21 200	Open	On
		4	z	x	x	+22,-34 190	Open	Off
		5	r	-110,+130 110/37	x	x	Open	Off
		6	r	+24/-38 220/110	x	x	Open	Off
		7	z	+720,-330 90	x	+680,-310 90	Open	On
		7	z	x	x	+790,-110 ?	Open	Off
G	Short	2	z	-82,+73 170/~50	x	x	Open	Off
		4	z	-15,+26 39/200	x	x	Open	Off
		5	r	-73,+140 120/33	x	x	Open	Off
		6	r	+23,-20 180	x	x	Open	Off
		7	z	+65,-100 180/79	x	x	Open	Off

*Normalized to 2A drive peak amplitude

[1] Peak amplitudes (teslas/sec). To convert to rate of change of surface current (amps/m), multiply by $10^7/4\pi$.

[2] Dominant frequencies (MHz)

[3] Not measured

[4] HF denotes a high frequency component whose strength is too weak to be determined

[5] LF denotes a low frequency component whose strength is too weak to be determined.

[b] $\dot{B}$ sensor measuring tabulated current component; i.e. $\dot{B}_ø$ is associated with J_z or J_r depending on position of sensor on can.

it appear to be associated with resonant currents on the booms since it occurs for both no boom and five boom configurations. Presently we believe the most likely explanation for the higher response of the belly band $\dot{B}_\phi$ sensor is as follows. The top of the SCATSAT is connected to the conductive inner face sheet of the upper solar array substrate which then connects directly to the belly band and the lower array substrate. The simulated solar arrays on which sensor 2 is mounted is a complex configuration of metal strips adjacent to but electrically isolated from the substrate. These may present a higher impedance path for current than the substrate so that current flows preferentially on the substrate and then appears on the belly band as a larger current than on the simulated arrays.

Table 13. Boom and Cable Currents[*]

Drive	Pulse Width	Sensor	No. of Booms 5	No. of Booms 1	No. of Booms 0	Antenna Penetration	Antenna
A	Long	SC1-4 Boom	+13,-13[1] 40[2]	+18,-6 40		Open	On
		3B Cable	+30,-33 0.68	x[3]	+36,-30 0.68	Open	On
		Lower SA	-3,+2.5 1.2	x	-5,+4.2 1.1	Open	On
	Short	SC1-4 Boom	+58,-62 44	+86,-86 53	x	Open	On
		Boom Shield	+3.2,-2.0	x	x	Sealed	Off
		3B Cable	+300,-210 69	x	+320,-160 69	Open	
		3B Cable	+8,-6 0.76	x	x	Sealed	Off
		Lower SA	+1.2,-2.5 74/~1	x	+2.1,-5.1 71/~1	Open	
		Lower SA	+4.7,-4.7 1.6	x	x	Sealed	Off
		Long Ant Current	+58,-62 13	x	x	Open	
C	Short	Loop Cable	x	x	+3.2,-3.2 43/170	Open	On
		Long Ant Current	x	x	+55,-55 12	Open	On

[*] Normalized to 1 A peak drive current

[1] Peak amplitude in mA

[2] Dominant frequencies in MHz

[3] Not measured

87

While the pattern of relative response amplitudes is independent of pulsewidth, the average value of external response is lower for the long pulse than for the short as shown in Table 14. For the configuration with five booms, the difference in $\dot{B}_\phi$ is consistently a factor of 4 to 5. With no booms the scatter in the ratio is greater. Since the signals being compared are derivatives, the question naturally arises as to how much of the difference is due to differing frquency content of the driver and responses. The answer appears to be very little for this case. Table 12 shows that the response frequencies are not greatly different and that some even higher frequencies appeared in the long pulse response than occurred in the short pulse response.

Table 14. Ratio of Short Pulse to Long Pulse Responses, Drive A

Sensor	5 Booms	No Booms
2 z $(\dot{B})^1$	4.2	4.5
2 φ $(\dot{B})$	4.0	1.5
3 z $(\dot{B})$	4.3	7.7
3 φ $(\dot{B})$	5.2	—-
SC1-4 Boom (I)	4.5	—-
3B Cable (I)	9.1	8.9
Lower SA (I)	0.83	1.0

^{1}Refer to current component monitored by the $\dot{B}$ sensor.

The nonderivative responses (i.e. I or B) exhibited short to long pulse response ratios ranging from about one (no difference) to roughly an order of magnitude. The solar array response was little affected while the coupling to the internal cable at location 3B was greatly affected. The latter is due to the fact that significant penetration occurs via the top antenna cable. The length of this cable exposed is different by a factor of 6 depending on whether the long pulse is used, which exposes ~5 cm of cable, or the short pulse which exposes ~30 cm. When this penetration was sealed, the coupling to the internal cables dropped by a factor of 38 (31.6 dB). The SC1-4 boom current differed by the same factor of 4-5 exhibited by the $\dot{B}_\phi$ sensors.

Experiments were conducted with and without booms to determine their effect. This information is important for designing possible electron spraying experiments where it will probably be impossible to deploy booms in an available vacuum tank. The z orientation of sensor 2 (2z) was unaffected as shown by comparison of tabulated results. But sensors 2φ, 3z, and 3φ were all significantly affected. Likewise, the

current response of the SC1-4 boom was affected by the presence or absence of its two neighbors. None of the few internal responses measured were affected by the absence or presence of the booms but it is clear that those closely coupled to a boom would be. The 300 foot antenna was simulated on the SCATSAT by a large plate to increase capacitance back to the body. The antenna simulation rang at a frequency of 13 MHz for the symmetric excitation. None of the external $\dot{B}$ sensors were measured with the antenna simulation in place so it is not known how this frequency couples to the body.

The dominant frequencies appearing in the time histories were determined by visual examination of the data. The identified frequencies exhibit considerable scatter and a convenient way of identifying groupings is to display them as shown in Figure 29. For example, the short pulse excitation clearly shows groupings around 35 MHz, 75 MHz, and 185 MHz for external $\dot{B}$ sensors. A single occurrance is at 60 MHz. The booms have a resonance around 50 MHz and the two cable measurements show both low frequency components (around MHz) and high frequency components (around 70-80 MHz). For the long pulse excitation the boom and cable current frequencies are similar to short pulse responses but the $\dot{B}$ sensors show much more scatter and generally higher frequencies. In fact there can hardly be said to be any groupings in these data.

RT-17156
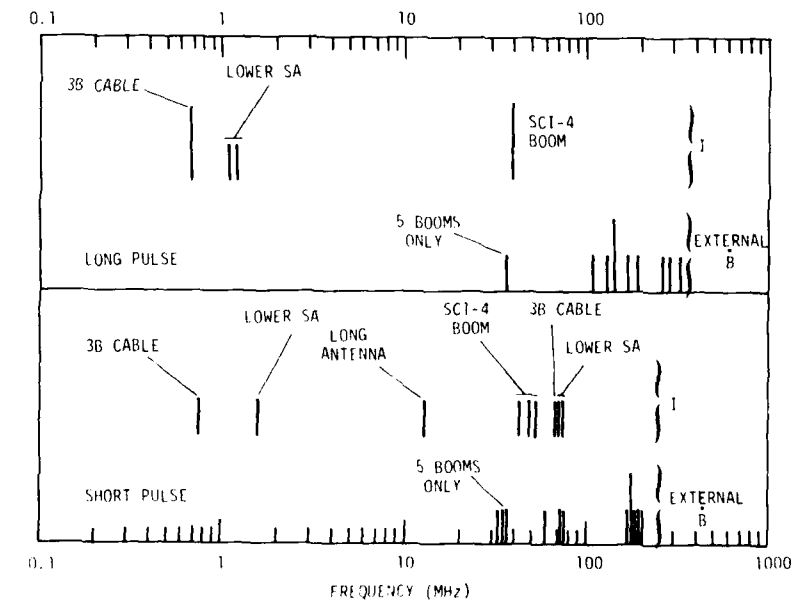
Figure 29. Frequency distribution of responses for drive point A. The short lines are for responses observed once while the longer lines are for those appearing twice

89

The two drive pulses have been Fourier transformed to compare their frequency content over the region of interest. The transforms are plotted in Figure 30. This shows that for the drive pulses normalized to 1000 mA peak current, the short pulse has generally higher amplitude than the long pulse in this region. Thus, the response differences are not explained by the drive current.
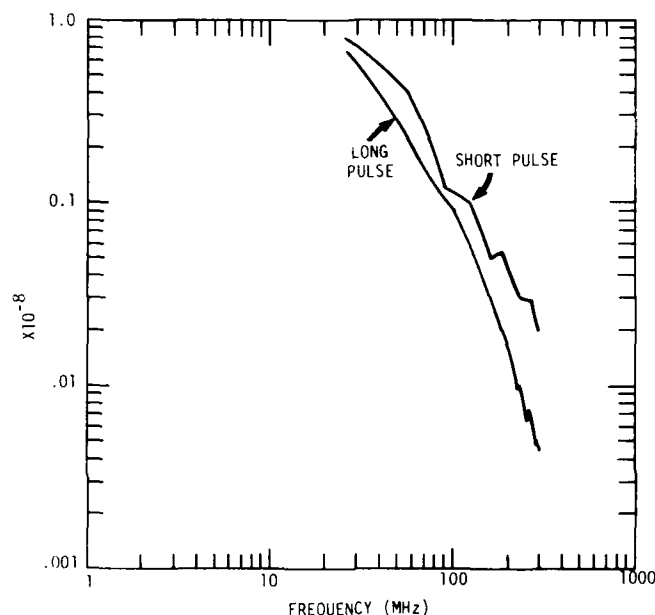
RT-17163

Figure 30. Fourier transform of typical drive pulses

The frequency groupings which show up in the short pulse excitation of point A are summarized in Table 15 along with the probable sources of each. Only the very low frequency which appears on the 3B cable when the antenna penetration is closed seems unexplainable. The 1.1 to 1.6 MHz on the lower solar array cable is expected since the large capacitance of the "array" to the substrate and the large inductance of the cable form a low frequence LC circuit. The 0.7 MHz frequency is related to the upper solar array. The 35 MHz which appears in external sensors probably is from the nearby SC2-1 boom since it disappears for the no boom configuration. The 40 to 53 MHz group results from the resonance of SC1-4 boom since it is measured only on this boom or associated cables. The 60 to 75 MHz group probably results from the axial mode of the satellite as a right circular cylinder. It appears predominantly in the $\dot{B}_z$ records. The 70 MHz which appears on the 3B cable with the antenna penetration open is believed to

90

be associated with the length of the antenna cable. This cable is about a meter long and since it is grounded at one end and open at the other it will ring at a quarter wavelength. The four meter wavelength corresponds to 75 MHz. The 71 to 74 MHz group which appears on the lower solar array cable along with the low frequency fundamental could have two sources: coupling from the antenna cable or leakage from the outside directly via the solar array. Comparison of photographs with and without the antenna penetration are not conclusive but it appears that the more likely source is the antenna. The 170 to 200 MHz group is possibly the circumferential mode of the can, though it appears in both axial and circumferential sensors.

Table 15. Resonant Frequencies and Sources

Frequency	Source (Predicted Frequency)
0.7 MHz	Upper Solar Array LC Circuit
1.1-1.6 MHz	Solar array LC circuit
35 MHz	SC2-1 Boom resonance (35)
40-53 MHz	SC1-4 Boom resonance (58)
60-75 MHz	Axial mode of can (66)
70 MHz (3B cable)	Length of antenna cable (~75)
71-74 MHz	External leakage or antenna cable
170-200 MHz	Circumferential mode of can (170)

As mentioned, the $\dot{B}$ data for the long excitation pulse are not so neatly grouped. After much puzzling over this, we believe that the following may explain what happened. The capacitive return plate had to be placed much closer to the top of the satellite than for the short pulse (5 cm instead of 30 cm), and extended to the full diameter of the satellite to obtain enough capacitance to significantly lengthen the pulse. (Note that even then it was not as long as originally desired). This configuration creates a transmission line like configuration which appears open circuited at the outer edge and loaded at the center. The "length" of this line is 55 cm and the quarter wavelength resonance corresponds to ~140 MHz. The fringing fields at the open outer edge of this line would excite the sides of the object and the sensors there, which could explain the broad group centered at 140 MHz. The higher frequency group around 300 MHz could be a second harmonic of this resonance. This modified drive configuration may also be less effective in exciting the object which would account for the lowered responses observed for long pulse excitation.

We believe the following conclusions can reasonably be drawn from the above discussion.

1. The SCATSAT does not exhibit $\dot{B}_\phi$ response distribution like that of a continuous right circular cylinder of the same size, probably because of the physical construction of the model and the SCATHA satellite.

2. The long pulse drive produces generally smaller responses, by factors of a few, than the short pulse. This may be all or partly explained by the difference in drive configuration which may be less effective in exciting the SCATSAT body.

3. Considerable excitation of the internal SCATSAT cables resulted from the top antenna cable penetration. Coupling decreased by ~30 dB at one measurement point when this penetration was sealed.

4. External $\dot{B}$ responses are affected by the absence or presence of the booms. The effect on internal responses is inconclusive except that responses associated with the boom cables are certainly affected.

5. Response frequencies resulting from the short pulse excitation are reasonably well grouped and with one exception can be explained by analysis of the model geometry. The exception is the very low frequency which appears on the internal cable at location 3B when the antenna penetration is sealed.

6. Response frequencies of external $\dot{B}$ sensors resulting from the long pulse excitation seem less well related to the object resonances and may be dominated by the geometry of the drive configuration instead.

5.5.2 Drive Point C, Side Excitation

This excitation drives the SCATSAT on the "back side" of the belly band, away from the 2-3-4 row of sensors and the SC1-4 boom. A continuous right circular cylinder excited in this manner would be expected to have relative $\dot{B}_\phi$ and $\dot{J}_z$ responses of $7 > 5 > 6 > 2 \simeq 4$. The measured responses are $7 > 5 \simeq 2 > 6 > 4$. Only sensor 2 seems to have a response which is out of line with expectations. Its response is comparable to that of a sensor much nearer the drive. This particular sensor was measured twice, for a full set of booms and for no booms, and exhibited comparable response amplitudes for both measurements. Therefore its response is not considered to be a measurement anomaly.

A possible explanation for this response is as follows. Unlike the axial drive which strongly excited the structure, the side drive strongly excites the solar array. Note that sensor 7 has a very large response. Of course, all the segments of the array are

92

interconnected so it may be that sensor 2 is driven by currents coupling directly through the array rather than by body currents. The credibility of this explanation is, unfortunately, jeopardized by the small response of sensor 4. It should be similarly excited and have a larger response if the hypothesis is correct. Thus, there is presently no adequate explanation for the large response of sensor 2.

Frequencies in the $\dot{B}_\phi$ responses show three distinct groups, around 37 MHz, 100 MHz, and 220 MHz (q.v. Figure 31). The first group probably results from boom resonances as before. The third group possibly results from the circumferential mode of the satellite which is more strongly excited by the asymmetric drive. However, the frequencies don't agree well with the axial drive. The asymmetric drive is also expected to excite a "circumferential" mode along the line of sensors. This mode has the same frequency as the axial mode, ~70 MHz. Again the 100 MHz group may correspond to this mode but the frequency appears to be shifted upward.

RT-17152
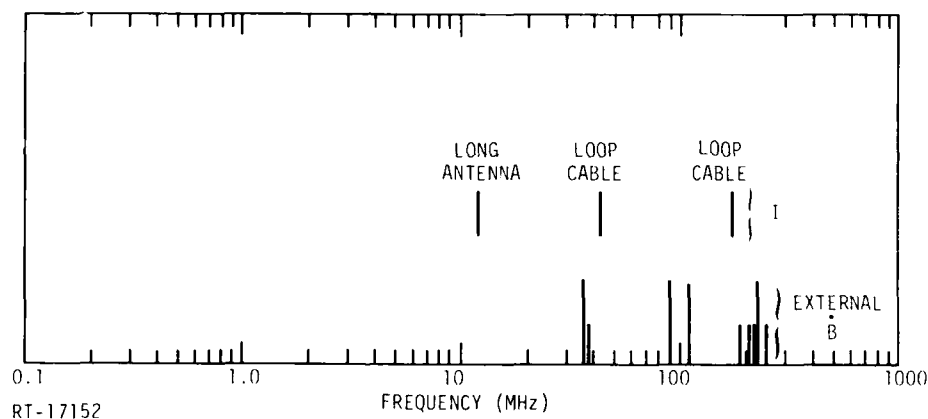
Figure 31. Frequency distribution of responses for drive point C. The short
lines refer to those frequencies appearing once, while the
longer line represents a double occurrence.

The only internal measurement was on the main bundle which loops around the inside of the central thrust cylinder. The measurement is a bulk cable current under the shield which covers this cable and was made adjacent to rib number 6. Two frequencies show clearly: 170 MHz and 43 MHz. The 170 MHz corresponds to the length of the loop. The 43 MHz probably represents leakage via a boom cable which then excites the loop.

No boom currents were measured for this drive, but the current on the simulated long antenna was measured. It rang at the same frequency and with the same amplitude as for the symmetrical excitation case.

93
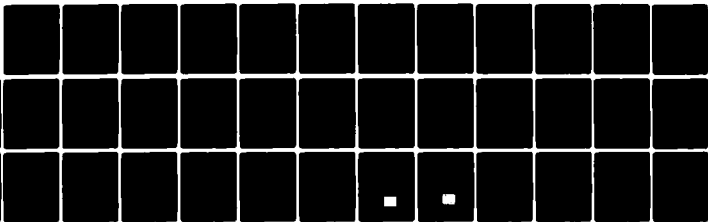
The following conclusions appear reasonable for these data.

1. The SCATSAT asymmetric drive case also does not exhibit external $\dot{B}_\phi$ responses like those of a right circular cylinder. There is presently not a good explanation for this.

2. Response frequencies associated with the body resonances appear to be shifted upward in frequency from those expected and previously measured.

5.5.3 Drive Points B and G

Drive B excited the top of the SCATSAT as did drive A, but the drive point is off center so that the excitation is asymmetrical. Only data from three external $\dot{B}_\phi$ sensors were recorded, 2, 4, and 7. Approximately the same frequencies show up in these responses as before (q.v. Figure 32). The response amplitude of sensor 2 increased sharply while sensor 7 decreased as a result of driving the object much nearer sensor 2 rather than midway between them as before. The response of sensor 4 increased slightly. Thus the responses for drive $\dot{B}$ are as expected relative to drive A.

RT-17153

FREQUENCY (MHz)

EXTERNAL $\dot{B}$
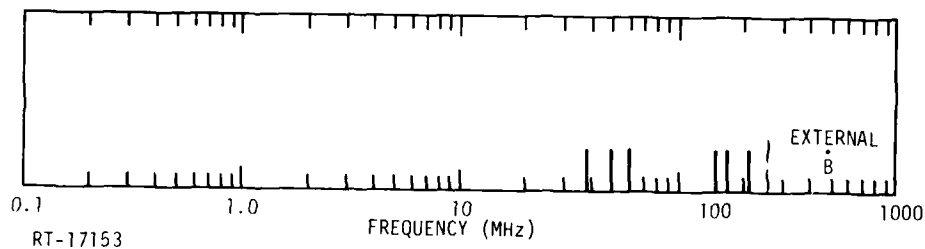
Figure 32. Frequency distribution of responses for drive point B

Drive G excited the side of the SCATSAT on the solar array just above the belly band. This drive point is not only asymmetric but is different from the others in that the satellite is excited elsewhere than on the structure. The responses of five $\dot{B}_\phi$ sensors, sensors 2 and 4 through 7, were measured. The frequencies are shown in Figure 33. Approximately the same frequencies appear as in the other excitations.

RT-17154

FREQUENCY (MHz)

EXTERNAL $\dot{B}$
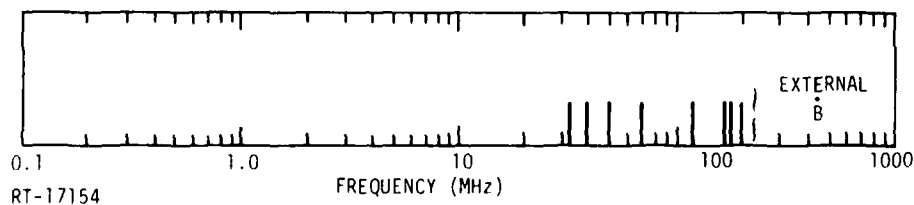
Figure 33. Frequency distribution of responses for drive point G

94

The relative peak amplitudes for the five sensors are 5>7>2>4~6. The greatly reduced response of sensor 7 is the most notable result of this drive. Because of its ~45° orientation to this drive (as compared to drive C), its response would be expected to be lower by ~30%. In fact, it is down by a factor of 8. All of the other sensors show little change in response amplitude with the exception of 2 which is down by ~35%. The large decrease in the response of sensor 7 with respect to drive C is surprising since the sensor is in nearly the same position with respect to the driver.

5.6 SUMMARY

The electrical test program on the SCATSAT measured a fairly complete set of data for one drive scheme, symmetric excitation on the top, and smaller sets for three other drivers, all asymmetric excitations. The following general conclusions about the SCATSAT are drawn from the data analysis.

1. The external surface current responses of SCATSAT, and the SCATHA satellite, are not like those of a continuous conductive right circular cylinder as might have been expected and as such a satellite structure is frequently modeled.

2. The booms significantly affect the external surface current responses.

3. The top antenna cable is a major penetration into the internal cables for drive points near the antenna. Measurements at one point decreased by a factor of ~40 when this penetration was sealed. However, there is no area near this antenna which is likely to discharge so that it may not be problematic.

4. Frequencies appearing in the various responses can generally be accounted for by resonances associated with particular structural features of the spacecraft.

5. For 1,000 mA of emitted current the internal or penetrating current levels with the top antenna penetrations sealed are approximately:

   a. On a boom wire shield: 3 mA
   b. On the 3B cable bundle: 8 mA
   c. On the loop cable: 3 mA
   d. On the solar array cable: 5 mA

95

e.   On the long dipole antenna: 50 mA.

The 3B and loop cable currents would be increased if the top antenna penetration were opened.

Another conclusion has been drawn concerning the drive schemes used. We wanted to use both short pulse, ~10 ns up and down triangular, and a long pulse, ~10 ns up and >100 ns down. The actual short pulse used had a rise time (10 to 90%) of more like 3 ns with an 8-10 ns FWHM. This was obtained from the Anvil pulser with no need for shaping. To obtain a longer pulse, it was necessary to increase the capacitance between the return plate and the object. Experiment and analysis showed that it was necessary to bring the return plate down very near the object and increase its size to the diameter of the object in order to bring the pulse width up to even 30 ns FWHM and 70 ns base width. This was still not as wide as desired but was accepted as a compromise. The experimental results suggest that this configuration resulted in resonances which were associated with the driver configuration rather than the object and that it is a less efficient excitation of the test object. More work is needed in this area if it is required to simulate long discharge pulses.

6. ANALYSIS

6.1 INTRODUCTION

One of the major tasks which was to be carried out in this program was the modification of an SGEMP coupling code to predict the response of spacecraft structures to its dielectric discharges. In their traditional application such codes take an input photoelectron current generated by x-rays or other high energy photon sources and then follow the resultant currents and fields by an appopriate application of numerical solutions to Maxwell's equations, including the Lorentz force. In the EID problem, the driver is the discharge described as a current source. Thus, the first task faced was to specify the arc discharge. This work was described in Section 3.7. Given a characterization of the discharge, we modified an SGEMP code to predict the EID induced response. How this was done is described in Section 6.2. One significant aspect of the problem is whether or not it is necessary to simulate thin (a few mils thick or less) dielectric over conducting substrates in adequately describing the replacement currents which flow consequent to a discharge. (Of course, one must have dielectrics present for electron induced charging to occur). The answer to this problem, which is essentially negative, is presented in Section 6.3. Since a prediction of the responses of the "CAN" to various discharge simulations is an adaptation of techniques described in this chapter, we have placed the details of the computer simulation analysis for this experiment in Section 6.4. The experimental setup, results, and method of scaling can be found in Section 3.4. Finally, the computer code predictions of the SCATSAT external body responses due to capacitative drive electrical tests and comparison to experiment are presented in Section 6.5.

6.2 MODELING OF DIELECTRIC DISCHARGES WITH SGEMP CODES

Early in this program, the question arose as to how to calculate the body currents due to dielectric discharges. It was recognized that the already-existing SGEMP codes should be useful tools for this purpose provided that the electromagnetic driving functions due to the discharge could be properly incorporated into the codes and

97

provided that other features of the discharge problem, such as thin dielectrics, did not cause serious difficulties. In this section, we describe the techniques that have been used to model the various driving functions for a discharge, such as the collapsing dipole when punchthrough discharge occurs, the outward emission of charge, and the capacitive drives.

6.2.1 Simulation of a Collapsing Dipole

At various times during this program, we have attempted to model the effect of a collapsing dipole sheet with the SABER code (Ref. 30). Under this program, the capability to simulate dielectrics in arbitrary regions of the problem was added to SABER. In this code, the finite-difference mesh regions are represented by capacitances and inductances in the three coordinate directions. Thus, a dielectric sheet would be represented by a sheet of parallel capacitors (with an appropriate dielectric constant), one end of which terminates on the conducting substrate while the other connects to the capacitors which represent free space. To create the charged dielectric sheet, charge would be transferred from some place in the simulated volume (for example, from the exterior boundaries that represent the electron plasma and infinity or from another point on the spacecraft) to the outer terminals of the capacitors which represent the dielectric sheet. This charge transfer is done in a time-dependent fashion and the code readjusts the charge in the system to provide the positive image charges at the substrate terminals of the dielectric capacitors and make the conductors equipotentials when equilibrium is attained. When this charge-up is completed, the potential due to the dipole layer will have been established.

Different methods were used to simulate the collapse of the dipole potential, depending on what effect we were trying to achieve. In one case, we wanted to simulate the uniform punchthrough of the trapped charge to the substrate. To achieve this, a shunt leakage path (lossy conductor) around each dielectric capacitor was turned on when the punchthrough was supposed to begin. The capability for using lossy conductors was also added to SABER during this program. The discharge rate could be controlled by adjusting the RC time constants of the lossy capacitors.

For simulating the can arc discharge experiment (Section 3.4), we wanted all of the charge from the outer surface of the dielectric to funnel into the substrate at one localized spot. To achieve this flow of charge parallel to the surface of the dielectric, the capacitors in the plane of the dielectric sheet at its outer boundary had to be shorted to provide a conducting path. The localized punchthrough from the outer

98

surface of the dielectric to the substrate could be accomplished by shorting the appropriate capacitors through the dielectric, as described above for the uniform punchthrough. However, the resulting pulse shape would be some function of L, R, and C of the dielectric-substrate system which is difficult to predict a priori. Therefore, if a specific discharge pulse shape is desired, as in the simulation of the arc discharge (Section 3.4), the simplest approach is not to create the localized short through the dielectric sheet but just to insert a localized current source with the desired pulse shape from the outer layer of the dielectric sheet to the substrate.

It should be pointed out that most of the above operations are non-standard for the SABER code, and for all other known SGEMP codes, because it involves changing the physical characteristics of the structure (for example, its electrical conductivity) midway through the calculation. To do this, one must insert temporary instructions into the code for each mesh region where a change is made. Also, care sometimes has to be exercised in how the changes are implemented. For example, once when the time constant of the shorted capacitors was made too short, it caused computational noise which completely overshadowed the normal response.

6.2.2 Simulation of Blowoff

The simulation of outward emission of electrons from the dielectric surface is particularly simple because practially all SGEMP codes have this capability as a standard feature. In this program, we have only simulated uniform emission from some area. If it is shown later that the emission emanates primarily from a localized spot, the simulated emission area can be restricted accordingly. In SABER and in most SGEMP codes, the emission pulse shape and the electron energy and emission angle distributions are arbitrary inputs. Particle dynamics in the self-consistent electromagnetic fields determine the subsequent trajectories of the emitted electrons.

Unfortunately, no known SGEMP code has the capability to simulate charged particles other than electrons. Therefore, they cannot simulate the emission of ions. If it is found that ion emission has a significant effect on the return currents, this capability would have to be added to the SGEMP codes. Such a code change would not be an excessive job because one could just add an emission and a particle-pushing subroutine for the ions similar to the one for electrons, and then add the ion electrical currents to the appropriate mesh regions.

6.2.3 Simulation of Capacitive Direct Drive

The simulation of the capacitive direct drive techniques with the SABER code is a completely standard operation. It is only necessary to simulate the conducting capacitor plate and a current source with a specified current pulse. In the SCATSAT electrical tests, the pulser hardwire leads from the assumed discharge point on SCATSAT to the capacitor plate, so the simulated current source is also from SCATSAT to the capacitor plate. It is also possible to drive the capacitor plate from ground and to have only capacitive coupling between the plate and the test object (Ref. 27). However, that is not the way the present tests and the corresponding calculations were made.

6.3 EFFECT OF THIN DIELECTRICS ON THE RESPONSE OF SPACECRAFT STRUCTURES SYSTEM TO DISCHARGING

The dielectrics that are most important from the standpoint of surface discharges in satellites are usually quite thin (on the order of a few mils or less) and they have conductive backings. The straightforward approach to simulating thin dielectrics in SGEMP codes would be to make the mesh zones equal to the thickness of the dielectric. However, the maximum permissible computational time step (Δt) in a three-dimensional SGEMP code is governed by the Courant condition that Δt must be less than $\Delta x/c\sqrt{3}$, where Δx is the minimum mesh width in the problem and c is the speed of light. For $\Delta x \cong 5$ mils $= 0.0127$ cm, Δt must be less than 2.5×10^{-13} sec. This is a prohititively small time step for typical SGEMP or discharge problems that can have characteristic times from tens to hundreds of nanoseconds. Therefore, a different approach is necessary when utilizing SGEMP codes to simulate dielectric discharge problems.

One fairly rigorous approach was proposed by Boyd (Ref 33). It consists of modifying the boundary conditions in the SGEMP code at the metallic surface that is covered with the dielectric. In his method, he obtains the first-order effect of the dielectric without having to use a mesh width equal to the dielectric thickness. Unfortunately this boundary condition is not in the SABER code and making the necessary modifications would have been a sizable undertaking because SABER is written in machine language with highly sophisticated word usage for efficient operation. Therefore, before deciding to expend a considerable amount of effort on incorporating Boyd's boundary conditions into SABER, we made an effort to estimate how important these boundary conditions might be in the simulation of body responses

to dielectric discharges. Each analysis which we tried, as discussed below, indicated that the effect of very thin dielectrics ($\approx$ a few mils) on conducting substrates would have only minor effect on the body responses to a dielectric discharge (less than a few percent). Therefore, for the present program, we felt that it was reasonable to just ignore thin dielectrics in the SABER simulation of dielectric discharges on SCATSAT. In other words, the conducting substrate was modeled but the thin dielectric was omitted. Of course, if the dielectric was the source of the discharge, the outward emission of charge, which is the main driver due to the discharge, was modeled in the region where the dielectric should have been but the emission was assumed to come directly from the conducting substrate rather than from the surface of the dielectric. The response of the charges in the substrate, and therefore in the rest of the spacecraft, should be almost identical with and without the dielectric due to the strong capacitive coupling across the thin dielectric. In other words, the response in the substrate should be almost the same as though the dielectric were not present on its surface.

In an attempt to better qualify the validity of ignoring thin dielectrics in simulating the body current responses to dielectric discharges, the following analyses were performed.

First, the analysis and results of Ref. 33 were reviewed, keeping in mind their application to the spacecraft discharging problem. Boyd considers a cylindrical conducting can (180 cm in height and 30 cm in diameter) covered with a dielectric of uniform thickness and immersed in ionized air with a spatially-uniform axial Compton current density $J_z(t)$. He calculates the axial current in the can at its equator and the normal electric field inside the dielectric at the center of the endcap. Figure 34 is a reproduction of his results for three radiation intensities and three thicknesses of the dielectric (0, 0.15, and 1.5 cm). For the two smallest dose rates, there is only a minor difference (<20 percent) between the curves for no dielectric and a dielectric with a thickness of 0.15 cm. Even at the largest dose rates, the peak currents differed by only a few percent. The form of his equation and his calculated results indicate that the effect of the dielectric decreases with decreasing thickness of the dielectric. Thus, for realistic dielectric thicknesses ($\lesssim$0.025 cm), the effect of the dielectric would be very small for this problem. However, there is a question whether the problem that was simulated in Ref. 33 is sufficiently severe to draw a general conclusion about the lack of importance of the dielectric for dielectric discharge problems. Consequently,

101
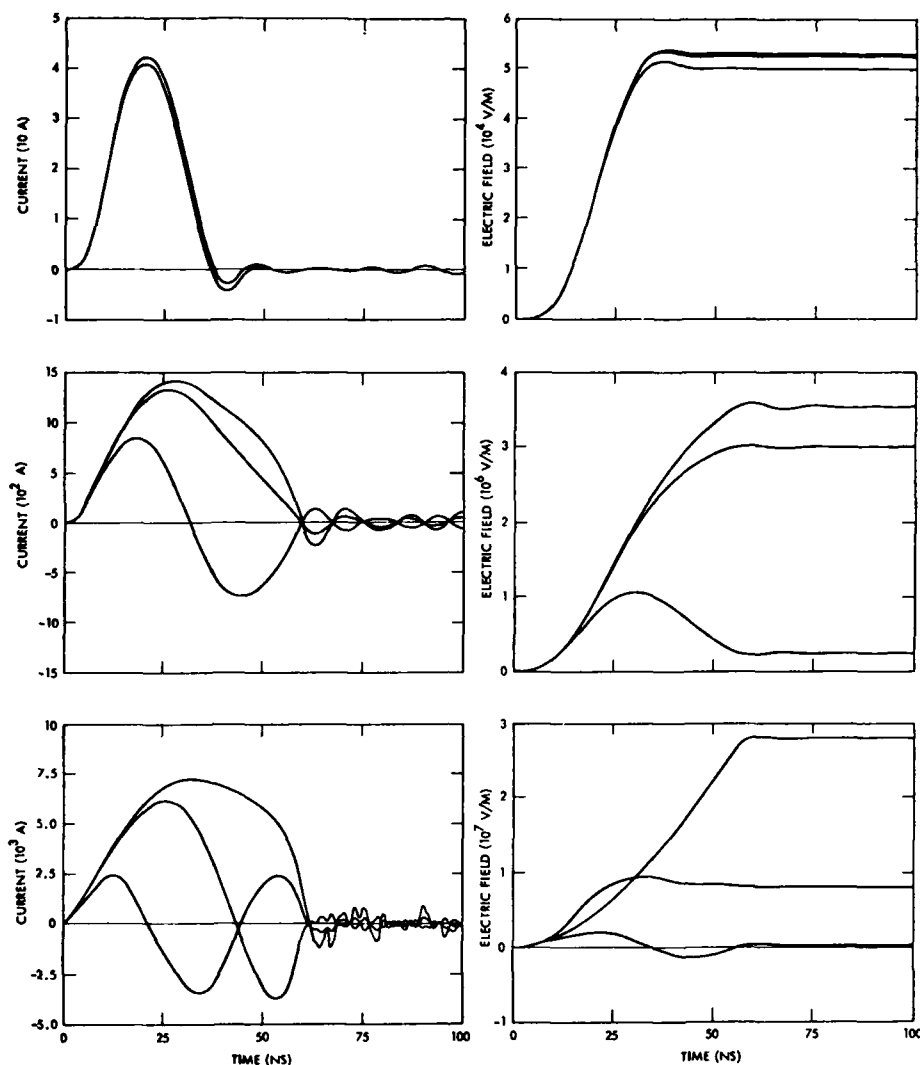
Figure 34

Electrical response of insulated cylinder whose radius is 0.15 m, height 0.9 m if insulated post on perfectly conducting plane, length 1.8 m if insulated cylinder suspended in air. Base or equatorial current (left) and internal electric field in the dielectric at the center of the end cap (right) for three environments: radiation intensities of 10^9 (top), 10^{11} (middle), 10^3 (bottom) roentgens/second for 1 MeV photons and air at one atmosphere pressure. The corresponding peak Compton currents and air conductivities are, respectively, 20 A/m^2 and 9.5E-4 MHOS/m (top), 2.E3 A/m^2 and .18 MHOS/m (middle), 2.E5 A/m^2 and 18 MHOS/m (bottom). The three insulator thicknesses represented on each plot are infinitesimal, R/100, R/10, where R is cylinder radius. The early current and late electric field go down as insulator thickness increases. (Reproduced from Reference 33).

102

computer calculations were made for two scenarios that have some of the fetures of dielectric discharges.

The first problem consisted of a conducting cylindrical can with 1 m radius and 0.93 m height. One end and the cylindrical sides of the can were covered with 0.5 cm of dielectric with a relative dielectric constant of 4. The driving function for the problem was a triangular pulse of electrons (10 ns up and 10 ns down) emitted uniformly in area from the end of the can that was covered with the dielectric. The emission was from the outside of the dielectric. The skin currents in the conducting walls of the can (that is, the magnetic fields in the first zone outside the conducting walls) were compared to the corresponding skin currents when the same electron emission was from the end of a bare can and there were no dielectrics on the can. The calculation for the can with the dielectric corresponds to the real situation for the outward emission of charge during the discharge of a relatively thick (0.5 cm) dielectric. The calculation for the can with no dielectric is the way we are simulating discharges on SCATSAT. The presence of the 0.5 cm dielectric reduced the skin currents on the side of the can by less than 20 percent. This amount of change is not significant in the assessment of discharge effects and, based on Boyd's results, we would expect the effect to be even less for thinner dielectrics.

The second computer problem, which was suggested by Roger Hill of SAI, was similar to the first. A conducting cylinder with radius equal to 0.685 m and height equal to 0.83 m is located inside a much larger conducting cylinder. Half of the sides of the inner cylinder is covered with 0.5 cm of dielectric with a relative dielectric constant of 2.5. The driving function for this problem was a triangular current pulse (9 ns up and 9 ns down) from the surface of the dielectric radially outward to the outer cylinder. The current density was uniform over the area of the dielectric. Again, this scenario approximates what happens when charge is emitted outward from a dielectric during a discharge. The skin currents in the conducting walls of the cylinder were again compared to the skin currents on a bare cylinder when the current pulse went directly from the bare walls of the inner cylinder to the outer cylinder and there was no dielectric on the cylinder. The calculation for the bare can corresponds to the simulations on SCATSAT, ignoring thin dielectrics. As in the previous problem, the presence of the 0.5 cm dielectric caused only small differences in the skin currents, less than 5 percent close to the edge of the dielectric and on the order of 1 percent further away. For a realistic dielectric thickness, the effect is expected to be even less.

When the above problem was proposed by Roger Hill, the plan was to charge up the surface of the dielectric with the current pulse from the outer cylinder, allow the electromagnetic transients from the charge-up to die away, and then short the radial capacitors in the code that represent the dielectric. This shorting process would allow the charge on the surface of the dielectric to flow to the substrate, representing a punchthrough that is uniform over the dielectric area. The resulting collapse of the dipole field from the charged dielectric sheet would produce skin currents in the conducting cylinder. It was planned to perform the calculations for two thicknesses of dielectric (0.5 and 0.1 cm) and compare the skin currents for comparable initial dipole moments. Also, we planned to examine the numerical values of the various terms in Equation 4 of Ref. 33 during the punchthrough process to see how important the dielectric is.

Unfortunately, the same problem of damping out the charge-up oscillations that is discussed in Section 6.4 for the arc discharge calculations occurred in this case also. Even with a fairly long delay between charge-up and the shorting, the residual oscillations in the skin currents were comparable to the currents induced by shorting the dielectric. This result complicates making a meaningful numerical comparison of the relative effects of the two dielectric thicknesses. As an alternative, we have examined the magnitude of the terms in Equation 4 of Ref. 33 during the charge up.

The original purpose of this last calculation was to provide data to numerically evaluate the magnitude of the term in Boyd's boundary equation that is proportional to the dielectric thickness in order to see what would be the result if the thin dielectric were completely ignored. The pertinent formula is

$$\frac{\partial Hy}{\partial t} = \frac{E_x}{\left[\frac{\Delta z}{z} + d\right]} - \frac{\left[\frac{\Delta z}{z} \frac{\partial E_z^+}{\partial x} + \int_0^d \frac{\partial E_z^-}{\partial x} dz\right]}{\left[\frac{\Delta z}{z} + d\right]} .$$

For our cylindrical geometry, the z coordinate corresponds to the radial direction; x to the axial direction; and y to the azimuthal direction. The thickness of the dielectric is d and the superscripts (-) and (+) on E_z denote values inside the dielectric and in the first mesh zone outside the dielectric respectively.

If d is set equal to zero, the above equation is the usual finite - difference form for Faraday's law adjacent to a perfect conductor since tangential E (i.e., E_x) is zero

inside a conductor. Therefore, the importance of including the thin dielectric in the simulation can be judged by comparing the magnitudes of $\partial H_y / \partial t$ with $d = 0$ and with d equal to its proper value.

In the present simulation, which used $d = 0.5$ cm, the magnitudes of E_z^- before the simulated collapse of the trapped charge from the dielectric to the substrate were very comparable in magnitude to E_z^+ at all axial positions along the cylinder. Moreover, E_z^- varies relatively slowly with axial position (except right at the edge of dielectric) and $\partial E_z^- / \partial x$ is comparable to $\partial E_z^+ / \partial x$. Therefore, before the simulated discharge, the ratio of the integral term from $z = 0$ to d to the term $\Delta z/2$ times $\partial E_z^+ / \partial x$ is approximately $d/\Delta z$, which would be a very small number for a realistic value for d. Moreover, when the charge on the dielectric discharges to the substrate, E_z^- goes to zero. If the rate at which it goes to zero is faster than the rate at which the outer electromagnetic fields return to equilibrium, the relative magnitude of the integral term across the dielectric during the discharge will be even smaller than the ratio $d/\Delta z$. Therefore, for this simulated problem, it is concluded that including Boyd's boundary condition in the code with a realistic value for d would have produced only a minor change in the return currents compared to what was calculated completely neglecting the thin dielectric.

It is, of course, possible to think of situations where the integral term in Boyd's equation is not negligible. Obviously, it was not negligible in the problem Boyd analyzed when the dose rate was large. However, it appears that, for realistic situations for spacecraft charging, the effect of thin dielectrics will be small and a good simulation of the return currents due to a dielectric discharge can be obtained neglecting the presence of the thin dielectrics.

6.4 COMPUTER SIMULATION OF POSTULATED DISCHARGE MECHANISMS

As discussed in Section 3.4, an effort was made to determine the relative effectiveness of a collapsing dipole potential and the radiative field due to the arc discharge compared to outward emission of charge in producing structural return currents. The preliminary analysis in Section 3.2 indicates that the effects of the collapsing dipole and radiative fields are relatively small compared to the effect of outward emitted charge. To confirm this conclusion, SABER computer calculations have been made for a driver which approximates the can arc discharge experiment (Section 3.4) and for a simulated capacitive drive from the end of the can. Also, the ABORC computer code (Ref 31) was used to simulate actual outward emission of charge

as might occur in a dielectric discharge. These analyses are described in Sections 6.4.1, 6.4.2, and 6.4.3. Section 6.4.4 discusses the way to scale the return currents from the different driving mechanisms. The calculated currents are compared to the results of the arc discharge experiments in Section 6.4.5.

6.4.1 Computer Simulation of an Arc Discharge

The SABER code was used for this simulation. Basically, we tried to simulate the experimental configuration illustrated in Figure 3.

However, in order to avoid extremely small computation time steps, the space between the can and the conducting plate was increased to 1 cm for the computer simulation. It is felt that this change will not adversely affect the usefulness of the results because the 1 cm spacing is still quite small compared to other dimensions of interest. The calculated results have to be scaled to correct them to the proper spacing (i.e., capacitance). The method of scaling is discussed in Section 6.4.4. The grid system that was used is summarized in Table 16.

Table 16. Grid Zones for the Simulation of the Can Arc Discharge Experiment

Radial (r) Zones[1]	0, .05, .1, .16, .225, .28, .32, .36, .4, .45, .5, .55, .5925, .635, .685, .75, .82, .92, 1.06, 1.25, 1.5, 1.85, 2.35, 3.0, 3.85, 4.95, 6.0, 7.3, 9.0, 11.0
Axial (z) Zones	-8, -5.7, -4.30, -3.3, -2.51, -1.95, -1.55, -1.27, -1.07, -.93, -.83, -.73, -.64, -.55, -.46, -.367, -.255, -.175, -.119, -.079, -.051, -.031, -.017, -.007, 0., .005, .01, .017, .027, .037, .05, .068, .093, .128, .178, .248, .348, .488, .688, .969, 1.36, 1.9, 2.6, 3.6, 5.0, 6.9, 9.5, 12.0
Azimuthal (φ) Zones[2]	0, 36, 72

1. Linear dimensions in meters
2. Angular zoning in degrees
3. Top of can is z=0; the conducting plate is contained between z=0.01 m to z=0.017 m
4. See Figure 3 for an illustration of the simulated plate

In the first attempts with this simulation, we tried to approximate the actual sequence of events in the experiment. The plate was charged up by a current pulse from the can to the plate; a time was allowed for the electromagnetic oscillations caused by the charging-up to damp out; and then the mesh zones from the tip of the plate to the can at the centerline of the can were shorted to represent the arc breakdown. Unfortunately, there were two difficulties with this approach. First, unless a very slow charge-up and a long delay time before the discharge were used (which

requires extensive computation time), the residual electromagnetic oscillations were comparable in magnitude to the response produced by the discharge process. Various attempts to artifically damp out the oscillations and then remove the artificial damping before initiating the discharger were not especially successful, and sometimes made the situation worse. The second problem was that great care had to be used in initiating the discharge. If the electric fields along the mesh lines that represent the short region were abruptly set to zero, the curl of E in the adjacent regions (which is one of the electromagnetic driving terms in the code) would suddenly assume large values which then propagated throughout the problem and gave extremely noisy results. When considering these difficulties, one should remember that the process of shorting the meshes midway through a problem is a very non-standard operation for the SABER code, and probably for most SGEMP codes. The electromagnetic properties of certain mesh regions, in particular the electrical conductivity, have to be changed during the problem.

Because of these difficulties, it was decided not to try to duplicate the steps in the experimental sequence. Instead, starting from time zero and no potential on the plate, a current source was applied along the centerline of the can from the can to the tip of the plate. The time history of the driving pulse was made the same as the experimentally-measured discharge current (Figure 4). Since the initial static potential on the plate has no effect on the body currents (only the rates of change of the potential are important), and since the electromagnetic equations in the code are completely linear, this process should give a reasonably correct simulation of the body currents due to the arc discharge.

Figures 35 and 36 show calculated time histories of the axial body currents (actually azimuthal magnetic fields $B\phi$ just outside the body) at locations on the body corresponding to two of the sensors (1 and 3; see Figure 3). These results are scaled and compared to the currents generated by other driving mechanisms in Section 3.4.4.

6.4.2 Computer Simulation of Blowoff

The purpose of this calculation was to study the effect of the charge that is emitted outward during a discharge. The ABORC SGEMP code for arbitrary bodies of revolution (Ref 31) was used for this calculation. Charge was emitted uniformly from the end of the can without the arc-discharge plate in place. A triangular emission pulse, 10 ns up and 10 ns down, was used with a very low peak current density

107
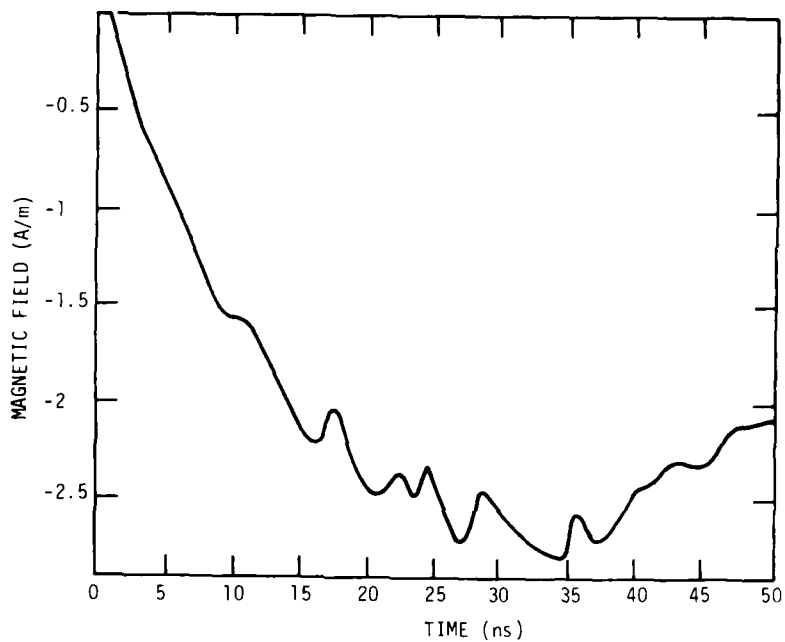
RT-17169

Figure 35. Calculated azimuthal magnetic field at sensor position 1 for simulated
arc discharge problem
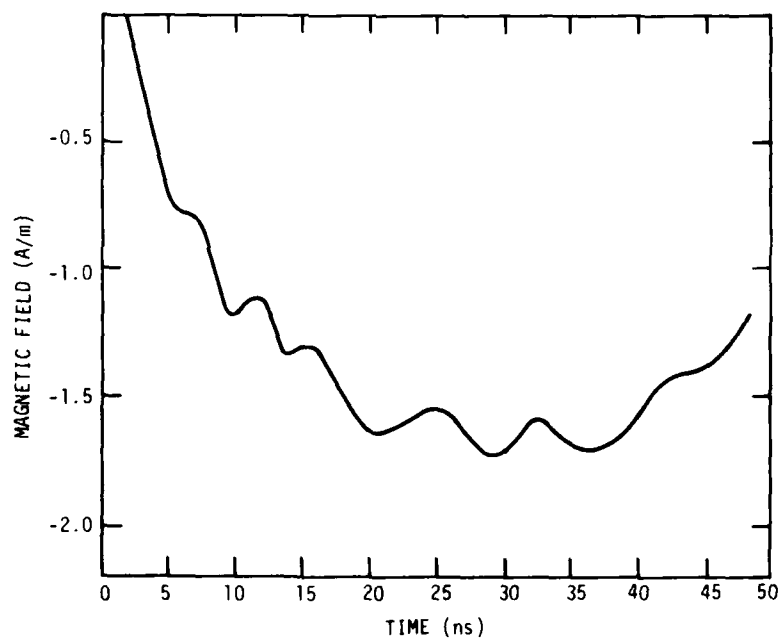
RT-17168

Figure 36. Calculated azimuthal magnetic field at sensor position 3 for simulated
arc discharge problem

108

(10^{-5} A/m^2) to make sure that space-charge-limiting does not occur in the simulation. Since dielectric surfaces that break down will usually have a negative surface potential, space-charge-limiting is not expected to be signficant for outward charge emission during a discharge. Typical calculated time histories of the surface azimuthal magnetic fields near sensors 2 and 3 are shown in Figures 37 and 38. These results are scaled and compared to the currents generated by other driving mechanisms in Section 3.4.4.

6.4.3 Computer Simulation of Capacitive Drive on End of Can

To complete the comparisons, the SABER code was used to simulate a capacitive drive on one end of the can corresponding to the ou tward emission of electrons. The capacitor plate was placed 35 cm from the end of the can and its size was the same as the end of the can. The plate was driven by a current pulse along the axis of the cylindrical can from the end of the can to the plate. The driving pulse was triangular, 10 ns up and 10 ns down. The peak driving current was arbitrarily chosen as 1 amp since the problem is linear and the results can be scaled.

Figures 39 and 40 show azimuthal magnetic fields near sensors 1 and 3. These results are scaled and compared to the currents generated by other driving mechanisms in Section 3.4.4.

6.5 PREDICTION OF SCATSAT EXTERNAL BODY RESPONSES

6.5.1 Model

The SABER computer code (Ref 30) has been used to simulate the capacitive-drive electrical tests on the SCATSAT model without booms. This code is a three-dimensional finite-difference formulation of the fully-dynamic Maxwell's equations in cylindrical coordinates. The exterior body of SCATSAT has been approximated as a fully-enclosed, perfectly-conducting cylindrical can with a cylindrical recess for the AIM cavity. The experimental data (q.v. Section 5.5) indicates that for the SCATSAT and P78-2 that this assumption, typically made for approximately cylindrical spacecraft (like SKYNET or DSCS-II) may not always be valid. It appeared to be true for the latter two spacecraft. The degree to which this approximation is valid depends on detailed structure of the satellite. Due to the computational difficulties of accurately simulating small slots and gaps with SGEMP computer codes and the penetration of electromagnetic fields through thin metallic skins with finite conductivities, the
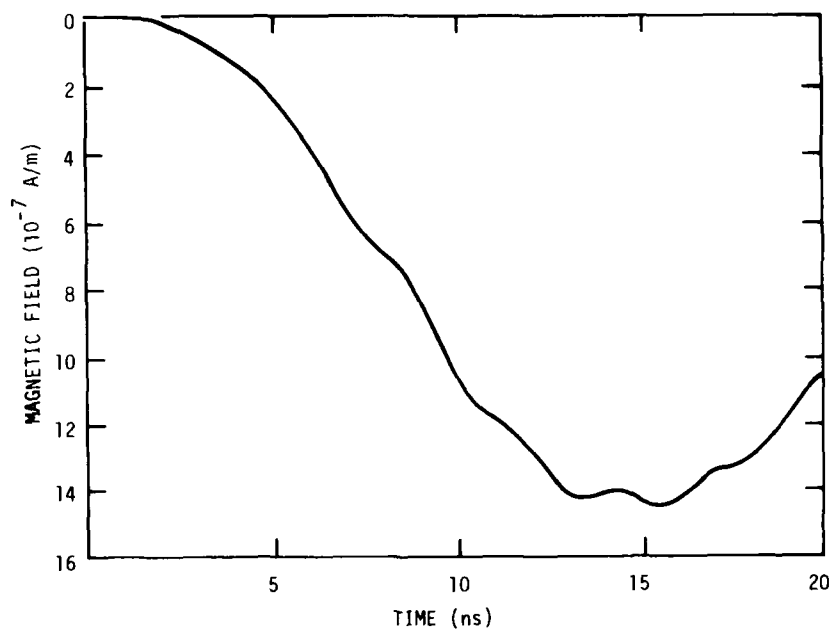
RT-17161

Figure 37. Calculated azimuthal magnetic field at sensor position 2 for outward emission of charge
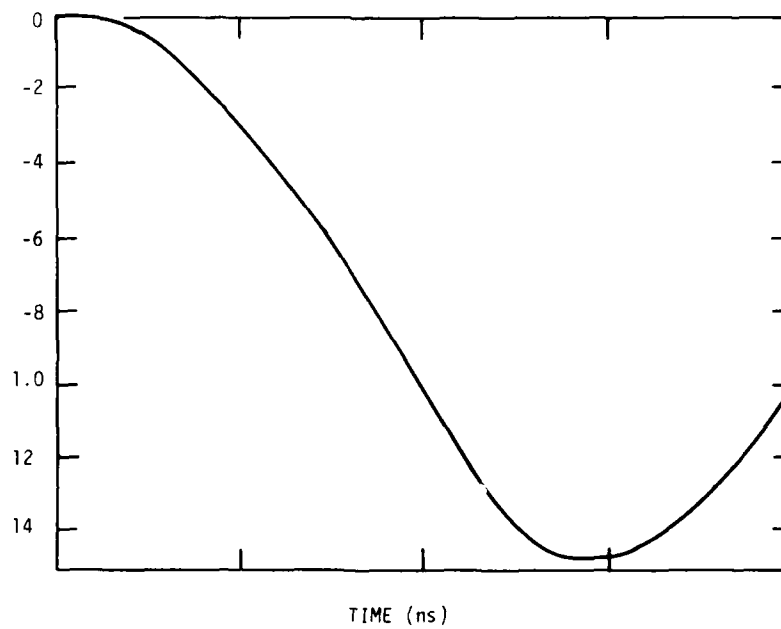
RT-17155

Figure 38. Calculated azimuthal magnetic field at sensor position 3 for outward emission of charge

110
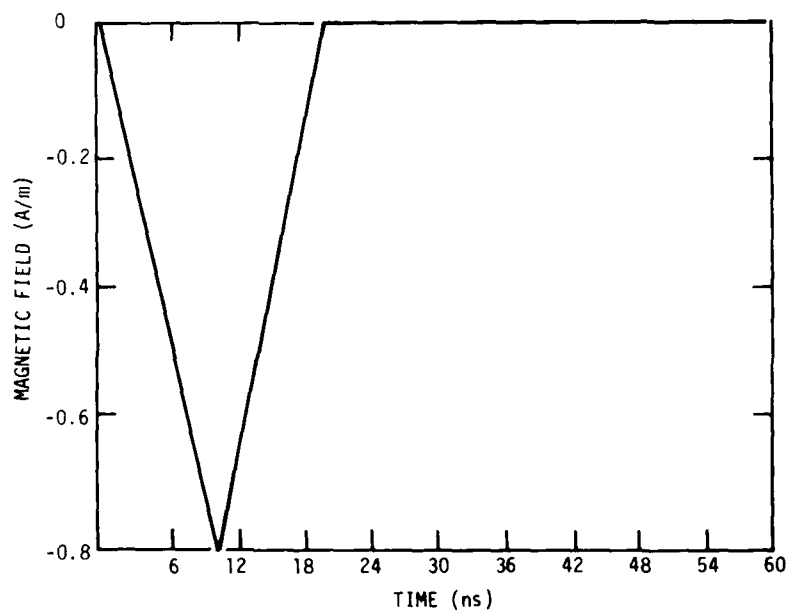
RT-17164

Figure 39. Calculated azimuthal magnetic field at sensor position 1 for
simulated capacitive drive
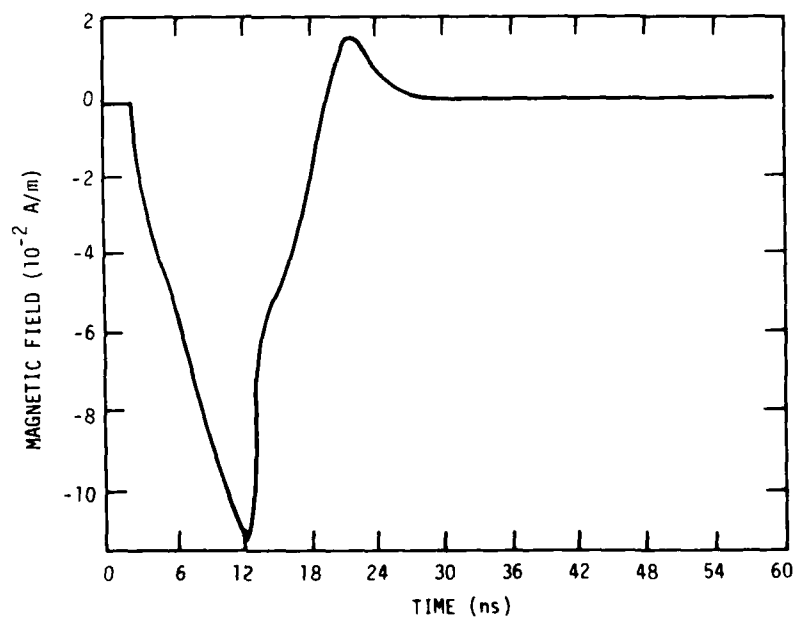
RT-17160

Figure 40. Calculated azimuthal magnetic field at sensor position 3 for
simulated capacitive drive

111

penetration of the external fields into the interior cavities of SCATSAT and coupling into the cable bundles are not considered in these calculations. These penetrations and cable couplings must be estimated by analytic techniques, using the calculated body currents in the absence of any penetrations. This is an important task which remains to be done.

The booms on SCATSAT have not been included in these calculations because it is not practical to correctly simulate in SABER the inductances, and hence the transient responses, of the booms. The only continuous electrically conductive paths along the booms on SCATSAT are the cables that bring the information from the experiments on the tips of the booms back to the satellite body. Hence, the response of the booms and their effect on the body responses will be controlled to a large extent by the inductances of these cables. In SABER, the inductance of a conducting line (represented by a continuous string of shorted capacitors) is a function of the grid sizes immediately surrounding the conducting line. Hence, to correctly approximate the inductances of the cables, the meshes which represent the booms, or cables, would have to be comparable to the cross-sectional dimensions of the cables. Such small mesh sizes would require extremely small computational time steps and would be impractical for the present problems. Thus, rather than simulating the booms with unrealistic inductances, which could lead to misleading results and conclusions, it was decided that it would be best to simulate only the SCATSAT without the booms and compare the results to the corresponding experiments without booms. The results will provide an indication of how well we can predict, and understand, the responses on a simple configuration. The effect of the booms on the body responses will have to be analyzed by some lumped-element equivalent circuit model.

The grid system used in the calculations is given in Table 17. This choice of the three grids is a compromise between accuracy of simulation and the maximum number of permissable meshes and computation time.

The SABER code requires that the simulated body be enclosed inside a large container. The closest distance from the SCATSAT boundaries to this outer cylinder (from bottom of SCATSAT) is about 3.6 m which corresponds to a clear time (round trip at the speed of light) of 24 ns. For excitations on the top and sides of the vehicle, the clear time is around 40 ns. For simulation times greater than these clear times, the calculated body responses will start to be influenced by the electromagnetic waves reflected from the outer walls.

Table 17. Grid Zones for Simulation of SCATSAT

Radial (r) Zones[1]	0., .0628, .1256, .1781, .2156, .2424, .2616, .2753, .2851, .2921, .2971, .3036, .3121, .3232, .3376, .3563, .3806, .4122, .4438, .4754, .5994, .6180, .6555, .7080, .7810, .8830, 1.025, 1.223, 1.450, 1.837, 2.377, 3.127, 4.177, 5.647, 7.0
Axial (z) Zones	-4.8, -4.1, -3.5, -3.074, -2.534, -2.147, -1.87, -1.6721, -1.53, -1.428, -1.3551, -1.3026, -1.2651, -1.2383, -1.2191, -1.2054, -1.1956, -1.1886, -1.1836, -1.1766, -1.1668, -1.1476, -1.1208, -1.0833, -1.0308, -.9541, -.8776, -.8011, -.7245, -.6515, -.599, -.5615, -.5347, -.5155, -.5018, -.492, -.485, -.480, -.4729, -.4630, -.4492, -.4299, -.403, -.3655, -.3130, -.2395, -.1665, -.1140, -.0765, -.0497, -.0305, -.0168, -.007, 0.0, .005, .012, .0218, .0355, .0547, .0815, .119, .1715, .2445, .3465, .4885, .6865, .9635, 1.3505, 1.89, 2.64, 3.6, 4.8, 6.0
Azimuthal (ϕ) Zones[2]	0, 45, 90, 135, 180, 225, 270, 315, 360

1. Linear dimensions in meters
2. Angular zone in degrees
3. The SCATSAT extends from z=0.0 to z=-1.103 cm and from R=0 to R=0.5639 m.
4. See Figure 24 for an illustration of the drive set up.

The capacitive drive is simulated as a conducting sheet with the same area and separation from the SCATSAT body as in the actual electrical tests. Due to the limitations of the grid system, the acrual drive plate (flat and circular) had to be approximated by pie-shaped or partial-cylindrical sections. However, it is felt that any inaccuracies resulting from this approximation are relatively minor. The electrical driving pulse is simulated as a current source, with the desired pulse shape, from SCATSAT to the plate. This simulated current source has infinite impedance in the calculations so there is no return current from the plate to SCATSAT, either during or after the driving pulse.

In the code, it is possible to record the electromagnetic fields or currents at any of the grid points. The most important quantities from the standpoint of penetration and couplings and for comparison to experiment are the body skin currents. Consequently, the magnetic induction fields just outside the body and tangential to the skin (B_ϕ and either B_z or B_r) were recorded at the points illustrated in Figure 41. These points were selected to give coverage at various axial and radial positions on the body and at approximately zero, 90 , and 180 in the azimuthal (ϕ) direction from the drive locations. Since the simulated SCATSAT body, without penetrations or booms, is cylindrically symmetric, one set of calculations is applicable to all azimuthal locations of the driver.

113
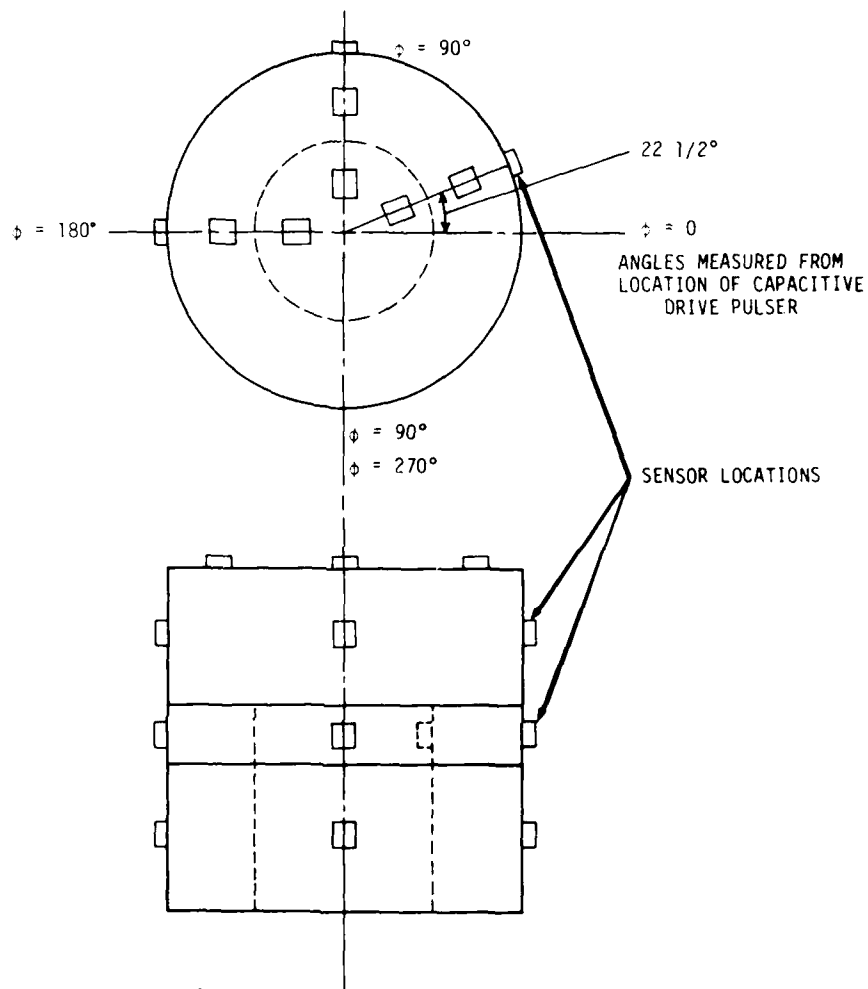
RT-17167

Figure 41. Locations where calculated surface magnetic fields are recorded for simulated capacitive drive of SCATSAT

6.5.2 Calculated Results for SCATSAT

Calculations were made for the SCATSAT model without booms for five locations of the capacitive drive (points A,B,C,E and G in Figure 21) with the fast pulse drive (Figure 26). Typical time histories for the surface magnetic field on the SCATSAT are shown in Figure 42.
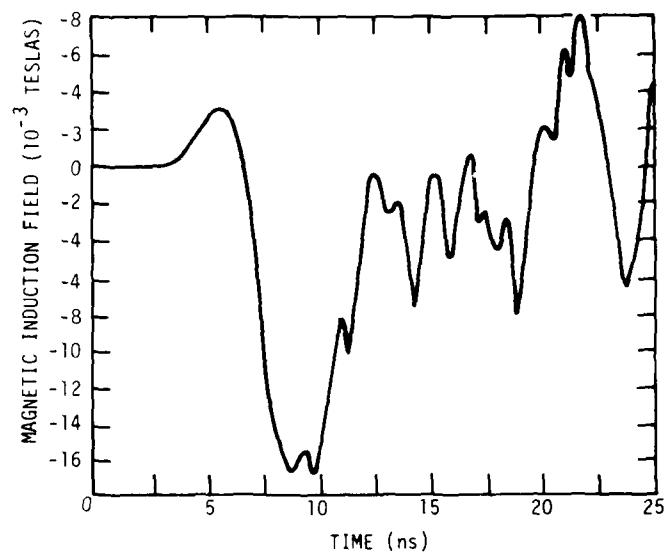
(a) SENSOR 2 DRIVE POINT C
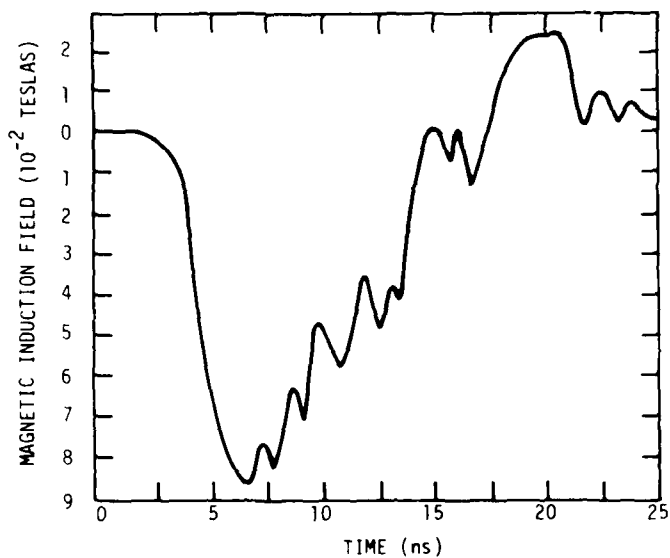
(b) SENSOR 7 DRIVE POINT B

RT-17162

Figure 42. Representative SCATSAT body responses as predicted by the SABER code

115

Since the measured quantities in the experiments are the rates of change of the magnetic induction ($\dot{B}$)*, the calculated time histories of the magnetic induction fields were differentiated graphically and the maximum values $\dot{B}_{max}$ for the various drive and observation points are summarized in Table 18. In general, the listed values of $\dot{B}$ are average values over significant portions of the calculated time histories. Small oscillations with higher frequencies have been averaged and, thus, these calculated values of $\dot{B}$ should be compared to average experimental results ignoring higher frequency oscillations. Although the signs of the peak $\dot{B}$ values are given in Table 18, one should not attach too much significance to the relative signs of different sets of data because the peak rate of change of B did not always occur at comparable positions on the oscillatory time histories.

The calculated $\dot{B}_{max}$ values are compared to the available corresponding measured values in Table 19. Note that in Table 19 the sensor orientations (ϕ or z) are specified for $\dot{B}$ rather than $\dot{J}$ so that the measured values are interchanged from their listing in Table 18. Also, while the comparisons are ostensibly for the no boom configuration only one third of the available measured values are actually for the no boom case.

Consider the circumferential fields, $\dot{B}_\phi$, for the symmetric drive A. Sensors 2 and 7 on the side of the SCATSAT near the top agree with the calculated $\dot{B}$ at these locations within a factor of 2 either way. Sensor 4 at the bottom of the side is in excellent agreement. Sensor 3 shows a marked disagreement, however, to a factor of ~5. As already discussed in Section 5, the measured response of this belly band sensor was much higher than expected for a continuous conducting object. Since the analytic model was exactly that, it's calculated response is therefore much lower than the measured response. The axial fields, $\dot{B}_z$, are of course predicted to be zero since symmetric drive does not force any circumferential currents on a symmetric object. The measured $\dot{B}_z$ are actually quite large since the real object is not symmetric.

Consider next circumferential fields for the asymmetric drive of the top of SCATSAT drive B. The three sensors for which measured data are available agree within about a factor of 2 either way with the calculated values. No axial fields were measured for this drive.

---

*Actually expressed as $\dot{J}$ but in units of $\dot{B}$. A conversion of $\dot{J}(amp/m^2 sec) = \dot{B}(teslas/sec)/4\pi 10^{-7}$ is reasonably accurate.

Table 18. Calculated $\dot{B}_{max}$ for SCATSAT Without Booms

ϕ (a)	z(b)	r		Field Component	A(c)	B	G	C	E
22	+0.0025	0.2685	Top	$\dot{B}_\phi$	-724.0(d)		+186.0	+171.0	+107.0
	+0.0025	0.2685		$\dot{B}_r$	0.0		+130.0	+86.1	+75.8
	+0.0025	0.5481	Top	$\dot{B}_\phi$	-256.0		+233.0	+306.0	+251.0
	+0.0025	0.5481		$\dot{B}_r$	0.0		+362.0	+231.0	-136.0
	-0.0401	0.5664	Outside	$\dot{B}_\phi$	-141.0		+586.0	+494.0	+476.0
	0.5803	0.5664		$\dot{B}_z$	0.0		-348.0	-200.0	-116.0
	-0.5664			$\dot{B}_\phi$	-65.6	-177.0	-680.0	-659.0	+715.0
	-0.5803	0.5664		$\dot{B}_z$	0.0	+54.1	+258.0	-389.0	-220.0
	-1.1720	0.5664		$\dot{B}_\phi$	-37.1	-101.0	-319.0	-421.0	-372.0
	-1.1720	0.5664		$\dot{B}_z$	0.0	-79.0	-141.0	-229.0	-381.0
	-0.4885	0.2886	Cavity	$\dot{B}_\phi$	-10.7		+10.7	+6.8	+16.0
	+0.0025	0.2685		$\dot{B}_\phi$			+48.8	-36.0	-37.6
	+0.0025	0.2685		$\dot{B}_r$			+26.0	+26.2	+25.1
	+0.0025	0.5481		$\dot{B}_\phi$			-29.8	-21.4	-13.9
	+0.0025	0.5481		$\dot{B}_r$			+52.1	+42.0	+35.7
	-0.0401	0.5664		$\dot{B}_\phi$			-18.8	-14.0	-12.0
	-0.0401	0.5664		$\dot{B}_z$			-39.3	-46.6	-23.3
	-0.5803	0.5664		$\dot{B}_\phi$			-14.3	-5.4	-13.3
	-0.5803	0.5664		$\dot{B}_z$		-31.7	-15.5	-15.2	-15.6
	-1.1720	0.5664		$\dot{B}_\phi$		-14.0	+11.4	+12.6	+24.2
	-1.1720	0.5664		$\dot{B}_z$		-25.3	-29.3	-36.0	-50.0
	-0.4885	0.2886		$\dot{B}_\phi$		24.7	-18.9	-20.5	-18.4
	+0.0025	0.2685		$\dot{B}_\phi$	(c)		-52.9	-37.9	-31.8
	+0.0025	0.2685		$\dot{B}_r$			+7.6	+7.5	+9.6
	+0.0025	0.5481		$\dot{B}_\phi$			-29.9	-20.0	-12.5
	+0.0025	0.5481		$\dot{B}_r$			-15.5	+16.7	+21.4
	-0.0401	0.5664		$\dot{B}_\phi$			-25.9	-13.0	-10.4
	-0.0401	0.5664		$\dot{B}_z$			-11.9	-13.2	-16.2
	-0.5803	0.5664		$\dot{B}_\phi$			-19.7	-2.2	-13.4
	-0.5803	0.5664		$\dot{B}_z$			-7.5	-1.5	-7.5
	-1.1720	0.5664		$\dot{B}_\phi$			+11.0	+16.4	+22.1
	-1.1720	0.5664		$\dot{B}_z$			-20.8	-16.8	-15.0
	-0.4885	0.2886		$\dot{B}_\phi$			-12.5	-16.5	+11.7

[a] measured from azimuthal location of the drive point (See Table 17)

[b] z measured from the top of can. Dimensions in meters

[c] The responses for drive position A are cylindrically symmetric

[d] The units are Teslas/sec.

Table 19. Comparison of Measured and Calculated $\dot{B}$ for SCATSAT Without Booms

Drive Point	$\dot{B}$ Sensor	Peak $\dot{B}$ (Teslas/sec)	
		Calculated	Measured
A	$2_\phi{}^a$	-150	-76
	z	0	-54
	3_ϕ	-70	+340
	z	0	-24
	4_ϕ	-40	-36^b
	7_ϕ	-150	$+220^b$
B	2_ϕ	-320	-290^b
	4_ϕ	-110	-49^b
	7_ϕ	-70	$+130^b$
C	2_ϕ	-14	+91
	4_ϕ	+17	-28
	5_ϕ	+180	$+130^b$
	6_ϕ	-40	-38^b
	7_ϕ	+530	+680
G	2_ϕ	+28	-82^b
	4_ϕ	+12	$+26^b$
	5_ϕ	+200	$+140^b$
	6_ϕ	-56	-23^b
	7_ϕ	+620	-100^b

[a]Since $\dot{B}$ is measured $\dot{B}_\phi$ corresponds to $\dot{J}_z$ or $\dot{J}_r$ depending on sensor location

[b]With booms - data not taken for no boom configuration

Drive C produced agreement within a factor of two or better for four or five circumferential field measurements. The one exception was sensor 2 where the measured value was a factor of 6.5 higher than the prediction. The very large measured response of this sensor was also discussed in Section 5 and no credible explanation for this response exists.

Drive G produced agreement within a factor of 2.5 for 3 of the five circumferential field measurements. Sensor 2 is again higher than predicted, by a factor of about 3. However, sensor 7 shows a much lower measured response than before and is lower than the prediction by a factor of 6.2. No explanation exists for the dramatically lower measurement. It is possibly a bad data point since it was measured only once.

The frequencies are compared in Table 20. Unfortunately, the calculated frequencies are very difficult to determine because the computer runs were terminated after only 25 ns. Thus, lower frequencies do not show up in the calculations because they would cover much less than a full period in the plots.

Table 20. Comparison of Measured and Calculated Frequencies for SCATSAT

Drive Point	$\dot{B}$ Sensor	Frequency (MHz)	
		Calculated	Measured
A	2ϕ	---	180
	$2z$	---	73 + HF
	3ϕ	Poss 200	61
	$3z$	---	176
	4ϕ	Poss 200	76/37[a]
	7ϕ	?	230/74[a]
B	2ϕ	200	150[a]
	4ϕ	~200	210/~50[a]
	7ϕ	200	170/38/60[a]
C	2ϕ	200	200
	4ϕ	80 +HF	200
	5ϕ	?	110/37[a]
	6ϕ	~200	220/110[a]
	7ϕ	?	90
G	2ϕ	~200	170/~50[a]
	4ϕ	~80	39/200[a]
	5ϕ	?	120/33[a]
	6ϕ	~200	180[a]
	7ϕ	?	180/70[a]

[a]Measured with booms

The only two frequencies which appear in the calculations are ~80 MHz and ~200 MHz. These same frequencies appear in the measured responses. Not much more than this can be reasonably concluded from the limited analytical data.

Summarizing the comparisons of analytical and experimental results, the following conclusions are drawn.

1.   The computer model, which treated the exterior surface of the SCATSAT as a continuous conductor, produced predictions which agree with the experimental data within a factor of 2.5 or better in all but three cases. In

119

two of the cases, there is sufficient corroboration of the experimental value to suggest that the prediction is in error as a result of inadequate detail in the model, i.e., representing SCATSAT as a continuous conductor. In the third case, there is no corroberation of the experimental data and no logical reason for it and so the experiment may be in error.

2. Frequency content is difficult to compare but it appears that the model would predict the correct frequencies if the problem were carried out far enough. Unfortunately this becomes very expensive. A run to 100 ns would consume one hour of computer time. One of the unaddressed analytic problems is the development of a normal mode or lumped element method of analysis which could be used to follow the coupling response out to longer time periods (in 1 μsec for use of the lower frequency modes). As a first cut it is suggested that at least a couple of cases be run both with SABER out to 100 ns. This would take 4 hours of computer time and about $2500 (at AFWL) and provide data for code comparison with alternate modeling techniques.

REFERENCES

1. D.A. McPherson and W. Schober, "Spacecraft Charging at High Altitudes: The SCATHA Satellite Program," in A. Rosen (Ed.), Progress in Astronautics and Aeronautics, Vol. 47, MIT Press, 1976, p. 15 ff.

2. R. D. Lovell, N. John Stevens, W. Schober, C. P. Pike and W. Lehn, "Spacecraft Charging Investigation: A Joint Research and Technology Program," ibid., p. 3 ff.

3. C. P. Pike and M. H. Bunn, "A Correlation Study Relating Spacecraft Anomalies to Environmental Data," ibid., p. 45 ff.

4. A. Rosen, IEEE Trans. Nucl. Sci. 23, 1762 (1976).

5. R. Leadon, A. Weiman, and R. Keyser, "Electrical Simulation of Electrostatic Discharges in Dielectrics," IEEE Trans. Nucl. Sci. (to be published Dec 1978).

6. A. Muelenberg, "Evidence for a New Discharge Mechanism for Dielectrics in a Plasma," in Reference 1, p. 237 ff.

7. A. Pavel, Proceedings of the Spacecraft Charging Technology Conference, C. P. Pike and R. P. Lovell (Eds.), AFCL TR-77-0051 (1977), p. 53 ff.

8. Martin Marietta Aerospace, P78-2 EMC Test Plan, TL-5827002.

9. G. T. Inoye, A. C. Whittlesey, S. R. Ponamgi, B. D. Cooperstein and A. K. Thomas, "Voyager Spacecraft Electrostatic Discharge Immunity Verification Tests," presented at the Symposium on the Effects of the Ionosphere on Space and Terrestrial Systems, Jan 24-26, 1978.

10. q.v. Ref. 7, executive summary, pp. 9-20.

11. I. Katz, D. E. Parks, M. J. Mandell, J. M. Harvey, D. H. Brownell Jr., S. S. Wang and M. Rotenberg, "A Three Dimensional Dynamic Study of Electrostatic Charging in Materials," NASA CR-135256, August 1977.

12. V. A. J. van Lint, D. A. Fromme and J. R. Rutherford, "Spontaneous Discharges and the Effect of Electron Charging on SKYNET SGEMP Response," IEEE Trans. Nucl. Sci. (to be published Dec 1978).

13. J. D. Jackson, Classical Electrodynamics, 2nd Edition, Wiley, New York (1975), p. 51.

14. G. Franceschetti and C. H. Papas, "Pulsed Antennas," IEEE Trans. on Antennas and Propagation, AP-22, 651, (1974).

15. K. G. Balmain et al., "Surface Discharges on Spacecraft Dielectrics in a Scanning Electron Microscope," in Ref. 1, pp 213 ff.

16. N. J. Stevens et al., "Testing of Typical Spacecraft Materials in a Simulated Substorm Environment," NASA TM X-73603, October, 1976.

17. R. C. Adamo and J. E. Nanevicz, "Spacecraft-Charging Studies of Voltage Breakdown Processes on Spacecraft Thermal Control Mirrors," in Ref. 1, pp 225 ff.

18. J. E. Nanevicz and R. C. Adamo, "Malter Discharges as a Possible Mechanism Responsible for Noise Pulses Observed on Synchronous-Orbit Satellites," in Ref. 1, pp. 247 ff.

19. A. Meulenberg, Jr., "Evidence for a New Discharge Mechanism for Dielectrics in a Plasma, in Ref. 1, pp. 237 ff.

20. K. G. Balmain, P. C. Kremer, and M. C. Cuchanski, "Charged Area Effects on Spacecraft Dielectric Arc Discharges,", preprint.

21. S. Bower, "Spacecraft Charging Characteristics and Protection," IEEE Trans. Nucl. Sci., NS-24, 2266 (1977).

22. Rauch and Andrews, IEEE Trans. Nucl. Sci., NS-13, 109, Dec. 1966.

23. N. J. Stevens and R. R. Lovell, NASA TM X-71795, "Spacecraft Charging Investigation for the CTS Project," June 1975.

24. E. J. Yadlowski, "Laboratory Simulation of Irradiation-Induced Dielectric Breakdown in Spacecraft Charging," Semi-Annual Status Report under NASA Research Grant NSG-3145, October 10, 1977.

25. I. K. Hoffmaster and J. M. Snellen, Jr., "Spacecraft Material Response to Geo-synchronous Substorm Conditions," Ref. 1.

26. A. J. Woods and T. N. Delmer, "SKYNET Program, Current Injection Predictions," Part II, 7 Feburary 1975, INTEL-RT-8121-007.

27. J. A. Rosado, "Electrical Injection Simulation of SGEMP," IEEE Trans. Nucl. Sci. NS-22, 2426 (1975).

28. J. Blackburn, "A Radiation Hardened Fiber Optic Transmission System Having a 400 MHz Bandwidth and Linear Response," IEEE Trans. on Instr. Meas. IM-26, 64 (1977).

29. P. P. Budenstein, "Dielectric Breakdown in Solids," U.S. Army Missile Research Development and Engineering Laboratory Technical Report RG-75-25, 20 Dec. 1974.

30. D. C. Hovey, "SABER 3-D SGEMP Code," IRT 0031-071, 31 July 1977.

31. A. J. Woods and T. N. Delmer, "The Arbitrary Body of Resolution Code (ABORC) for SGEMP/IEMP," DNA Report 4342T, 1 July 1976.

32. EGG, EMP Sensor Handbook, Data Sheet 1109, December 1976.

33. R. G. Boyd, IEEE Trans. Nucl. Sci. NS-22, 2431 (1975).

Appendix A
Response Scaling in the CAN Experiment

The object of this analysis is to determine how best to scale (normalize) the body responses from electrical tests so that the results from different test conditions can be compared. In particular, we will apply it to different capacitances in the arc discharge and capacitive drive simulation.

Consider a plate that is hardwire-connected to the test object and that is driven with a given current pulse, $I_P(t)$. We assume that $I_P(t)$ is not a function of the plate spacing, that is, the capacitance (C_P) between the plate and the test body. This analysis is applicable to computer analysis of both the can arc discharge and the simulated outward emission of charge.

The lumped-element model is illustrated in Figure A-1(a) and the resulting equivalent circuit is shown in Figure A-1(b). The charging circuit contains a large resistance R which is omitted from Figure A-1(b) because it will have negligible effect during the discharge.

The quantity of interest is the body skin current, I_s. Therefore, the top of the can and the outside of the discharge plate are coupled to some remote place on the body by body and free-space capacitances (C_B and C_F, respectively). A return leakage path is then allowed along the skin of the test object. Effective inductances are included for free space (L_F) and the body (L_B) to simulate time delay in the traveling wave. However, if the period of the driving pulse $I_P(t)$ is not too short, these inductances do not have a significant effect on the conclusions from this analysis.

The following are the equations for the equivalent circuit.
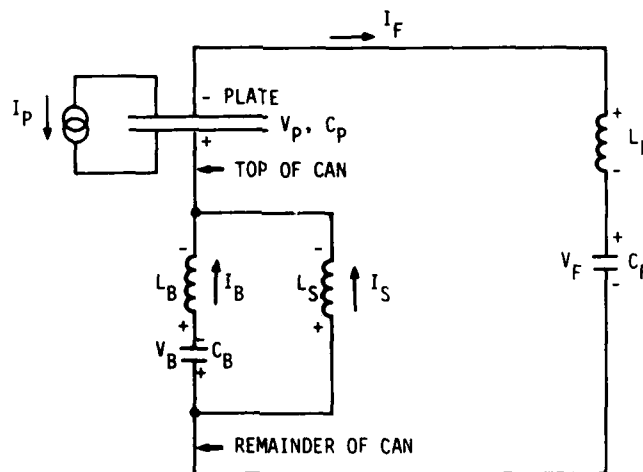
$$C_P \frac{dV_P}{dt} = I_P + I_F \tag{1}$$

$$C_B \frac{dV_B}{dt} = I_B = I_F - I_S \tag{2}$$

$$C_F \frac{dV_F}{dt} = I_F \tag{3}$$
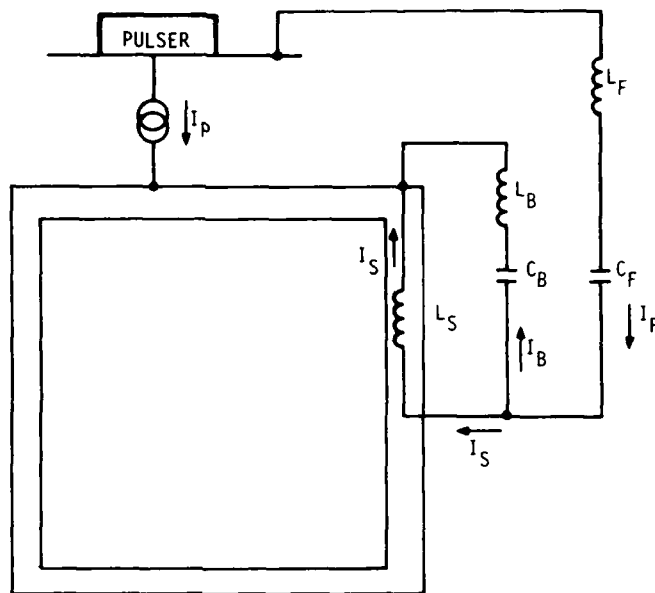
RT-16862

(a) Lumped Element Model

RT-16863

(b) Equivalent Circuit

Figure A-1. Schematic geometry, coupling paths and resultant equivalent circuit for can analysis

124

$$L_F \frac{dI_F}{dt} + V_P + L_B \frac{d}{dt}(I_F - I_S) + V_B + V_F = 0 \tag{4}$$

$$L_S \frac{dI_S}{dt} - V_B - L_B \frac{d}{dt}(I_F - I_S) = 0 \tag{5}$$

The differential equations for the equivalent circuit can be reduced to the form of Equations 6 and 7.

$$\left[(L_B + L_F)\frac{d^2}{dt^2} + \frac{1}{C_P} + \frac{1}{C_F} + \frac{1}{C_B}\right] I_F - \left(L_B \frac{d^2}{dt^2} + \frac{1}{C_B}\right) I_S = -\frac{I_P}{C_P} \tag{6}$$

$$L_B \frac{d^2}{dt^2} + \frac{1}{C_B} \; I_F - (L_S + L_B) \frac{d^2}{dt^2} + \frac{1}{C_B} \; I_S = 0 \tag{7}$$

First consider the case where $C_P \gg C_B$ and/or C_F. In this case C_P^{-1} can be neglected relative to $(C_F^{-1} + C_B^{-1})$ in the first term of Equation 1. With this approximation, the left hand sides of Equations 6 and 7 are independent of C_P so the currents I_F and I_S will be proportional to I_P/C_P, which is approximately equal to $\dot{V}_P$, since I_F will be much less than I_P (see Figure A-1). Therefore, for a very large value of C_P relative to the other capacitances in the system, the skin currents should be scaled proportional to $\dot{V}_P$.

In the other extreme where C_P is small compared to C_B, but not necessarily small relative to C_F, the term $I_F (C_P^{-1} + C_F^{-1})$ will dominate everything on the left-hand side of Equation 6, provided that the period of I_P is not so short that the inductance terms became large. Since a small value of C_P will be due to a large plate separation, C_F will also be small when C_P is small and it will be comparable in magnitude to C_P for all plate separations. Therefore, for the case of $C_P \ll C_B$, I_F is proportional to I_P with a proportionality constant $[C_P^{-1}/(C_P^{-1} + C_F^{-1})]$ that is nearly independent of C_P. Furthermore, since I_S is proportional to I_F by a factor that is independent of C_P (Equation 2), the body skin currents (I_S) should scale with I_P for this situation.

In summary, depending on the relative magnitude of C_P relative to C_B, the body skin currents should scale proportional to $\dot{V}_P$ or I_P.

125

Appendix B

Modeling the Response of the Anvil-2 SCATSAT System

In order to try to obtain a pulse to approximate the desired slow discharge pulse the circuit inductance was varied experimentally. However, the circuit went from critically-damped to oscillatory without significantly increasing the pulse width. Consequently, an analysis of the equivalent circuit of the system was performed to guide the choice of circuit parameters to obtain a longer damped pulse.

The actual test setup is shown in Figure 24 and Figure B-1 shows the corresponding equivalent electrical model as modeled with the TRAC computer program. The charging capacitor, C_C, is charged to the battery voltage V_O (320 volts for this analysis). A pulse is applied to the base of the transistor, driving it into an avalanche mode. While in the avalanche mode, a bulk resistance, R_{BULK}, appears between the collector and emitter of the transistor providing a discharge path. Experience shows that loading the output of the Anvil 160 and 50Ω provides approximately 160 volts across the load for a charge voltage, V_O, of 320 volts. This would imply that R_{BULK} equals about 50Ω.
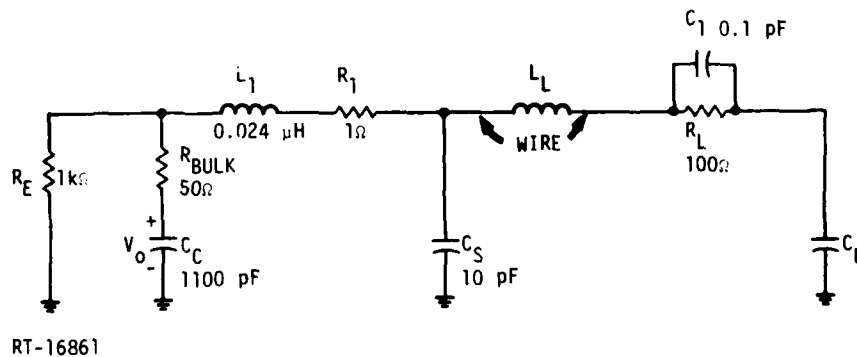

RT-16861

Figure B-1. Equivalent electrical circuit as modeled for TRAC

The value of L_1 is the equivalent inductance of the 4 inches of RG 8 coaxial cable. That value is 0.024 μH for this length of this type of cable. R_L is the resistance of this length of coax and was somewhat arbitrarily chosen to be 1Ω. C_S is the

equivalent capacitance of the coax cable and the stray capacitance from the wire to SCATSAT. The stray capacitance was considered to be small compared to the capacitance of the coax cable which is approximately 30 pF/ft or 10 pF for this 4 inch length.

L_L is the total inductance of the wire, drive plate, SCATSAT, and any lumped inductance that might be added in series with the wire. R_L is the lumped resistance and is a 100Ω resistor. C_1 is the stray capacitance around this resistor, and is estimated at 0.1 pF.

C_L is the capacitance from the drive plate to the surface of SCATSAT. The short pulse testing was done for a spacing of 30 cm between SCATSAT and a 34 cm radius drive plate, and the estimated/calculated capacitance is 10 pF for this configuration.

Figure B-2 shows the computer prediction of the current through R_L with the circuit parameter values as shown in Figure B-1 with L_L = 0.1 μH (an estimated value with no lumped inductance present in the test setup) and C_L = 10 pF. Figure B-3 shows a photograph of the current flowing through the resistor as measured in the lab with the test setup as described above (30 cm plate spacing, no lumped inductance, R_L = 100Ω). It can be seen there is fair agreement between corresponding amplitudes and times. Further minor adjustment of the circuit parameter values could undoubtedly provide even better agreement, but the example shown indicates that the equivalent circuit is basically correct.

Since the purpose of this exercise was to increase the rise time and the decay time, L_L and C_L were varied to see if the desired effect could be achieved. It appeared that increasing only L_L would produce a damped sinusoid pulse and C_L would have to be increased simultaneously to prevent this oscillation. Unfortunately C_L could be increased practically (at most) about a factor of 20 by increasing the drive plate area and decreasing the plate spacing. Figure B-4 shows the predicted current through R_L with all circuit parameters as before except C_L = 200 pF and L_L = 2 μH (both increased a factor of 20 from previous values). Figure B-5 shows the current actually measured using a 62 cm radius drive plate with a plate spacing of 5 to 6 cm. The lumped inductance added is estimated at 2 μH. It can be seen that there is good agreement between the predicted current and measured current.

R_E is the equivalent resistance looking back into the emitter of the transistor. C_C is much greater than the other capacitances, and when the transistor is turned on, only a small portion of the stored energy of C_C is needed to charge C_S and C_L. The current flowing through R_L is essentially the charging current for C_L. When C_C, C_S,
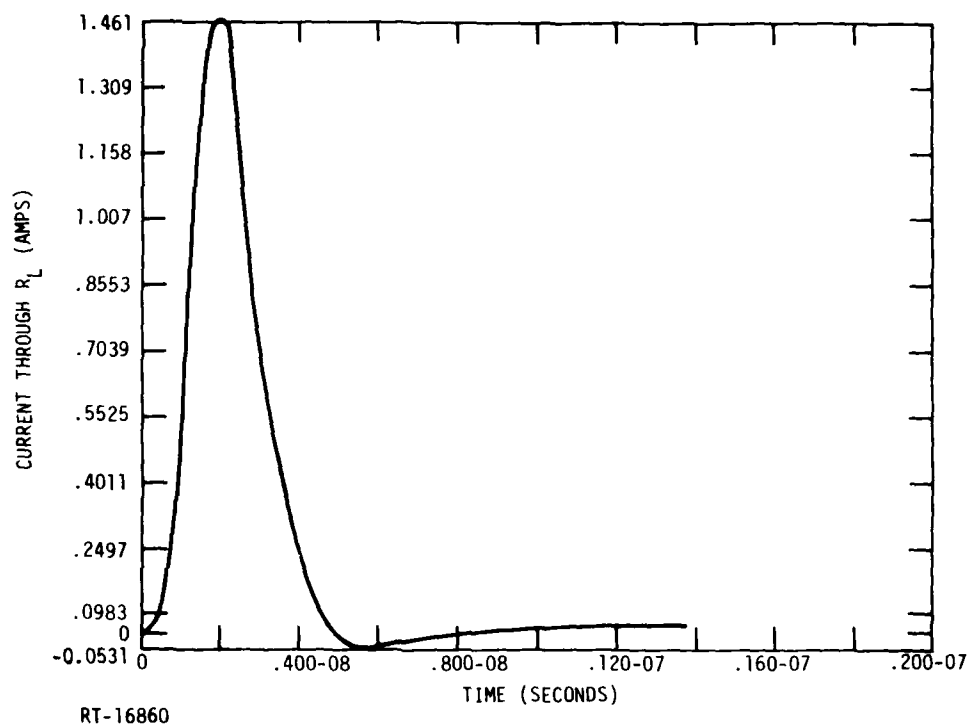
RT-16860

Figure B-2. Computer prediction of current through R_L with C_L = 10 pF
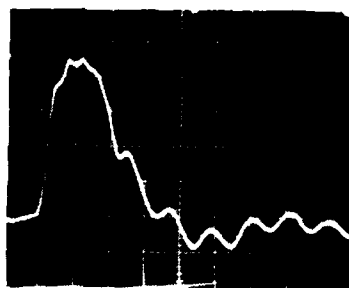and L_1 = 0.1 μH

Figure B-3. Current flowing through R_L with a 34 cm radius drive plate with a
30 cm spacing and no lumped inductance added. The vertical
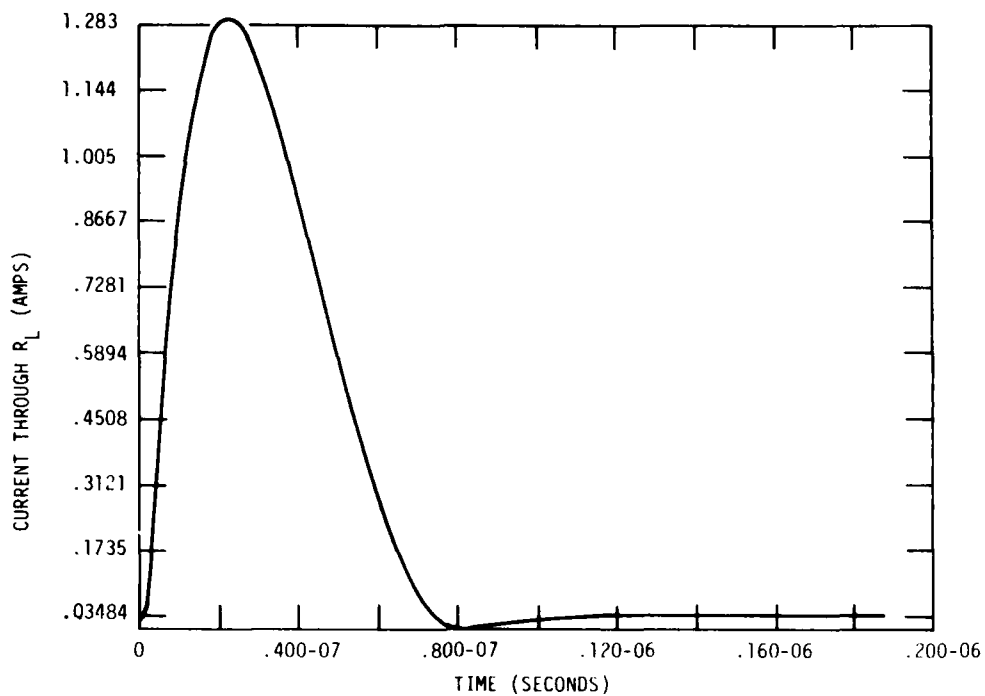scale is 200 mA/division and the horizontal scale is 5 ns/division.

Figure B-4. Computer prediction of current through R_L with C_L = 200 pF and L_1 = 2 μH
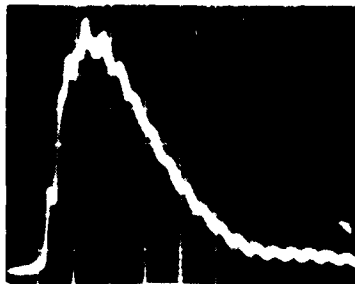
RT-16859

Figure B-5. Current flowing through R_L with a 62 cm radius drive plate with 5-6 cm spacing and an estimated lumped inductance of 2 μH. The horizontal scale is 10 ns/division and the vertical scale is 200 mA/division.

130

and C_L all reach the same potential, the only discharge path to ground is R_E. R_E was arbitrarily chosen to be 1 kΩ so that it was large compared to R_L. After charging, the capacitors will discharge through R_E with a decay constant of R_E times the effective capacitance of C_C in parallel with C_S and C_L. Since most of the stored energy is in C_C, the discharge current from C_S and C_L will be so small as to be negligible. This agrees with the in-lab measurements in which only the charging current through R_L can be observed.

It should be noted that the in-lab measurements (Figures B-3 and B-5) include the current flowing through R_L and the stray capacitance, C_1, whereas the computer predictions do not include the current flowing through C_1. However, upon examining the current flowing through C_1, the computer shows it to be about two orders of magnitude less than the current flowing through R_L at all times, thereby rendering it negligible.

No attempt has been made to vary the circuit parameters to try to exactly reproduce the in-lab measurements. It is expected only minor parameter variations would be needed to achieve this.

In summary, a well-damped pulse with pulse widths of 10 to 30 ns FWHM can be obtained with the present setup but it would be difficult to obtain a significantly longer pulse without oscillations. However, C_L could be increased by making the drive plate conform more clearly to the SCATSAT surface with the possibility of producing longer pulse widths.

Appendix C
## Model Study of Coupling Between Test Area and SCATSAT

The basic problem that was addressed was the determination of the possible effect of reflected electromagnetic energy from the building floor (or wall or ceiling) on the quality of the response of the SCATSAT to the simulation of dielectric discharge. It is clear that even a very large room does not necessarily approximate electromagnetically, a free space environment. Prior to attacking this problem, three basic assumptions were made:

1. The major effect will be on the 19 foot (tip-tip) boom which is driven as a dipole antenna

2. Due to its proximity and orientation, the building floor will be the major reflecting surface

3. Considering the floor to be a perfectly conducting plane is a worst case assumption.

The problem was modeled, therefore, as a dipole antenna of length 2 h (2 h = 19 feet) suspended a height d (d = 5½ feet) above a perfectly conducting plane (and parallel to the perfectly conducting plane). The ground plane images the dipole, so that the system may be considered to be an array of two parallel dipoles separated by a distance 2 d (see Figure C-1).

A simple experiment was conducted to investigate the effects of the height, d, on the antenna response. Figure C-2 illustrates a monopole antenna of length h in the presence of two perfectly conducting ground planes that has the same electromagnetic field behavior as that of Figure C-1. This configuration was constructed in the laboratory and the monopole was excited by a time domain reflectance (TDR). The TDR detected changes in the monopole's driving point impedance due to a varying ground plane spacing, d. This will be seen to be predominantly effected by near field interactions. Simply put, the TDR launches a step voltage on a transmission line that feeds the monopole and then monitors the reflected voltage wave that returns to the TDR. This was done for two different monopole lengths (h) and for a variety of heights,

133

d. The ground plane distance, d ranged from infinity to d = ¼ h. The peak t.) peak response shows that little change is observed as h decreases from infinity until the region of d = ½ h to d = ¼ h. At d = ½ h, the p-p response is only 5% different than when d = ∞. At d = ¼ h, the response is approximately 20% greater than when d = ∞.
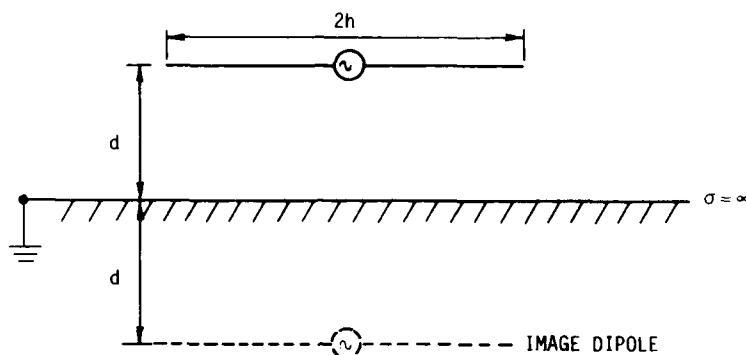
RT-17165

Figure C-J. Horizontal dipole above a ground plane
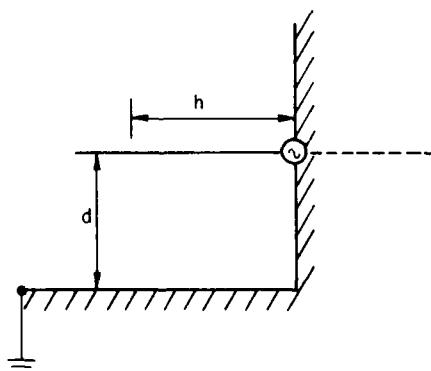
RT-17166

Figure C-2. A monopole in the presence of two ground planes

To recap, this experiment consisted of a short monopole in the presence of two perpendicular groundplanes. The idea was to simulate a dipole antenna (a driven boom) above a parallel groundplane. The monopole was driven by a time domain reflectometer (TDR) and the reflected wave recorded. It was found that the groundplane which

134

represented the building floor had little effect on the peak TDR response until the groundplane was brought within ½ a monopole height (/8) from the monopole. It was inferred from this that since the length of the SCATSAT boom is 19 feet tip-to-tip (implying a monopole length of 9½ feet) that the proposed 5-6 foot elevation of the boom above a floor that is much less reflective than a groundplance is probably adequate to minimize interference effects upon the SCATSAT electrical tests.

Perhaps it should be discussed in slightly more detail, however, how applicable the short monopole results are to a SCATSAT long boom situation. The TDR pulse had a rated risetime of 50 picoseconds. A widely used engineering rule of thumb states that bandwidth in Hertz multiplied by risetime in seconds approximately equals 0.35. Therefore a 50 psec risetime step function implies an upper band edge of 7 GHz. This bandwidth certainly encompasses the short monopole resonant frequenc_es of approximately 455 MHz and 1.1 GHz. An examination of the results shows that the monopoles are ringing near these frequencies.

The monopole antenna is basically a resonant circuit, hence a major consideration in exciting it with a pulse is to determine whether the spectral content of the pulse is sufficient to efficiently excite the antenna's resonant mode. The SCATSAT 19 foot boom should exhibit a resonant frequency near 26 MHz. Both the capacitive direct injection pulse and the arc discharge pulser used by MMC have risetimes of the order of 3 nsec (Ref. C-1). The rule of thumb indicates a band edge near 117 MHz. If either method of excitation had a slower pulse risetime of ~10-15 ns., implying an upper band edge 23-35 MHz, then these pulsers would be borderline in possessing the correct spectral content to excite the boom. As both the short and long pulse had significant frequency components above 50 MHz this is not likely. In fact significant responses were seen at frequencies between 75 and 50 MHz associated with excitation of the boom (q.v. Table 15).

The basic conclusion of the short monopole experiment is unaffected by the method of excitation chosen. If a sufficiently fast risetime method of excitation is used (as it was), then the boom will probably ring well at its resonant mode, the distance to the floor will be about $\lambda/8$, and little interference should be anticipated. If a source with a slow risetime is used, and if the boom is excited, the same conclusion is reached. If the slow risetime method is used and the boom is not excited, then the question of reflections from the floor interferring with boom currents is moot.

135

Analytical Effort

The three dimensional SGEMP code MEEC-3D was used to simulate a rod dipole in a conducting box. The rod was 10 cm square and each rod was 3 m long. The rods had a spacing of 10 cm between them and were driven by a triangular current pulse 10 ns up and 10 ns down. Two runs were made with the rods 1 m and 2 m from the closest wall of the cavity.

For the important quantities, (i.e., H around the rod and E perpendicular to the rod), the maximum differences for the two runs were very minor (less than 15%). Some other quantities, such as E parallel to and close to the rod varied by as much as 50% but their magnitudes were small and not very interesting.

On the basis of these runs, it appears that a separation distance of 1 to 2 meters from the ground for electrical tests of SCATSAT should be adequate to avoid ground interference problems.

Reference

C-1 R.O. Lewis, Jr., "Viking and STP P78-2 Electrostatic Charging Designs and Testing," in Proceedings of the Spacecraft Charging Technology Conference, C.P. Pike and R.R. Lowell eds, AFGL TR-77-0051, 24 February 1977.

DISTRIBUTION LIST

DEPARTMENT OF DEFENSE

Assistant to the Secretary of Defense
Atomic Energy
    ATTN: Executive Assistant

Defense Intelligence Agency
    ATTN: DB-4C

Defense Nuclear Agency
2 cy ATTN: RAEV
4 cy ATTN: TITL

Defense Technical Information Center
12 cy ATTN: DD

Field Command
Defense Nuclear Agency
    ATTN: FCLMC
    ATTN: FCPR

Field Command
Defense Nuclear Agency
Livermore Branch
    ATTN: FCPRL

Interservice Nuclear Weapons School
    ATTN: TTV

Joint Chiefs of Staff
    ATTN: J-5 Nuclear Division
    ATTN: C3S Evaluation Office

Joint Strat Tgt Planning Staff
    ATTN: JLA
    ATTN: JLTW-2

National Communications System
Office of the Manager
Department of Defense
    ATTN: NCS-TS

Undersecretary of Def for Rsch & Engrg
    ATTN: Strategic & Space Systems (OS)
    ATTN: AE

DEPARTMENT OF THE ARMY

BMD Advanced Technology Center
Department of the Army
    ATTN: ATC-O

BMD Systems Command
Department of the Army
    ATTN: BDMSC-H

Deputy Chief of Staff for Rsch Dev & Acq
Department of the Army
    ATTN: DAMA-CSS-N

Electronics Tech & Devices Lab
U.S. Army Electronics R&D Command
    ATTN: DRSEL

U.S. Army Communications Sys Agency
    ATTN: CCM-AD-LB

DEPARTMENT OF THE ARMY (Continued)

Harry Diamond Laboratories
Department of the Army
    ATTN: DELHD-N-RBC, R. Gilbert
    ATTN: DELHD-I-TL

U.S. Army Foreign Science & Tech Ctr
    ATTN: DRXST-IS-1

U.S. Army Missile R&D Command
    ATTN: RSIC

DEPARTMENT OF THE NAVY

Naval Research Laboratory
    ATTN: Code 6707, K. Whitney
    ATTN: Code 7550, J. Davis
    ATTN: Code 6701

Naval Surface Weapons Center
    ATTN: Code F31

Strategic Systems Project Office
Department of the Navy
    ATTN: NSP

DEPARTMENT OF THE AIR FORCE

Air Force Geophysics Laboratory
    ATTN: PH, C. Pike

Air Force Weapons Laboratory
Air Force Systems Command
    ATTN: SUL
    ATTN: NT
    ATTN: NXS
2 cy ATTN: DYC

Ballistic Missile Office
Air Force Systems Command
    ATTN: MNNH
    ATTN: MNRTE
    ATTN: MNNG

Deputy Chief of Staff
Research, Development, & Acq
Department of the Air Force
    ATTN: AFRDQI

Headquarters Space Division
Air Force Systems Command
    ATTN: SKF

Rome Air Development Center
Air Force Systems Command
    ATTN: ESR, E. Burke

Strategic Air Command
Department of the Air Force
    ATTN: NRI-STINFO Library
    ATTN: XPFS

OTHER GOVERNMENT AGENCIES

Central Intelligence Agency
    ATTN: OSWR/STD/MTB, A. Padgett

NASA
Lewis Research Center
    ATTN: N. Stevens
    ATTN: C. Purvis
    ATTN: Library

DEPARTMENT OF ENERGY CONTRACTORS

Lawrence Livermore National Lab
    ATTN: Tech Info Dept Library

Los Alamos National Scientific Lab
    ATTN: MS 364

Sandia National Laboratories
Livermore National Laboratory
    ATTN: T. Dellin

Sandia National Lab
    ATTN: 3141

DEPARTMENT OF DEFENSE CONTRACTORS

Aerospace Corp
    ATTN: Library
    ATTN: V. Josephson

AVCO Research & Systems Group
    ATTN: Library A830

Boeing Co
    ATTN: P. Geren

Computer Sciences Corp
    ATTN: A. Schiff

Dikewood Corporation
    ATTN: Tech Library

Dikewood Corporation
    ATTN: K. Lee

EG&G Washington Analytical Services Ctr, Inc
    ATTN: Library

Ford Aerospace & Communications Corp
    ATTN: A. Lewis
    ATTN: Tech Library

General Electric Co
    ATTN: J. Peden

General Electric Company—TEMPO
    ATTN: W. McNamara
    ATTN: DASIAC

Hughes Aircraft Co
    ATTN: Tech Library

Hughes Aircraft Co
    ATTN: E. Smith
    ATTN: W. Scott
    ATTN: A. Narevsky

DEPARTMENT OF DEFENSE CONTRACTORS (Continued)

IRT Corp
    ATTN: B. Williams
    ATTN: Library
    ATTN: N. Rudie
    ATTN: R. Keyser
    ATTN: R. Leaden
    ATTN: S. Weiman
    ATTN: I. Wilk

JAYCOR
    ATTN: E. Wenaas
    ATTN: Library

JAYCOR
    ATTN: R. Sullivan

Johns Hopkins University
    ATTN: P. Partridge

Kaman Sciences Corp
    ATTN: W. Rich
    ATTN: Library
    ATTN: N. Beauchamp
    ATTN: D. Osborn

Lockheed Missiles & Space Co, Inc
    ATTN: Dept 85-85

McDonnell Douglas Corp
    ATTN: S. Schneider

Mission Research Corp
    ATTN: C. Longmire
    ATTN: R. Stettnner

Mission Research Corp
    ATTN: B. Goplen

Mission Research Corp-San Diego
    ATTN: V. Van Lint
    ATTN: Library

Pacific-Sierra Research Corp
    ATTN: L. Schlessinger
    ATTN: H. Brode

R & D Associates
    ATTN: S. Siegel
    ATTN: R. Schaefer
    ATTN: Tech Info Center
    ATTN: P. Haas

Rockwell International Corp
    ATTN: Library

Science Applications, Inc
    ATTN: W. Chadsey

Spire Corp
    ATTN: R. Little

SRI International
    ATTN: Library

Institute for Defense Analyses
    ATTN: Classified Library

138

DEPARTMENT OF DEFENSE CONTRACTORS (Continued)

Systems, Science & Software, Inc
    ATTN: A. Wilson
    ATTN: Library

DEPARTMENT OF DEFENSE CONTRACTORS

TRW Defense & Space Sys Group
    ATTN: D. Clement
    ATTN: Technical Information Center